LEVEL 12

RADC-TR-81-198
Final Technical Report
July 1981

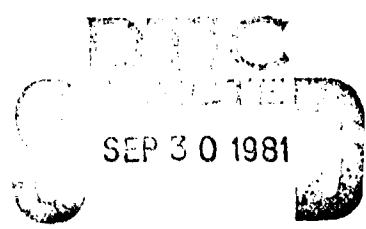# CONDUCTION AND CHARGE STORAGE IN ELECTRON IRRADIATED SPACECRAFT INSULATORS

IRT Corporation

J. Wilkenfeld
C. Mallon
J. Horne

SEP 3 0 1981

A

ROME AIR DEVELOPMENT CENTER
Air Force Systems Command
Griffiss Air Force Base, New York 13441

81 9 30 039

This report has been reviewed by the RADC Public Affairs Office (PA) and is releasable to the National Technical Information Service (NTIS). At NTIS it will be releasable to the general public, including foreign nations.

RADC-TR-81-198 has been reviewed and is approved for publication.

APPROVED: *James A. Wall*
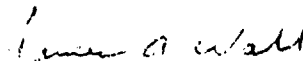
      JAMES A. WALL
      Project Engineer

APPROVED: *Freeman D. Shepherd Jr.*

FREEMAN D. SHEPHERD JR.
Acting Director, Solid State Sciences Division

FOR THE COMMANDER: *John P. Huss*

      JOHN P. HUSS
      Acting Chief, Plans Office

REPORT DOCUMENTATION PAGE		READ INSTRUCTIONS BEFORE COMPLETING FORM
1. REPORT NUMBER RADC-TR-81-198	2. GOVT ACCESSION NO. AD-A104 796	3. RECIPIENT'S CATALOG NUMBER
4. TITLE (and Subtitle) CONDUCTION AND CHARGE STORAGE IN ELECTRON IRRADIATED SPACECRAFT INSULATORS		5. TYPE OF REPORT & PERIOD COVERED Final Technical Report Sep 1977 – Sep 1980
		6. PERFORMING ORG. REPORT NUMBER IRT-8172-008
7. AUTHOR(s) J. Wilkenfeld C. Mallon J. Horne		8. CONTRACT OR GRANT NUMBER(s) F19628-77-C-0245
9. PERFORMING ORGANIZATION NAME AND ADDRESS IRT Corporation PO Box 80817 San Diego CA 92138		10. PROGRAM ELEMENT, PROJECT, TASK AREA & WORK UNIT NUMBERS 62702F 46002020
11. CONTROLLING OFFICE NAME AND ADDRESS Deputy for Electronic Technology (RADC/ESR) Hanscom AFB MA 01731		12. REPORT DATE July 1981
		13. NUMBER OF PAGES
14. MONITORING AGENCY NAME & ADDRESS(if different from Controlling Office) Same		15. SECURITY CLASS. (of this report) UNCLASSIFIED
		15a. DECLASSIFICATION/DOWNGRADING SCHEDULE N/A

16. DISTRIBUTION STATEMENT (of this Report)

Approved for public release; distribution unlimited

17. DISTRIBUTION STATEMENT (of the abstract entered in Block 20, if different from Report)

Same

18. SUPPLEMENTARY NOTES

RADC Project Engineer: James A. Wall (ESR)

19. KEY WORDS (Continue on reverse side if necessary and identify by block number)

Spacecraft charging	Conductivity
SCATHA	Polymers
Electrons	Fused Quartz
Charge transport	

20. ABSTRACT (Continue on reverse side if necessary and identify by block number)

Charge, storage and conduction processes were studies in four spacecraft insulators, FEP Teflon, Kapton, Mylar and fused quartz exposed to mono-energetic electron beams with energies of 5-27 keV as a function of particle flux, sample thickness, applied external bias and temperature. The experimental data was used to determine some of the parameters which control the deposition and transport of keV electrons in representative spacecraft insulators found on the surface of communication and other satellites

DD FORM 1473 EDITION OF 1 NOV 65 IS OBSOLETE

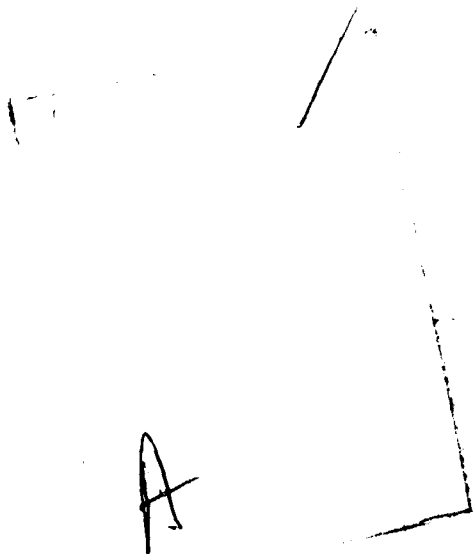placed in geostationary orbits. Properties determined include location of the charge deposition centroid, dark, radiation, delayed and surface conductivities. These parameters were then used in a phenomenological transport model to interpret the observed charge leakage behavior under various exposure conditions.

In the model, the sample is divided into two regions. In the irradiated region, radiation-induced conductivity is the predominant conduction mechanism. In the nonirradiated region, space-charge limited currents predominate.

TABLE OF CONTENTS

LIST OF FIGURES

LIST OF TABLES

1. EXECUTIVE SUMMARY

The primary objective of this study has been to determine some of the parameters which control the deposition and transport of keV electrons in representative spacecraft insulators found on the surface of communication and other satellites placed in geostationary orbits. Properties determined include location of the charge deposition centroid, dark, radiation, delayed and surface conductivities as a function of incident electron energy and flux, sample temperature and magnitude of externally applied bias. These parameters were then used in a phenomenological transport model to interpret the observed charge leakage behavior under various exposure conditions.

The study was motivated by a desire to understand the behavior of spacecraft insulators exposed to high energy particle radaition. Geosynchronous spacecraft are exposed to the hot plasmas associated with magnetic substorms. In such storms, electrons with initial energies of many keV can become trapped in surface dielectrics found in satellites because of the high resistivities of these materials. Relatively high potential differences can be built up between different portions of the spacecraft which may result in dielectric breakdown. Such breakdown can induce electromagnetic interference signals in electronics which may have adverse consequences on performance. Breakdown may also lead to damage or contamination of surface coatings. Because of the harmful consequences of spacecraft charging, the National Aeronautics and Space Administration (NASA) and the United States Air Force (USAF) are performing a joint technology program entitled SCATHA (Spacecraft Charging at High Altitude) (SCATHA) of which this effort is a part.

This program was a combined experimental and analysis effort in which charging experiments were performed on four common spacecraft insulators, FEP Teflon, Mylar, Kapton and fused silica. The measurements consisted in exposing samples of these materials (typically ca. 25 μm thick) to a uniform monoenergetic electron beam of energy between 5 and 27 keV and of current density ca. 0.5 to 5 na/cm^2 representative of electron energies and fluxes associated with magnetic substorms. For most combinations of beam energies and sample thicknesses, the electron beam is stopped in

the sample (nonpenetrating). During, and sometimes after, irradiation, the current exiting or charge accumulating on the front and rear surfaces of the sample was monitored as a function of time, often for different values of an applied external bias which ranged from -500 V to $+500$ V.

Material parameters were extracted from the data using a model in which the sample is divided into an irradiated region which extends from the electrode of incidence to the practical range of the beam and a nonirradiated region. In the irradiated region ionization creates an electron-hole plasma and conduction occurs primarily through the induced radiation conductivity. The end plane of the deposited space charge acts as a virtual electrode for injection of charge carriers into the nonirradiated region of the sample where conduction is by excess charge. While a somewhat simplified model, it explicitly relates the charge transport behavior (i.e., currents) to material properties in analytical expressions.

The values determined for the mean depth of the deposited charge centroid are comparable to or somewhat larger than those predicted by transport calculations. It is believed that this is due to a motion of injected charge deeper into the insulator under the combined influence of radiation-induced conductivity and internal space charge fields which are significant out to the CSDA electron range. Such charge transport is not taken into account in this simple model.

Radiation conductivity, g_D, data were determined by two methods. In one, which is the classical approach, the sample is exposed to a penetrating beam of radiation. The second is based on measuring the decay of stored space charge when the sample is exposed first with the front electrode open and then shorted. All of the data could be fit to an expression of the form $g_D = K_D \dot{D}^\Delta$, where $\dot{D}$ is the dose rate and K_D and $0.5 \leqslant \Delta \leqslant 1$ are material constants. For the dose rates relevant to these experiments (3 to 50 krads/s) radiation conductivities ranged from 5×10^{-15} $(\Omega\,cm)^{-1}$ to 10^{-12} $(\Omega\,cm)^{-1}$, depending on material and dose rate. Such values are orders of magnitude larger than dark conductivities $(<10^{-17}$ $(\Omega\,cm)^{-1})$ as assumed in our charge transport model.

The delayed conductivity after irradiation $\bar{g}(t)$ was found to be proportional to $t^{-\gamma}$ where, for a given material, γ has the same value as the exponent Δ for the dose rate dependence of radiation conductivity. As $0.5 < \gamma < 1$, this is a somewhat slower rate of decay than the t^{-1} rate predicted for bimolecular recombination. That $\Delta < 1$ is in agreement with the model in which trapping plays a significant role in the kinetics of charge transport in these materials.

2

The front and rear electrode leakage measurements displayed the following patterns. Where the ratio of the charge centroid $\overline{R}$ to sample thickness T_s was $< 1/2$, I_1', the current leaving the front electrode (after correction for backscattering and secondary electron effects) was approximately equal to I_t, the injection current. The current leaving the rear electrode was several orders of magnitude smaller, but still much larger than expected if due to the normal dark conductivity. When $\overline{R}/T_s$ approaches but is still less than 1, the magnitude of I_2, the rear electrode current, approaches I_t. We interpret this behavior to be evidence of the role that space-charge-limited conduction plays in charge transport in the unirradiated region.

The phenomenological model was employed to reproduce features of the leakage current measurements such as the value of applied bias V_o at which $I_2 = 0$ and to compute values for the trap modulated mobilities in the nonirradiated regions of the sample. Generally, the predicted and measured values of V_o were within a factor of 2 or 3 of each other. Possible sources of error include difficulty in determining V_o experimentally, errors in the method used to calculate the dose rate in the polymer on which V_o depends through the value of the radiation-induced conductivity, and the simplified nature of the model.

Mobility values were determined for charge transport in the nonirradiated region of the sample at $300^\circ K$ for Mylar, Kapton and Teflon. The values were μ_- (Mylar) = 1.3-2.4×10^{-13} cm^2/Vs, μ_- (Kapton) = 2.8×10^{-13} cm^2/Vs and μ_- (Teflon) = 4×10^{-12} cm^2/Vs. Because of experiment conditions, these are electron mobilities.

In summary, the simple model predicts in a general way the trends in the experimental leakage data, but a more detailed analysis which fits the data to a specific trap structure is required. Additional experiments to determine the detailed charge distribution, would be useful. Also, necessary are thermally stimulated current measurements on electron charged polymers of interest to determine more detailed information about trap distributions. Another useful activity to pursue would be the development of transport-type models in which realistic models of conductivity, including space-charge transport, are included.

Experiments to measure the effective surface conductivity of these materials did not work out as planned because charging dynamics were controlled not by applied external bias but by the tangential component of the space charge fields deposited in the unelectroded regions of the insulator between electrodes. Our experiments show that whether breakdown occurs for given charging conditions depends on edge effects;

3

i.e., the spacing of grounded conducting electrodes. Surface conductivity can be defined more precisely under irradiation since is essentially defined by the product of the conductivity of the irradiated region of the polymer and its depth. Additional experiments to examine edge effects in a systematic manner should be undertaken as many engineering fixes for spacecraft charging involve various forms of edge grounding.

2. BACKGROUND AND APPROACH

2.1 PROBLEM OF SPACECRAFT CHARGING

Over the last several years, a series of anomalies have been observed in the behavior of satellites located in geosynchronous orbits at altitudes of several earth radii (Ref 1). The anomalies have included equipment malfunctions such as uncommanded changes in operation, the recording by detectors of spurious events which in fact had not occurred, and a persistent rise in operating temperatures. In at least one case it is thought that discharge-induced failure led to the loss of a satellite. It was gradually realized that the appearance of many, but not all, of these anomalies could be correlated with the presence of a satellite in a magnetic substorm. These findings have been summarized in the Proceedings of the AIAA/AGU Symposium on Spacecraft Charging by Magnetospheric Plasmas (Ref 2) and in those for two Spacecraft Charging Technology Conferences (Refs 3,4).

In such storms, the relatively cold, high-density plasma (with electron temperatures of a few eV or less) is replaced by a much hotter lower-density plasma with a temperature on the order of 10 keV or more (Ref 5). The electron component of such a plasma is energetic enough to penetrate the surface of irradiated dielectrics where they are trapped. Because of the high resistivity of such dielectrics some of the embedded charge will not leak off. In this manner, the irradiated and shadowed portions of a spacecraft can be differentially charged. This effect can be enhanced if one side of the spacecraft is not illuminated by sunlight. The illuminated portion of the spacecraft will tend to remain near the potential of the ambient plasma because of UV-induced photoemission. Such differential charging of electrically isolated dielectrics can lead to the creation of potential differences between spacecraft components which can be as large as 10 to 20 kV.

At a sufficiently high potential gradient, dielectric breakdown will occur. Three types are distinguishable. In one, the discharge current travels from one metal surface to another through the volume of the dielectric. This has been called metal-to-metal discharge. A second type of discharge runs along a dielectric surface to a conductor

5

and has been designated dielectric-to-metal arcing (Ref 5). In conventional insulator literature the former is typically called punchthrough, while the latter is termed flashover. A third type of dielectric breakdown may occur in electron irradiated spacecraft insulators in which the consequent discharge results in the expulsion of particles (electrons, ions) and debris out through the front surface (Ref 6). Such discharges generate electromagnetic interference that can couple into circuits; the resultant transients may then produce circuit malfunction or upset if they are not properly circumvented. The discharge current also generates replacement currents. Laboratory experiments and analysis (Ref 7) have demonstrated that of the three types, blowoff discharges will produce the largest replacement currents per amp of drive current and hence typically will evoke the most severe response. The discharges not only affect circuits, but also may degrade thermal blankets and second-surface mirrors, which may cause a rise in satellite temperature. The discharge products can contaminate other critical surfaces such as those found in optical devices. In order to effect a level of hardening that is adequate but not excessive, one must be able to predict the behavior of spacecraft in worst-case environments. Thus, one must develop realistic models on which to base such predictions.

As the problem of spacecraft charging is potentially catastrophic (i.e., it may lead to spacecraft failure), a joint NASA-U.S. Air Force program was developed (Ref 8). The goals of this program, denoted SCATHA (Spacecraft Charging at High Altitudes) are to understand the problems which arise from the differential charging of spacecraft surfaces and to develop the technology to render spacecraft immune to them. A portion of this program is aimed at determining those mechanisms which lead to charge accumulation and subsequent breakdown in spacecraft structures containing insulators. Such a study has three aspects. The first is a proper specification of the radiation environment, i.e., the electron, proton, ion, and photon fluxes and energies. These will vary as a function of location and local time, and, in particular, will depend upon whether a geomagnetic substorm is present. Second, the flow of charge and the possibility of breakdown will depend on the geometric arrangement of structures on the satellite; i.e., which portions are exposed or shadowed and the detailed configuration of the capacitive structures through or across which discharge may occur and their electrical connectivity. Finally, the relevant material parameters that control the motion of charge through and across these insulators must be determined, where unknown; and it must be understood, in particular, how they may be modified by the

radiation environment present in a geosynchronous satellite orbit. The parameters are summarized in Table 1. The list is not meant to be definitive.

Table 1. Material Properties Relevant to Spacecraft Charging

Bulk Property	Environmental Dependence
Volume conductivity	Temperature, electric field, radiation fluxes
Surface conductivity	Temperature, electric field, particle and photon radiation fluxes, depends on surface conditions
Dielectric breakdown strength	Temperature, sample thickness, modified by radiation, sample geometry
Radiation conductivity	Dose rate, dose
Photoemission	Photon energy, flux
Charge deposition	Incident particle type, energy spectrum, flux, dose, temperature
Secondary emission coefficient	Incident particle type, energy, angle of incidence, surface condition, dose
Backscatter coefficient	Incident particle type, energy, angle of incidence, surface condition, dose

2.2 RADIATION ENVIRONMENT

In order to define reasonable simulation conditions for our test program, a brief description of the radiation environment seen by a satellite in a geosynchronous orbit is given. The space environment of concern for these tests shown in Table 2 consists of the relatively tenuous plasma whose density is ca. 0.5-10 electron-ion pairs per cm^3 at geosynchronous altitudes (Refs 9,10), solar electromagnetic radiation (Ref 11), and trapped electrons associated with the outer Van Allen belt (Refs 12,13).

The power incident on a spacecraft from solar radiation is 1.4 kW/m^2. The spectrum is one which, at long wavelengths, is like that of a 6000°K blackbody, which peaks at about 0.4 μm and which rapidly diminishes below 0.2 μm. However, because the quantum efficiently rapidly increases at lower wavelengths, most photoemission is produced by vacuum UV or harder photons. Thus, the commonly employed solar simulator, which outputs little, if any, UV below 2000 Å, is a poor simulation (Ref 14). The effect of this radiation is to cause the photoemission of electrons. Photocurrents of $\sim 5 \cdot 10^{-9}$ A/cm^2 are typical (Ref 5). Such photoemission tends to keep the potential of the satellite near that of the surrounding plasma.

7

Table 2. Components of Space Radiation Environment

Component	Characteristics	Effects Produced	Comments	References
1. Net particle density	ca. 0.5-10 cm^{-3} at geosynchronous altitudes			(9)
2. Solar electromagnetic	0.14 w/cm^2 total flux. Visible, IR like 6000°K blackbody. UV comprised of discrete lines, of which H(Lyα) is most important, superimposed on a continuum.	photoemission (UV,x-ray), heating (visible, IR) Photoconductivity (UV, visible)	Photoemission controlled by surface properties	(11)
3. Natural trapped electron	Outer zone specified in AEI-7. Energies ca. 0.1-5 MeV. Integral omnidirectional flux ca. $10^8 e/cm^2$ sec at geosynchronous altitudes	Charge and dose deposition, secondary emission, backscatter, semiconductor damage, leakage currents, discharges	Primary effects in spacecraft dielectrics include enhancement of bulk charge leakage, charging of internal dielectrics	(12,13)
4. Magnetic substorm	Correlation with A_p index. Characterized by single or double Maxwellian $J_e < 1$ na/cm^2, $k_B T_e < 15$ keV $J_i < 100$ pa/cm^2, $k_B T_e < 20$ keV where T_e is T_{rms}, based on ATS-6 data.	Charge, dose deposition secondary emission, backscatter, leakage currents, discharges	Typical electron environments $J_e = 0.02$-0.12 na/cm^2 $k_B T_e = 1$ keV 0.01-0.2 $= 5$ keV 0.01-0.07 $= 8$ keV Typical ion environments $J_i = 2$-7 pa/cm^2 $k_B T = 3$ keV $J_i = 2$-8 pa/cm^2 $k_B T = 7$ keV Based on ATS-5 data. The observed ATS-6 environments are more severe.	(9,10)
5. Nuclear trapped electron	Fission electron spectrum. Integral fluxes ca. 10^9 $e/cm^2 \cdot$ sec (minutes), ca. 7×10^7 $e/cm^2 \cdot$ sec (long term)	Charge and dose deposition, secondary emission, backscatter, semiconductor damage, leakage currents, discharges	Same as item 3, but charging rates are faster because of higher fluxes	(13)

Also present is the normal hydrogen ion plasma. The energy distribution of this plasma is typically described by one or two Maxwellian distributions, with an electron and ion temperature that correspond to particle energies well below 1 keV. Under normal environments, the combination of electron charging and electron photoemission ensures that the potential of a satellite relative to the plasma is never large. This is true even for satellites that are eclipsed. This is related to the fact that the maximum potential difference between an object immersed in a plasma of energy $k_B T_e$, where k_B is Boltzman's constant $= 8.63 \times 10^{-5}$ eV/°K, and T_e the plasma temperature in °K, and the plasma is $3.6 \ k_B T_e$ (Ref 8). Most significant for the creation of differential charging is the electron flux associated with a substorm plasma. As the electron temperature of the plasma corresponds to energies of ~10 keV, large voltages between components can be built up that can lead to breakdown. The charging effect of the substorm plasma is diminished if the satellite is exposed to sunlight because of photoemission. Worst-case charging scenarios are most common in the midnight-to-dawn segment of local time as magnetic substorms typically occur then (Ref 1). The

spacecraft is also exposed to the normal trapped radiation environment, which contains high energy electrons with energies ranging from below 50 keV to several MeV. The data given in Table 2 for this component are based on a representative environment for a synchronous orbit from the AEI-7 model. Its contribution to the net electron flux impinging on a satellite is several orders of magnitude smaller than that due to the plasma electrons. As these electrons have significantly greater ranges in materials than those for the ambient plasma, even in substorm conditions, they may cause special problems resulting from the charging of components such as cables which are normally shielded from the plasma radiation flux. In the environment consequent to a nuclear burst, a spacecraft will be subject to an additional component of penetrating high energy trapped fission electrons. Because of their range, these electrons may not only cause electrostatic discharging in the spacecraft interior but possibly also cause direct damage to electric circuitry (Ref 15).

2.3 OBJECTIVES AND APPROACH

The primary objectives of this program have been to determine some of the parameters which control the deposition of and transport of charge in representative insulators under a limited subset of the total radiation environment shown in Table 2 to which a spacecraft in geosynchronous orbit may be exposed. Properties determined included charge deposition depth, dark, photo, delayed and surface conductivity. These parameters were then used in quantitative phenomenological models to predict features of the experimentally determined leakage currents observed in the dielectrics when exposed to radiation and external bias.

The deposition and motion of electrons in insulating materials is most significant in determining whether a sufficient potential difference will build up which results in breakdown. Much work to date, as embodied in the NASCAP code (Ref 16) assumes that the electrons are deposited on the surface of the dielectric. Such an assumption is perhaps valid in determining surface potential buildup in dielectrics where the maximum electron range is much less than dielectric thickness. However, even electrons of a few keV have ranges of a few μm in typical polymer dielectrics which is many thousands of atomic layers thick. As we shall describe in a later section of this report, even surface charge leakage under irradiation is controlled by the behavior of a thin layer of the bulk material whose conductivity is enhanced by radiation induced generation of charge carriers. Moreover, where the polymer films are thin; i.e., where

there are significant numbers of high-energy electrons, (those whose range is comparable to or greater than the material thickness) bulk leakage behavior becomes important. Finally, evidence based on observations such as the creation of Lichtenberg figures in thicker dielectrics and discharge tracks in films (Ref 17) indicates that the detailed charge and dose deposition profiles are significant in determining the nature of the breakdown induced.

Clearly, to carry out the full set of measurements to determine all material parameters under the full spectrum of environments described in Table 1 would have necessitated a program many times the size of that undertaken. We have therefore concentrated on those elements most important for an understanding of internal charge motion in these dielectrics, namely electron energy and flux, and sample temperature and applied bias.

Therefore, we chose to determine the material parameters above using mono-energetic electron beams with energies of 5 to 27 keV and beam currents whose order of magnitude flux ranged from a fraction of to several times 1 na/cm^2, and at temperatures which ranged from 100°K to as high as 600°K. While the temperature range is much greater than that found in properly functioning spacecraft, one can learn much about the nature of material parameters such as mobility by determining their temperature dependence.

No account has been taken of the effect of ions or UV in determining surface potential or charge transport. Because of their greater mass, the proton currents associated with the plasma are more than an order of magnitude lower than those of electrons. Their range in dielectrics is similarly reduced. The net effect of ions (and of UV photons), is to reduce the surface potential because of secondary electron production. While these effects are significant in reducing the surface potential of spacecraft dielectrics in the real environment, they are not essential to an examination of electron trapping and transport in materials. However, to predict the behavior of real spacecraft, values for the secondary electron coefficients produced by ions and electrons and for photoemission must be determined for relevant spacecraft materials.

The basis of our approach was to utilize the body of experimental techniques and theoretical models developed to study conductivity and radiation effects in insulators. This work has provided measurements for some of these same material parameters, such as photoconductivity, as well as relevant physical models. The state of these data as of 1976 was summarized in the paper of Wall, Frederickson and Burke (Ref 18) which

10

presents an overview of the nature of the fundamental material parameters needed to model electrostatic charging and discharge and contains a useful bibliography.

The fact that many insulators can stably store charge for periods of the order of years is of technological significance. Polymer films in which charge has been introduced are known as electrets and form the active element in transducers such as microphones. Because of a growing commercial interest in such materials, their behavior under irradiation has been extensively studied (Refs 19-21). The processes used to create electrets are similar to those by which spacecraft dielectrics are charged. One can directly apply the extensive theory developed to model electrets to understand the response of spacecraft insulators exposed to space radiation. In fact, we have employed, for the most part, both the techniques and models developed by Gross, Sessler, West and others as the foundation for our own efforts as will be described in the following sections. The main element in the measurement approach is the use of the split Faraday cup developed by Spear (Ref 22) in which either the currents or voltages at both surfaces of the sample are monitored during and after irradiation.

2.4 CONTENTS

The remainder of this report is organized as follows. The third section presents a discussion of the experimental techniques employed to measure the voltage and current characteristics of the irradiated dielectric samples, as well as a description of the sample chamber, electron guns and beam diagnostics and sample mounting configuration.

The fourth section describes the model used to determine material parameters from the experimental measurements and presents our determination of these properties including charge deposition, prompt radiation and delayed conductivity. It is to be stressed that while we have chosen to interpret the observed behavior of these samples with a relatively simple model, such an evaluation represents only a first cut at developing a more sophisticated model which predicts not only the equilibrium charging behavior but also transient effects.

The fifth section presents an evaluation of our measurements of leakage currents in the irradiated polymer samples under temperature and bias and an application of the model presented in Section 4 and the determined material parameters to reproduce some of the significant features of the data.

The sixth section of the report describes the surface leakage experiments. The point of view used to evaluate these data is that in this case surface leakage or surface conductivity is a reasonably well defined quantity, which is determined by the radiation-induced bulk conductivity in the irradiated upper layer of the material.

12

3. EXPERIMENTAL APPARATUS

This section describes the sample irradiation chamber, the electron gun, incident and emitted particle diagnostics, sample mounting, sample configuration and measurement techniques.

3.1 VACUUM EXPOSURE CHAMBER

The vacuum exposure chamber dimensions are shown in Figure 1. Figure 2 is a photograph of the outside of the chamber. With the present arrangement, the sample-to-electron gun-UV source distance is 91.4 cm (36 inches). Samples up to 25.4 cm (10 inches) in diameter can be irradiated. The system has two liquid nitrogen trapped oil diffusion pumps 15.2 cm and 10.2 cm (6 and 4 inches). For most runs, only the six-inch diffusion pump was used. Both the source chamber and the target chamber have liquid nitrogen traps for cryosorbtion pumping. The tank had a base pressure of 3×10^{-7} torr reached in a relatively short pumping time. The exposure chamber has six high-quality, low-leakage General Radio Type 874 feedthroughs for signal leads and numerous other feedthroughs for diagnostics. Figure 3 is a photograph of the interior of the exposure chamber and shows the location of the major experimental items.
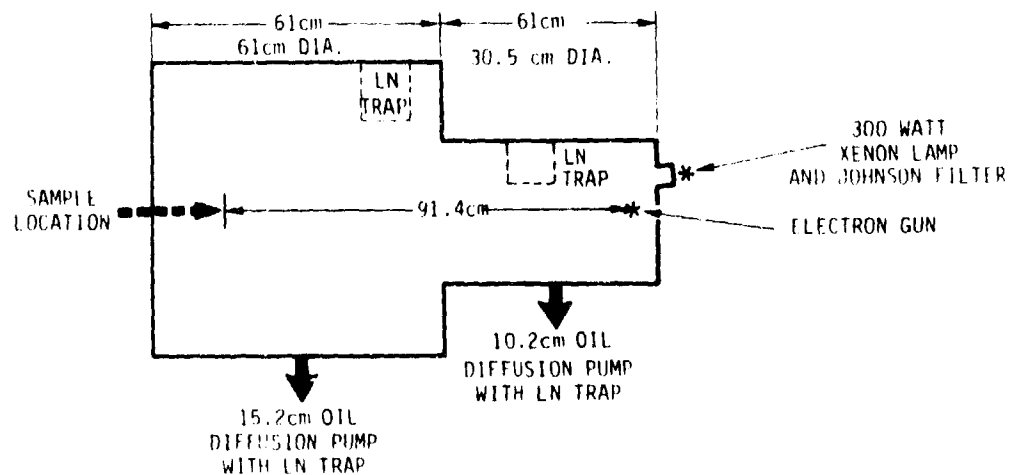
Figure 1. Vacuum exposure chamber
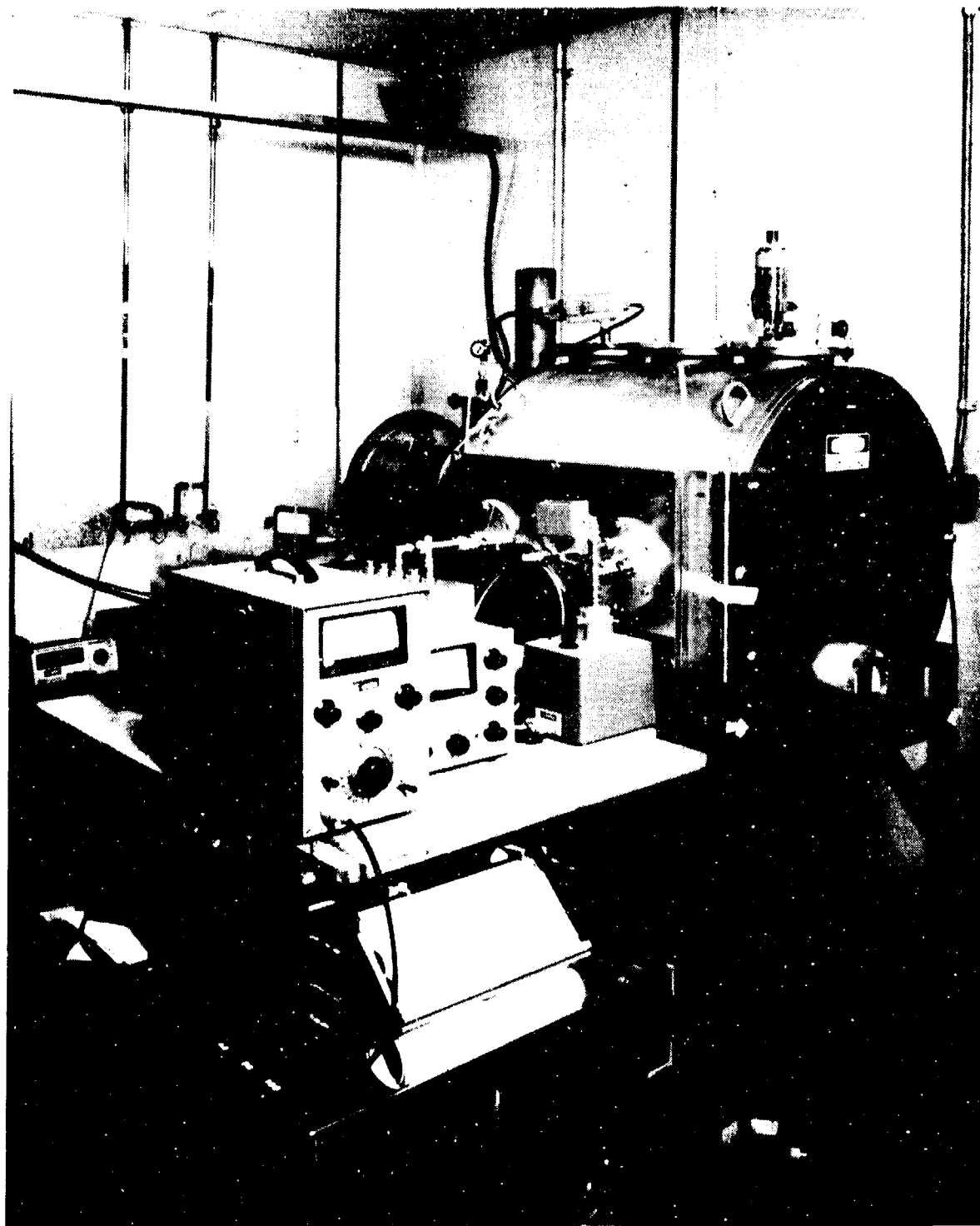
Figure 2. Experimental chamber
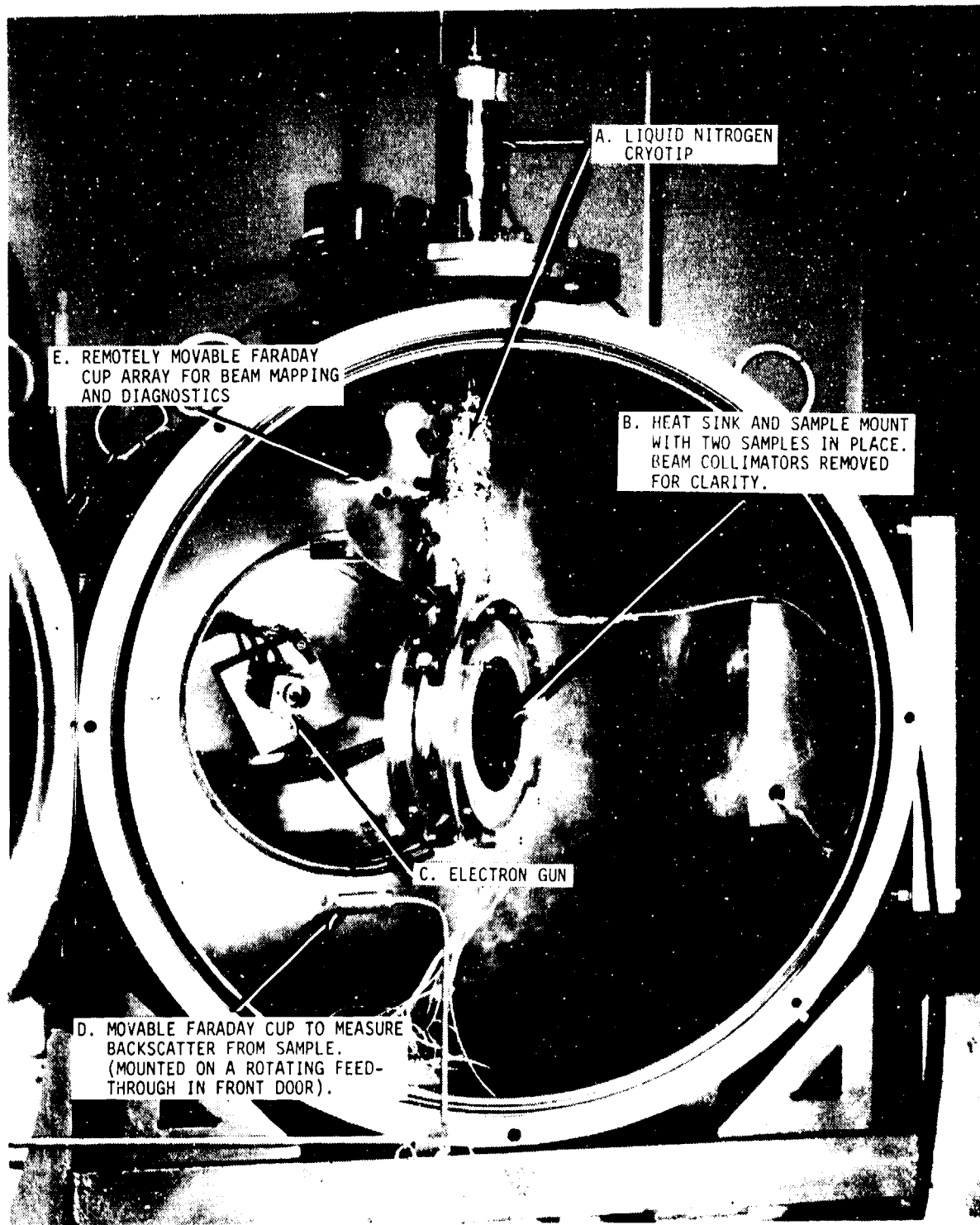
Figure 3. Interior of exposure chamber

3.2 ELECTRON GUN

The IRT designed and constructed electron gun was installed in the vacuum exposure tank. It was designed to provide a uniform beam one meter in diameter at a distance of two meters (Ref 23). (A gun of similar design was used in the SKYNET satellite electron spraying experiments in the four-meter tank at Physics International.) At the gun-to-sample distance of 91.4 cm (36 inches) in the vacuum exposure tank, beam mapping has shown that the current density is uniform (better than ±20 percent) over a 50.8 cm (20 inch) diameter which is much greater than the present sample size. The calibration of the electron guns employed is shown in Figure 4. The electron current density was typically uniform to better than ±5 percent over a sample diameter (7.5 cm). A photograph of two of these guns is shown in Figure 5.

The gun filament is constructed of four turns of 10 mil thoriated tungsten. The filament is heated by a well-regulated, low-voltage, high-current power supply, and provides fine control of the electron emission from the filament as shown in Figure 6. The filament current is regulated to provide a stable electron beam as a function of time. Typically a ±1 percent current stability over eight hours could be achieved. The present gun design limits the high-voltage accelerating potential to ~30 kV. The high voltage was provided by regulated supplies and was measured with a Kiethly 6103A 1000:1 voltage divider probe. Electron energies were accurate to within 2 percent of the chosen value. The block diagram of the electron gun and associated supplies is shown in Figure 6. A remotely controlled stopping shield was located in front of the extractor. It has a 2 msec gating time.

3.3 ELECTRON BEAM DIAGNOSTICS

Five Faraday cups (Figure 3, Item E) were used to monitor beam intensity and uniformity. The Faraday cups are mounted on a movable plate that shields the sample during beam diagnostics prior to an irradiation. After the desired beam parameters are established, the Faraday cup array is removed for sample irradiation.

An additional Faraday cup (Figure 3, Item D) is mounted on a wand which passes through a vacuum-tight rotating feedthrough mounted on the front door which enables it to be remotely passed over the sample surface. Its orientation can be fixed such that it looks toward the electron gun for additional beam mapping or towards the sample surface to monitor backscatter. The calibration and use of this Faraday cup to measure the back-emitted current is discussed in subsection 4.2.
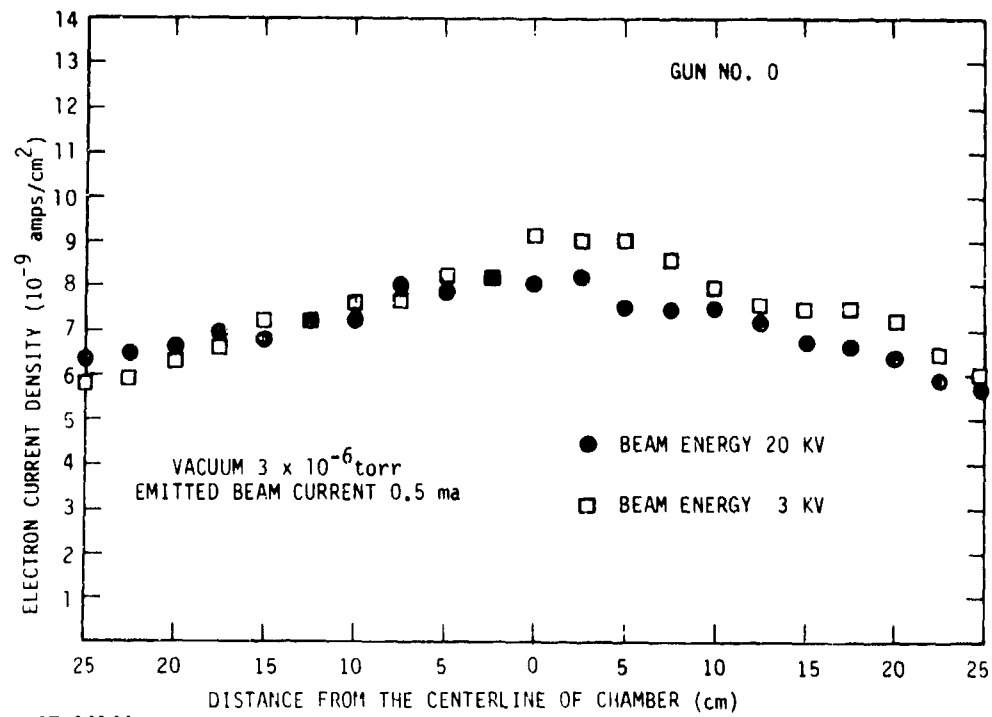
RT-16144
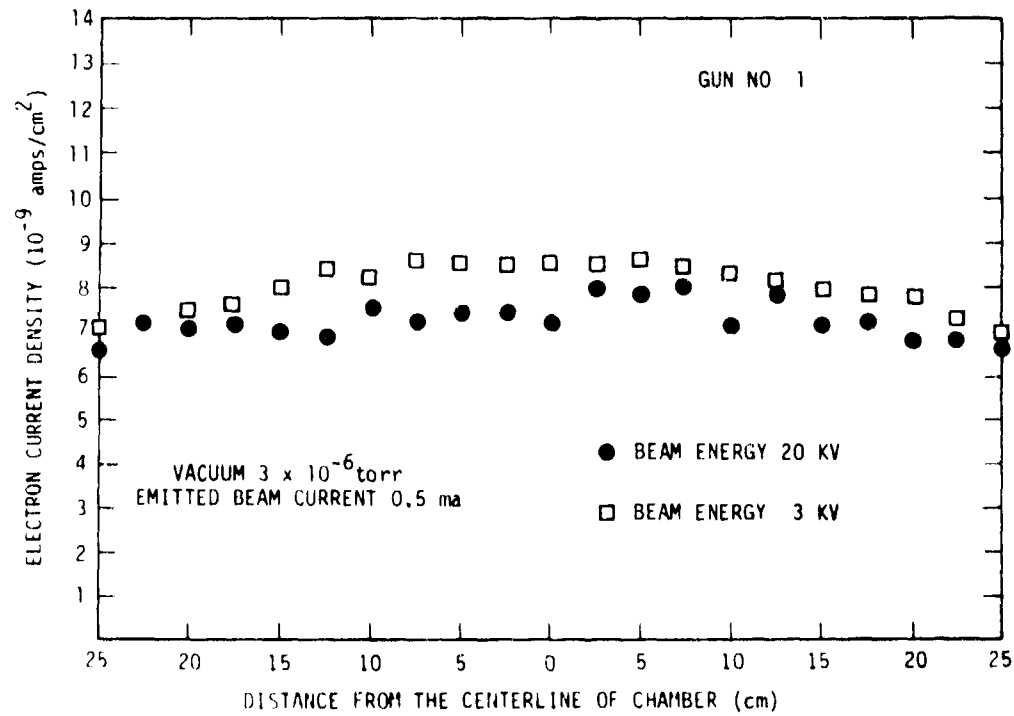
RT-16143

Figure 4. Calibration of electron guns

GRID

EMITTER

ANODE

GRID

C

B

A
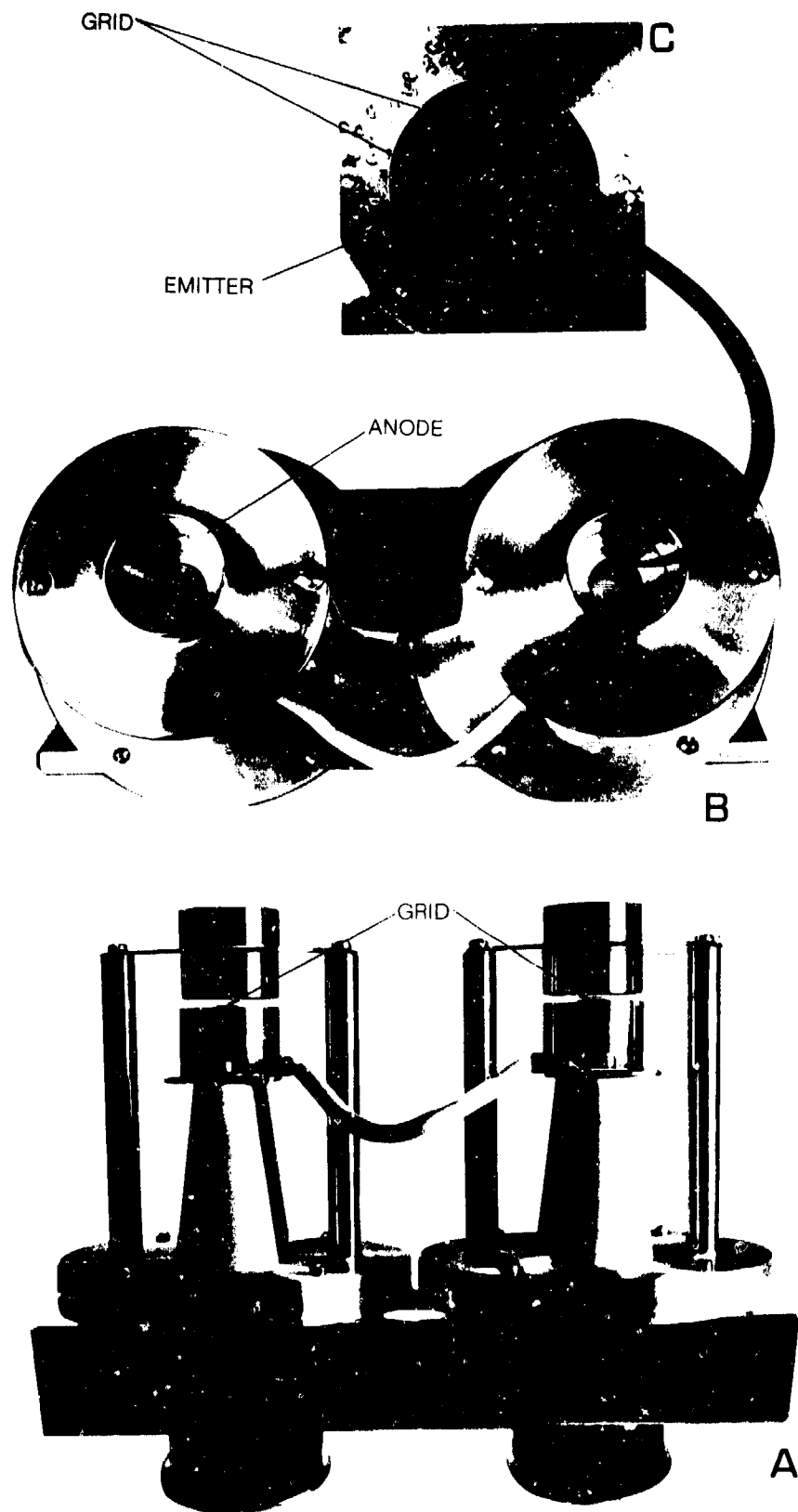
Figure 5. Electron guns (view C is an enlarged detail of view B to show the emitter and grid)

18
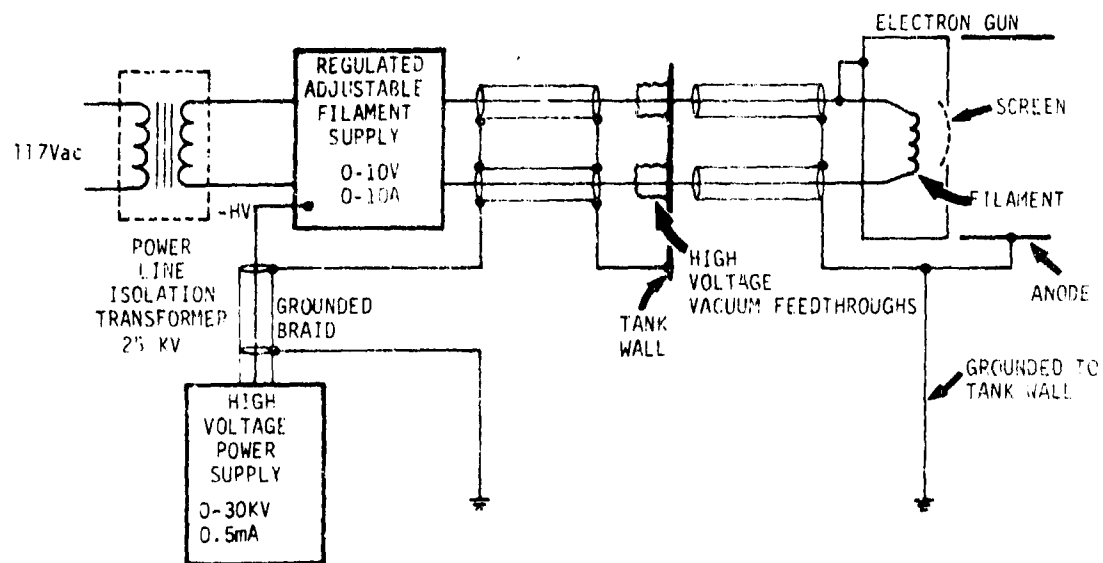
RT-16206-1

Figure 6. Circuit diagram of electron gun and associated wiring and power supplies

3.4 POLYMER FILM SAMPLE MOUNT

The method for contacting the samples to the sample-mount-heat sink is shown in Figure 7. Figure 3, Item B, shows the completed assembly, except for the electron beam collimators which have been removed to show the complete sample.

The sample mounts, Figure 7, are attached to the grounded heat sink by six screws. The sample mount consists of two aluminum plates separated by 0.64 cm (0.25 inch) of Emerson and Cuming Stycast 2850FT which has a high thermal conductivity but is electrically insulating (volume resistivity is $\sim 5 \times 10^{16}$ Ω-cm). The top aluminum plate that contacts the rear sample electrode is slightly domed (radius ~ 193 cm) to ensure uniform sample contact with the heat sink. Electrical isolation provided by the epoxy allows the back sample electrode to be either grounded or biased. The central region of the sample mount was originally guarded as shown in the figure to avoid leakage paths to the grounded heat sink for measurements where the back sample electrode is biased. However, the distance of the collimator from the sample surface resulted in the exposure of a ~ 2 mm wide ring of unelectroded sample material and permitted breakdown for incident electron energies of $\geqslant 10$ keV. This problem was corrected by attaching a 7.6 cm (3 inch) diameter stainless steel ring to the collimator plate that extends down to ~ 3 mm from the front electrode of the sample. The front sample electrode was also enlarged slightly to have a diameter 6 mm larger than the

19

collimator ring. This was done to keep the edge of the sample electrode, which is a high field region, away from the grounded collimator ring. The collimator ring near the sample surface has a radius equal to one-half of its wall thickness and was electro-polished to remove any sharp points that could induce premature breakdown. With this configuration, no breakdowns were observed when the front surface was at or near ground potential for irradiations up to 27 keV.
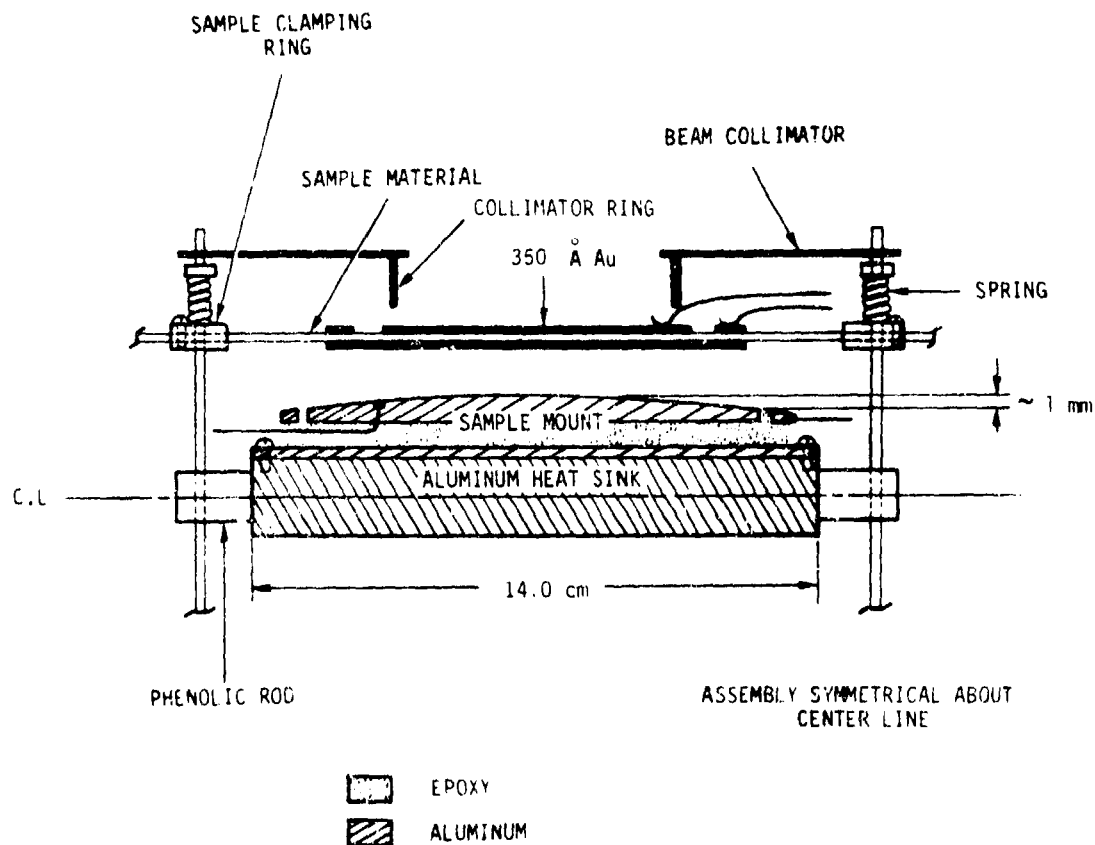
RT-16122-1

Figure 7. Heat sink, sample-mount and sample assembly

The sample is held in clamping rings whose inside diameter is 16.5 cm (6.5 inches), which leaves approximately a 2.5 cm (1 inch) band of nonelectroded sample material between the sample electrodes and the grounded clamping rings. The clamping rings, containing the sample, are held in position by three threaded rods that pass through phenolic rods attached to the heat sink. The sample is held in contact with the sample mount by three springs and take-up nuts on the threaded rod. The threaded rod also supports the collimators for the electron beam.

3.5 POLYMER SAMPLE PREPARATION

The polymer samples were commercially available films of types employed on spacecraft surfaces. These included FEP Teflon (89 percent polytetrafluoroethylene, 11 percent hexafluoropropylene copolymer), Type S Mylar (polyethylene terepthalate), and Kapton H (polypyromellitimide). The samples were manufactured by E. I. duPont deNemours and Company. No information about date of manufacture or lot number was available.

Gold electrodes were deposited on each face. Gold was chosen because it was desired to have a contact which was a good conductor but relatively transparent to UV. However, the dense gold film complicated the interpretation of the measurement because of the significant amount of backscatter, secondary emission production and of a small amount of trapping of the primary electrons. The electrodes were in most cases ca. 350 Å (± 10 percent) thick. Electrode thicknesses were measured with a quartz crystal thickness monitor.

The electrodes were deposited from a heated tungsten boat approximately 30.5 cm (12 inches) from the sample. Prior to applying the electrodes, the sample was mounted in the sample clamping rings and cleaned. The masks used to define the contact area were made of magnetic material and held in place by permanent magnets. During electrode deposition, the entire sample surface not electroded was covered to avoid contamination. The front sample electrode (when unguarded as was the case for most measurements) is about 8.9 cm (3.5 inches) in diameter. Only the central 7.6 cm (3 inch) diameter was irradiated (41.9 cm^2 area).

3.6 TEMPERATURE CONTROL SYSTEM

The experimental program required temperature-dependence measurements between $200^{\circ}K$ and $300^{\circ}K$ for the majority of the samples and $200^{\circ}K$ to $600^{\circ}K$ for fused silica samples. An Air Products LT-3-110 Liquid Transfer Cryotip (Figure 8) with liquid nitrogen as the coolant is used to achieve sample temperatures below $300^{\circ}K$. The cryotip is mounted vertically through a port in the top of the exposure chamber to position the heat sink-sample assembly at the centerline of the exposure chamber. The sample heat sink attached to the cold finger of the cryotip is a 14.0 cm (5½ inch diameter), 1.9 cm (3/4 inch) thick aluminum plate. Two 150 watt cartridge heaters and a thermocouple are embedded in the heat sink for temperature control and monitoring. With liquid nitrogen as a coolant, the heat sink-sample assembly cools to $\sim 150^{\circ}K$ in

1-1/2 hours. Temperatures as low as $100^\circ K$ could be reached. The heat sink accommodates a sample holder (Figure 3, Item B) on each face, so that two samples can be installed at one time. This feature, plus the ability to rotate the cryotip 180 degrees allows measurement and irradiation of two samples with a single pumpdown.

(1) NITROGEN DEWAR
(2) NITROGEN CYLINDER
(3) PRESSURE REGULATOR
(4) MERCURY MANOMETER, 0 TO 500mm Hg
(5) VACUUM SHROUD
(6) VACUUM SHROUD PUMP
(7) VACUUM PUMP FOR OPERATION BELOW 4.2°K
(8) ACCESSORY FLOW CONTROL PANEL
(9) ACCESSORY TEMPERATURE CONTROLLER
     MANUAL OR AUTOMATIC
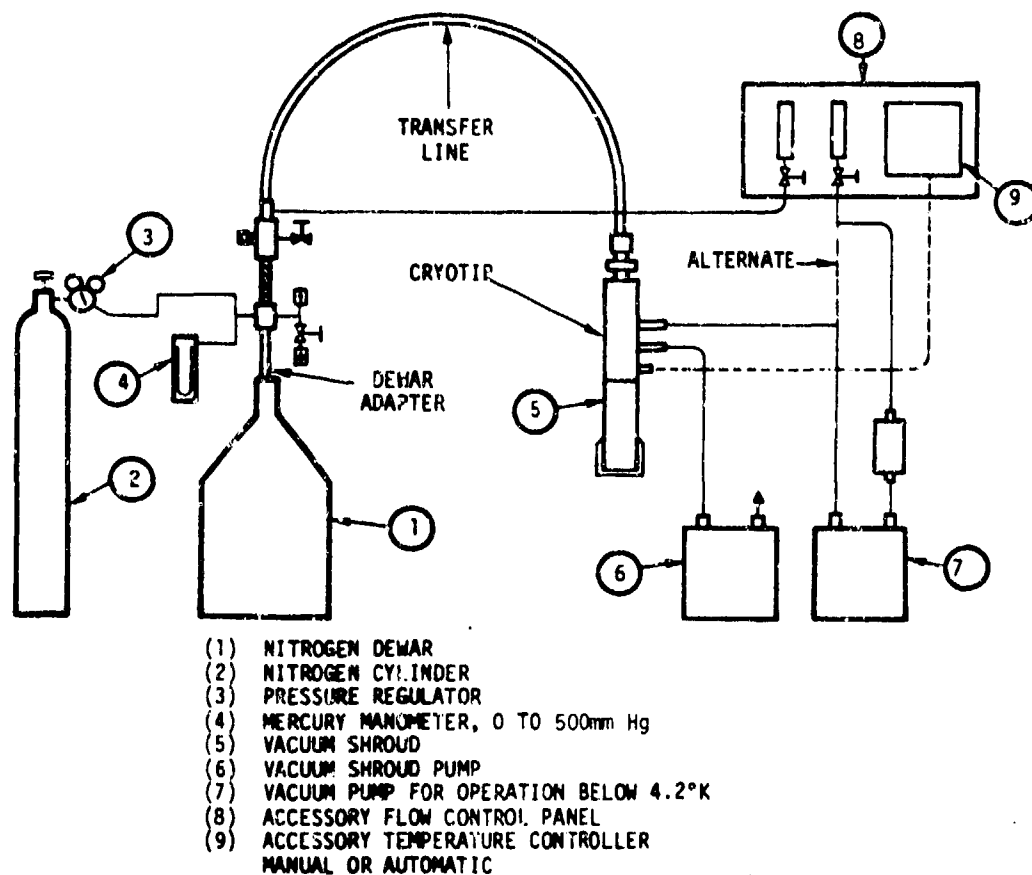
RT-15259

Figure 8. Cryostat system for maintaining samples at a constant temperature. In the experiment to be carried out, the vacuum shroud (5) is removed as the cryotip itself is in the vacuum of the irradiation chamber.

3.7 UV SOURCE

A solar simulator consisting of a Varian 300 watt Xenon arc lamp (VIX300 UV) and a Johnson filter was provided. The lamp uses an internal aluminum parabolic reflector and a sapphire window to maximize UV output. The Johnson filter is used to suppress the Xenon lines and to tailor the source output to match the solar spectrum. The lamp was chosen to provide an intensity at the sample surface of about one solar constant (AM0).

3.8 FUSED SILICA SAMPLE MOUNT

A different sample mounting arrangement was designed for the fused silica (Corning 7940) samples for two reasons.   First, the samples were smaller (5 cm x 4.5 cm) and thicker (0.014 cm) than the polymer films and hence relatively inflexible.   Second, a supplemental electrode system was provided in front of the sample to supress secondary electron (those emitted with energies $\leqslant 50$ eV) emission to eliminate one of the factors which limited the accuracy of the polymer film measurements.

An aluminum electrode 214 Å thick and 2.5 cm in diameter, with tab for electrical connection (see Figure 9), was evaporated onto the front surface of the SiO_2 wafer. The front electrode was changed from gold to aluminum to minimize secondary emission and backscatter entrance transmission (cf. subsections 4.2 and 5.1). The back surface is completely covered by a 7924 A thick evaporated gold electrode.

The SiO_2 target is electrically insulated from the target support assembly by an AD-96 alumina insulator (Coors Porcelain Company) 5.08 cm square by 0.074 cm thick. A gold electrode, evaporated on the front surface of the insulator mates with the rear electrode of the SiO_2 target and serves as the point of electrical contact. Electrical connection with both the front and back electrodes is made by means of gold-plated molybdenum spring clips, as shown in Figure 9. The potential of the targets' front electrode can be adjusted by means of a battery box (see Figure 10). In series with the battery box is a 27.5 pf air capacitor that can be short circuited by means of a mechanical switch. This capacitor formed part of the capacitive voltage divider used for the open circuit measurements.

The SiO_2 target and alumina insulator are affixed to a copper thermal block by two spring clips (-160, -170 in Figure 9). The temperature of the target can be varied from $200^{\circ}K$ to $600^{\circ}K$ by thermal conduction and is measured by a chromel-alumel thermocouple mounted in the center of the copper block.

There are two electron lenses in front of the target. The first lens is at ground potential and serves as a mask to define the effective area of target irradiation (2 cm^2). The second lens is at -740 volts with respect to the target's front electrode and suppresses secondary electrons with energies of less than 200 eV which are emitted from the target. To show the effectiveness of these lenses in suppressing secondary emission, for an incident 10 keV electron beam of constant current, the sum of the front and rear electrode currents $(I_1 + I_2)$ remained constant even though the front electrode potential relative to tank ground (V_1) was varied between $\pm 500V$.

LN$_2$ RESERVOIR

(150)

(140) SHIELD

BRAZE WITH BT SOLDER
(72 Ag 28 Cu)

.25 OD X .135 ID X .50
ALUMINA TUBE (8 REQ)
.125 OD X .063 ID X 1.00
ALUMINA TUBE (4 REQ)

1/8 O.D X .026 WALL
COPPER TUBE X 11 LONG
BRAZE WITH BT SOLDER

BC 50141 SOLID COAXITUBE
PRECISION TUBE CO INC.

SHIELD

(110) BASE PLATE

NOTE: DIMENSIONS ARE INCHES UNLESS OTHERWISE SPECIFIED.

(130)

ELECTRICAL
SPRING CLIP

E1E43 CARTRIDGE HEATER
WATLOW PRODUCTS (2 REQ)

2-56 UNC RD HD SS SCREW
X 1/4 LONG (8 REQ)

SiO$_2$ FUSED QUARTZ TARGET
5 CM X 4.5 CM X .020 CM

0-80 UNF SS NUT
(16 REQ)

ELECTRICAL
SPRING CLIP

0-80 UNF SS STUD
X 1-5/8 LONG X 3/8
LONG THREAD EACH END
(4 REQ)

6-32 UNC SS FLAT HD
SOCKET CAP SCREW X 1/4
LONG (2 REQ)

(120) LENS

AD-96 ALUMINA INSULATOR
2 X 2 X .025 (1 REQ)
COORS PORCELAIN CO.

(160) SAMPLE CLIP

6-32 UNC SS BUTTON HD
SOCKET SCREW X 1/2 LONG
(2 REQ)

RT-19665

Figure 9. Target support assembly
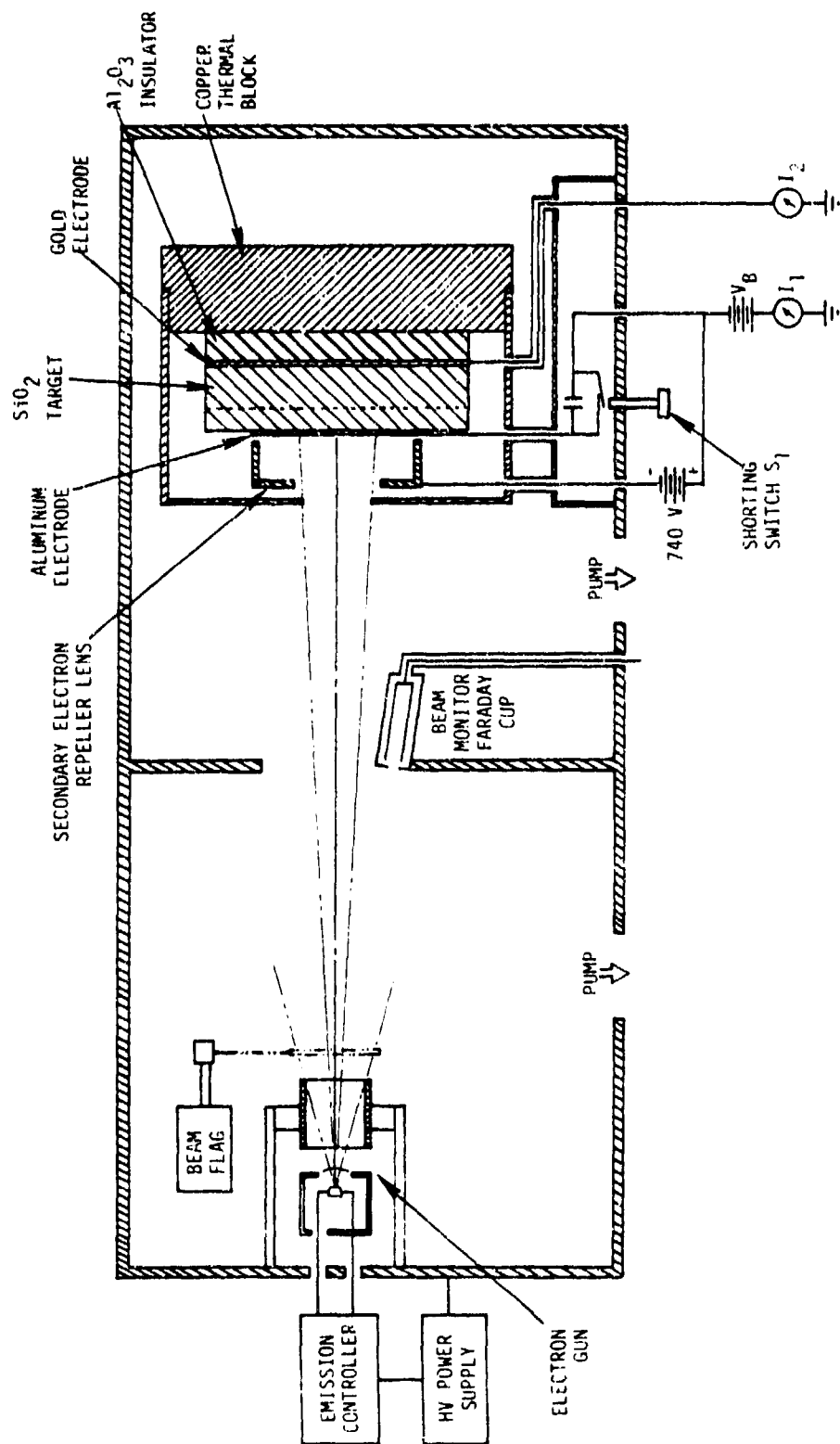
Figure 10. Irradiation configuration for SiO_2 irradiations

3.9 CURRENT AND VOLTAGE MEASUREMENTS

Two measurement configurations were employed based on the techniques developed by Gross, Sessler and West (Ref 24). They are shown in Figure 11. In the short circuit method current flowing from both the front and rear electrodes, I_1 and I_2, respectively, were measured. Keithley 640, 610, or 642 electrometers were used for the current measurements. They have a sensitivity of a few tenths of a picoampere, being limited by noise associated with the use of coaxial cables. The front surface of the sample could be set at voltages relative to ground between -520 V and +520 V with a battery box whose cells were carefully isolated to minimize extraneous leakage currents, equivalent to applied fields of up to 0.8 MV/cm in the thinnest samples.

(a) SHORT CIRCUIT

(b) OPEN CIRCUIT
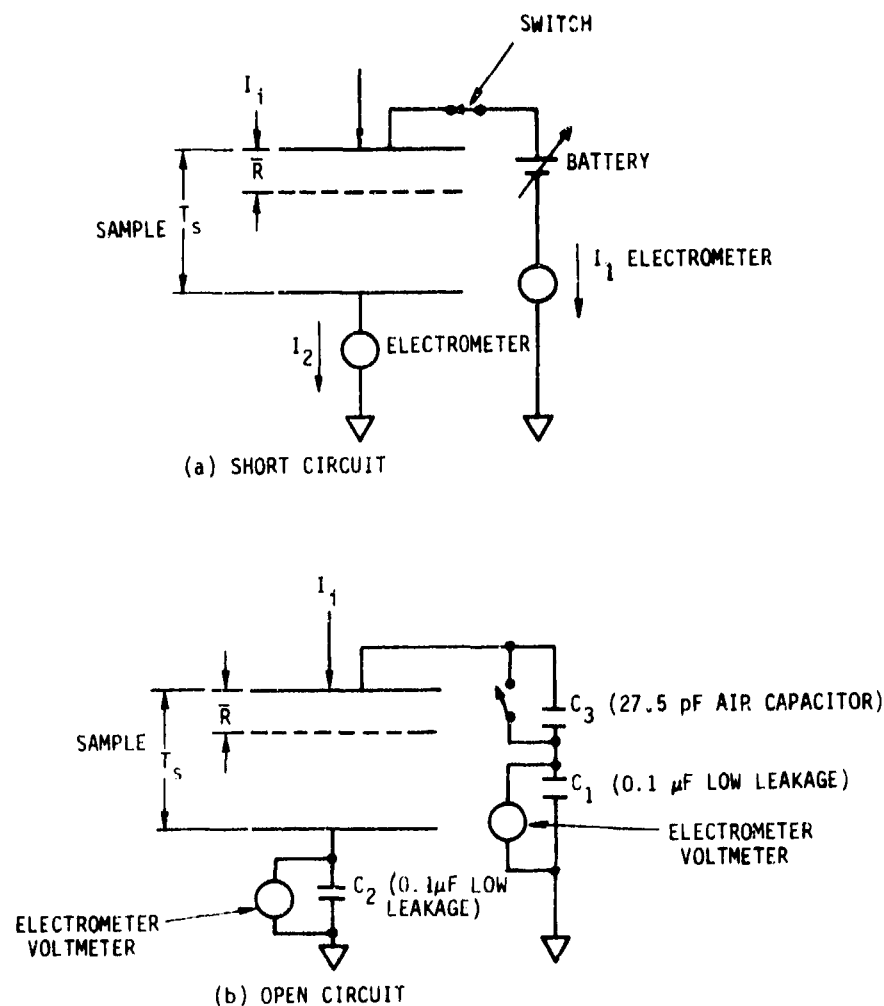
RT-15260-3

Figure 11. Experimental measurement configurations

The incident current impinging on the sample (I_i) was determined from beam mapping with the five Faraday cup array (Figure 3, Item E) and monitored with the rotatable single Faraday cup (Figure 3, Item D). In this configuration, measurements of I_1, I_2 and the net back emitted current I_b were made as a function of V_1, sample temperature T, and incident beam current and energy E_i. I_b was determined by a method described in subsection 4.2.

In the open circuit configuration, front surface potential during charging was monitored with a capacitative voltage divider consisting of a 27.5 pF high voltage air capacitor (C_3) and a 0.1003 μF low leakage Teflon capacitor (C_1). The rear electrode was connected to ground through a low leakage capacitor C_2. By themselves, C_1 and C_2 are low impedance charge measuring devices. The voltages across C_1 and C_2 were measured with either Keithley 640 or 642 vibrating capacitor electrometers which have input resistances of greater than 10^{16} ohms, more than a factor of 100 greater than those of C_1 or C_2.

The output of the electrometers as well as that of the Faraday cups monitoring incident and back-emitted current were recorded as a function of time on strip chart recorders or a multichannel digital data logging system.

As $C_3 \ll C_1$, the capacitance of the combination is $\simeq C_3$. In addition, C (sample) was typically a few nF. Hence the parallel combination of C (sample) and (C_1, C_3) is essentially C (sample). In this configuration, the front surface potential, neglecting leakage, is equal to

$$V_1 = V_{C1}\left(1 + \frac{C_1}{C_3}\right) , \tag{1}$$

where V_{C1} is the voltage across C_1. The net charge deposited, Q_0, in a time t is

$$Q_0 = (I_i - I_b)t = C_2 V_2 \tag{2}$$

where V_{C2} is the voltage across C_2 and Q_2 its charge. This charge is not identical to that actually trapped in the dielectric Q_t because of leakage of injected charge to the rear sample electrode and because of emission of secondary electrons from the front electrode.

In some cases, irradiations were performed with the front electrode switch open, and then closed. The resultant changes in I_1 and I_2 were used to determine the radiation-induced conductivity (Figure 11a). Changes in Q_1 and Q_2 were used to determine the injected charge centroid $\overline{R}$ in a sample of thickness T_s.

4. MATERIAL PARAMETER MEASUREMENTS

The determination of material parameters relevant for the transport of charge in polymeric insulators exposed to energetic electrons is described in this section. These parameters include average depth of charge deposition, dark conductivity, radiation conductivity and delayed conductivity. These quantities are derived on the basis of a relatively simple model developed by Gross and co-workers (Refs 21,24,25). It is to be emphasized, however, that this is only one model for interpreting the data. Other more sophisticated approaches based on detailed transport calculations will undoubtedly give more accurate agreement with the experimental data. Because we are aware of this fact, we have, where possible, identified the limitations and inaccuracies in the modeling approach.

4.1 DISCUSSION OF THE MODEL

For the purpose of evaluating the experimental data the following model is presented. It is shown schematically in Figure 12. A monoenergetic and uniform beam of electrons is incident normally on the dielectric sample. Beam energies ranged from 5 to 27 keV. The sample itself has a layer of gold film deposited on its surface which was typically 350 $\mathring{A}$ ± 10 percent thick. The polymer samples themselves were for the most part thicker (6.25 to 25.4 μm) than the practical range of the incident electrons so that the beam was stopped in the sample. The resulting charge distribution represents both a source for an internal field and a reservoir of space charge.

In the model, the sample is divided into two regions. The boundary between the irradiated region A, and the unirradiated region B is taken to be a plane located at a depth ($x = \bar{R}$ from the front face. $\bar{R}$ is the centroid of the injected charge. In reality, this plane is not fixed, but varies as a consequence of charge rearrangement taking place during and after irradiation.

A fraction β of the incident electron flux is backscattered from the interior of the sample up to a depth equal to half that for electrons of incident energy E_i, yielding a backscatter current $I_\beta = \beta I_i$. A secondary electron current $I_\delta = \delta I_i$ is also produced.
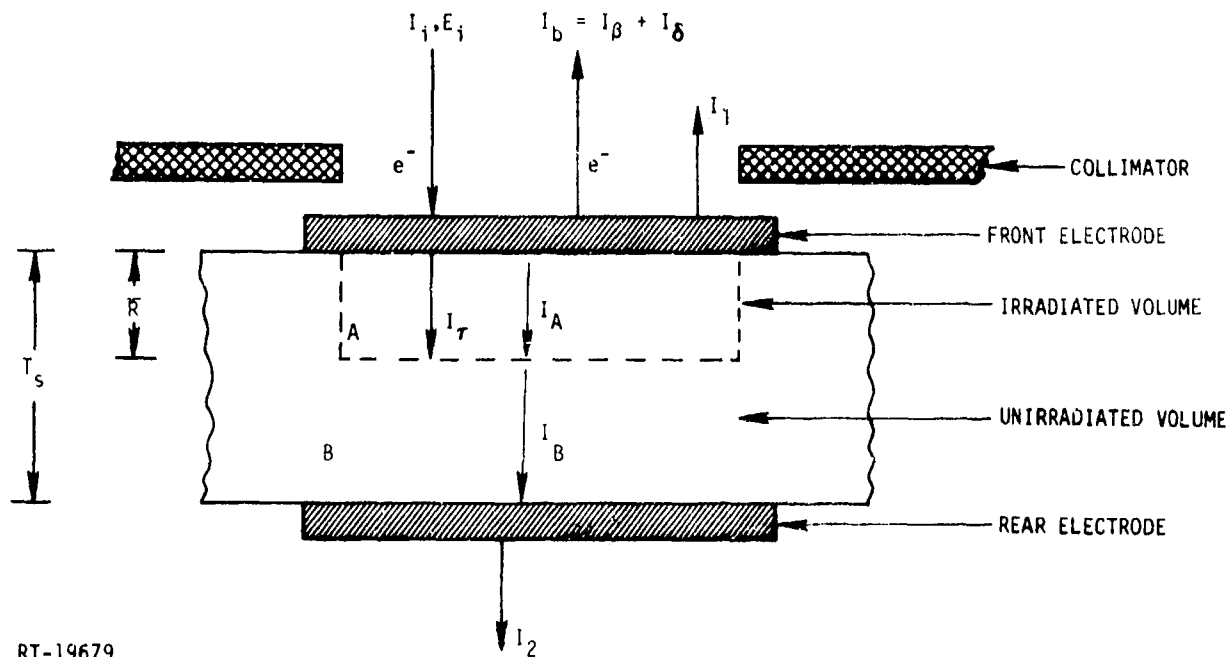
Figure 12. Charging model

The net back emitted current $I_b = I_\beta + I_\delta$. In addition, a small fraction α of the incident beam is stopped in the front electrode. The resultant current I_α becomes part of that leaving the front electrode I_1. Except at low energies (<10 keV), the data of Cosslett and Thomas (Ref 26) indicates that α is a few percent and hence negligible given the overall accuracy in measuring currents (a few percent). Passage of the primary beam through the electrode causes an energy loss, and energy dispersion which is more significant at lower energies ($E_i < 10$ keV) than at higher ones. This in turn leads to a further dispersion in charge and dose deposition above that for a mono-energetic beam normally incident on the unelectroded polymer.

The current responsible for producing charging effects in the dielectric I_τ is

$$I_\tau = I_i - I_\beta - I_\alpha \quad . \tag{3}$$

In fact, what is measured is the net charging current I_o given by

$$I_0 = I_i - I_b = I_1 + I_2 \quad . \tag{4}$$

30

The manner in which I_0 is determined is discussed below. In our data, we have corrected for the effects of backscatter analytically by computing the net sample injection current

$$I_t = I_i - I_\beta = I_0 + I_\delta \quad , \tag{5}$$

where I_δ is calculated. In the evaluation of the date we have assumed that $I_t \simeq I_\tau$ and these quantities are used interchangeably. In fact $I_t = I_\tau + I_\alpha > I_t$. The absorbed current is added to I_i.

The net solenoidal current in region A, I_A, can be written as

$$I_A = I_\tau + A \cdot \left(g_A E + \mu \rho E + \epsilon \frac{\partial E}{\partial t} \right) , \, t \leqslant x \leqslant \overline{R} \quad , \tag{6}$$

where A is the sample area, t the thickness of the front electrode, g_A the net conductivity with both a dark and radiation-induced component, $\mu_A \rho E$ the effective spacecharge limited current density, with $\rho(x,t)$ the spacecharge density μ_A the effective trap modulated mobility for the predominant charge carrier in region A, $E(x,t)$ the electric field and ϵ the dielectric constant. The last term in Equation 6 is the displacement current which is assumed to vanish when charging equilibrium is reached.

The net solenoidal current in region B (I_B) is

$$I_B = \left(g_B E + \mu_B \rho E + \epsilon \frac{\partial E}{\partial t} \right) \cdot A \quad , \, \overline{R} < x \leqslant T_s \tag{7}$$

where the terms are defined analogously to those for region A. Note that the continuity equation requires that

$$I_0 - I_1 = I_A = I_B = I_2 \quad . \tag{8}$$

Thus, the measurements consist in determining the internal transport parameters μ, g, $\overline{R}$ in the two regions from the measured external quantities, I_i, I_b, I_1, I_2 or Q_1, Q_2 as a function of applied bias V_1 and sample temperature using the approximations described below. These are:

31

1. The injected current deposits a charge distribution $\rho(x)$ in the material. For purposes of analysis, this continuous charge distribution is replaced by a planar charge distribution σ such that

$$\sigma = \int_0^{T_s} \rho(x)\, dx \quad , \tag{9}$$

located at a depth $\bar{R}$ where

$$\bar{R} = \int_0^{T_s} \rho(x)\, x\, dx \Big/ \int_0^{T_s} \rho(x)\, dx \quad , \tag{10}$$

the mean depth of the space charge field, $\bar{R}$ is not constant but depends on charge rearrangement taking place during and after irradiation and need not be equal to the average range of the primary electron beam. However, for analysis purposes, $\bar{R}$ will be so defined. Examination of $\bar{R}$ vs R_p, the practical range as determined by transport calculations, indicates that $\bar{R}$ is typically 50 to 65 percent of R_p (cf. Table 5) for the materials and electron energies of interest. This planar charge is a virtual electrode capable of injecting charge carriers into region B. An injecting electrode in this idealization is effectively a plane where E is zero and ρ infinite (Ref 25) such that the product of $\rho \cdot E$ is finite as required by the continuity equation. For certain values of applied potential V_1, E changes discontinuously at the interface between regions A and B such that

$$E(\bar{R}_+) = \lim_{\epsilon \to 0} E(\bar{R}+\epsilon) = 0 \quad .$$

2. The dose rate is assumed constant in the irradiated volume (Region A) and zero in Region B. It was taken to be equivalent to deposition of the total beam energy in a layer whose thickness is equal to R_p. Then the dose rate $\dot{D}$ in rads/sec is given by

$$\dot{D} = 0.1\, \bar{E}_t J_t / (R_p - t) \tag{11}$$

where $\overline{E}_t$ is the average beam energy in kV after passage through the front electrode, J_t is the injected charge per unit area in na/cm^2, R_p is the practical range in g/cm^2, t the thickness of the front electrode in g/cm^2.

3. The radiation-induced conductivity is that for steady state which is attained in a few seconds after the start of irradiation. The conductivity g_D is given by (Ref 27)

$$g_D = K_D \dot{D}^\Delta \quad , \tag{12}$$

where K_D is a constant, and $0.5 \leqslant \Delta \leqslant 1$ depending on the energy distribution of traps.

The dark conductivity g_{A0} in region A can be written (Ref 28)

$$g_{A0} = g_{00} \left[\frac{2 + \cosh (\beta_F E^{1/2}/2 \, kT)}{3} \right] \quad , \tag{13}$$

with g_{00}, the dark conductivity at low fields, T the absolute temperature and $\beta_F = (e^3/\pi \epsilon)^{1/2}$, the Frenkel parameter. A similar expression holds for g_{B0}, the dark conductivity in region B. However, $g_{B0} \ll \mu_B \rho$ and is ignored.

4. The delayed conductivity $\overline{g}(t)$, i.e., that which persists in the irradiated region of the polymer after irradiation, has been fit to a function of the form (Ref 29)

$$\overline{g}(t) = \overline{k} g_D (1 + bt^\gamma)^{-1} \tag{14}$$

where g_D is the quilibrium value of the radiation-induced conductivity in region A during irradiation, $\overline{k} \leqslant 1$ takes into account that thermal equilibrium between conduction electrons and holes is not instantly established (Ref 24) and b and γ are constant. Typically, γ is set equal to 1 for the bimolecular recombination of electrons and holes.

5. After irradiation for times of ~ 0.5-1 hour, a quasi-equilibrium state is reached in which I_1 and I_2 become constant. In the model, this is equivalent

to setting the $\partial E/\partial t$ terms in Equations 6 and 7, representing the displacement currents equal to zero.

6. The normal dark conductivity in polymeric insulators is typically less than $10^{-17}\,(\Omega\cdot cm)^{-1}$ after the relaxation of charging transients. Even with electric field enhancement, under the irradiation conditions relevant for these measurements, $g_{A0}\ll g_D$ (cf. subsection 4.4). In addition, it has been shown (Ref 24) that the effective space charge conductivity term $\mu_A \rho \ll g_D$. Then the predominant conductivity mechanism in region A is due to the creation of charge carriers by ionizing radiation, here assumed deposited with uniform dose leading to a dose rate dependent conductivity given by Equation 12.

7. Some current reaches the rear electrode. The data presented in Section 5 shows that $I_2 \ll I_1$ until the effective range of the beam $\overline{R} > T_s/2$ in which case I_2 becomes comparable in magnitude. This data suggests that two limiting cases be considered. In the first $I_2 \ll I_1$, conduction in region B is primarily through the normal dark conductivity, albiet field enhanced, given by Equation 13. As the beam becomes more penetrating, space charge limited charge transport predominates. In this case, the plane of deposited charge acts as a virtual electrode. Depending on the polarity of the external applied bias electrons or holes will be pulled into the nonirradiated region B. The conductivity is then effectively $\mu_B \rho$. Because the trap modulated mobility μ_B is different for electrons and holes in a given material, μ_B can assume two values, one for holes and the other for electrons.

8. Kirchoff's first rule requires

$$\int_0^{T_s} E(x,t)dx = V_1 \tag{15}$$

We now describe the manner in which material parameters were obtained from the measured quantities I_1, I_2, I_o, I_b. In the discussion which follows, some data is expressed in terms of current densities (amps/cm^2). If I_k is a particular current term, the equivalent current density is given by J_k. The arrows in Figure 12 show positive current flow for each of the components of interest.

4.2 DETERMINATION OF INJECTION CURRENT AND DOSE RATE

This section discusses the manner in which I_t, the injection current and $\dot{D}$, the mean dose rate in the irradiated region of the sample were determined. The question of the accurcy of assumptions of uniform dose deposition and monotonic charge deposition are also examined through a comparison of the experimental results for I_i and I_b with experimental data on the backscatter, absorption and transmission of keV electron beams in gold films and with calculations of beam transport made with the SANDYL Monte Carlo transport code.

The net injection current deposited in region A of the sample is given by Equation 3 or in our approximation by Equation 5. Passage of the beam through the gold foil front electrode not only causes attenuation because of backscatter, but alters the measured value of I_1 because of secondary emission from the front surface and partial stopping of the beam in the electrode. One needs to determine I_t and $\overline{E}_t$ to obtain $\dot{D}$.

When irradiating samples with electrons in the energy range of 5 to 30 keV the back emission current I_b is large and is a strong function of the incident electron energy. Back emission is defined as the sum of the backscattered and secondary emission currents. It was necessary to measure this current in order to understand the charging dynamics of the system. This is especially true for an experimental sample configuration such as ours in which the front electrode is a high density, high atomic number metal. In addition, some of the emitted secondary electron current was recollected by the front electrode for $V_1 > 0$, producing a systematic error in meter current unless properly accounted for. In order to interpret our measurements it is required that the back-directed current be known in order to obtain the value of current I_t that actually enters the irradiated volume of the sample.

A Faraday cup was installed off the sample-beam axis to sample the back-directed current. This Faraday cup was calibrated as a function of incident electron energy as follows. The calibration requires an accurate measurement of the incident beam current density (J_i) and the current flowing from the front irradiated electrode to ground (I_1) while applying bias to this electrode. The circuit used for the measurement and the data obtained for a 15 keV irradiation is shown in Figure 13. In Figure 13, the measured current I_1 is converted to current density J_1 by dividing by the sample area, 42 cm^2. Prior to irradiation, the electron beam is mapped with a five-Faraday-cup array that is remotely placed in front of the sample to measure beam uniformity and current density. During beam mapping and sample irradiation, a fixed-position Faraday
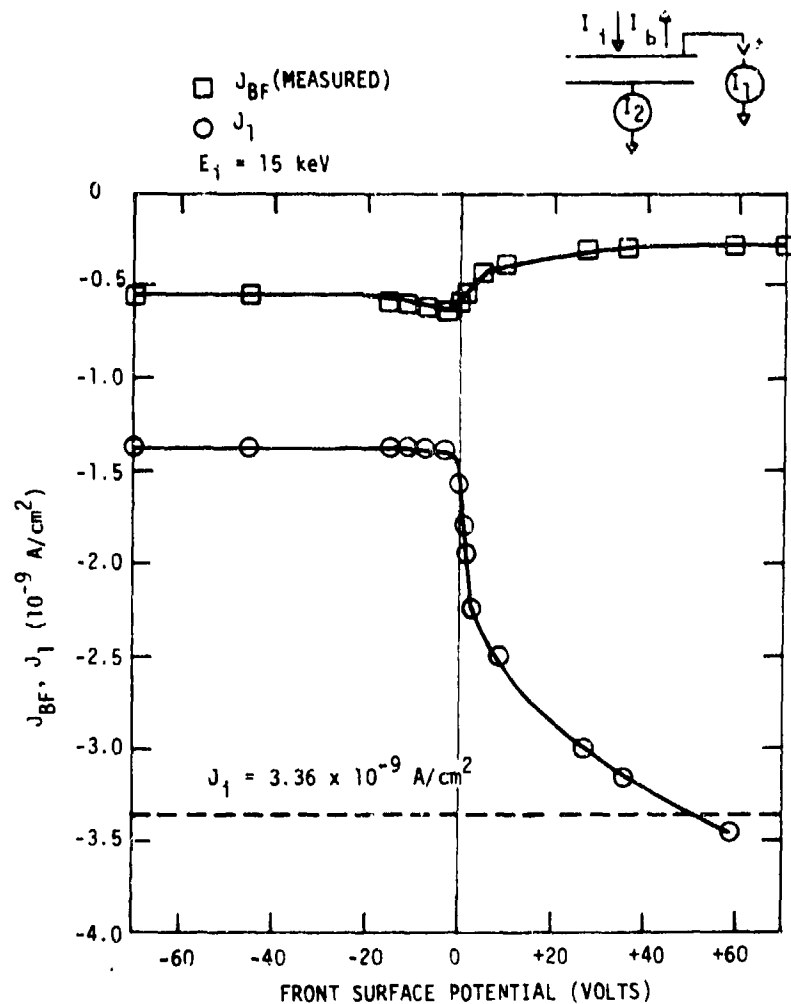
Figure 13. Faraday cup and front electron current densities versus front electrode bias for a Mylar sample with 350Å gold electrode.

cup samples the beam. The current density monitored by this Faraday cup J_{BF} is equal to I_{BF} divided by collector area 0.456 cm^2. The output of this Faraday cup is continuously monitored during irradiation to provide the actual beam current density on the sample at all times. Typical beam uniformity over the sample surface is better than ±10 percent, and constant to within a few percent over several hours.

The total current in the circuit shown in Figure 13 is

$$I_1 = I_i - I_b - I_2 \quad , \tag{16}$$

36

The sign convention is such that a positive incident current is into the sample while positive components of other currents are out. Equation 16 is essentially Kirchoff's first law. For a 1 mil thick sample and electron energies up to 20 keV, i.e., where the practical range is much less than the sample thickness, $I_2 \ll I_1$ or I_i and can be neglected. The net charging current (I_o) of the sample is

$$I_o = I_i - I_b \simeq I_1 \qquad . \qquad (17)$$

The relationship between J_i, J_1, and J_b for a 15 keV electron beam and a 0 to ± 70 volt front surface potential is shown in Figure 13. During these measurements the incident beam current density was constant at 3.36×10^{-9} A/cm^2. The calibration factor for the Faraday cup that measures the back-directed current is obtained from the negative bias region of Figure 13. J_1 decreases with negative bias and becomes constant for negative bias greater than -50 volts. At this point, all of the secondary electrons produced at the front surface of the sample are being driven away from the surface and are being sampled by the Faraday cup. The commonly accepted definition of secondary electrons are those emitted with energies of <50 eV. Nearly all backscattered electrons created by keV electron beams incident on metal films have energies which are a significant fraction of the incident beam energy (Ref 30). The fraction sampled by the Faraday cup, of course, depends on the angular dependence of emission and the solid angle subtended. Therefore, under these specific conditions one can calculate the magnitude of the back-directed current density,

$$J_b \simeq J_i - J_1 \qquad , \qquad (18)$$

and thus obtain a calibration factor for the Faraday cup. This was done at large negative voltages to ensure that all secondary electrons were repelled from the front face of the sample.

$$
\begin{aligned}
k &= \frac{J_i - J_1}{J(F.C.)} \\[2mm]
&= \frac{-3.36 \times 10^{-9} + 1.37 \times 10^{-9}}{-5.58 \times 10^{-10}} \\[2mm]
&= 3.57 \qquad . \qquad\qquad (19)
\end{aligned}
$$

Experimentally determined values of k are given in Table 3, where $I_b = I_i - I_1$ was determined for large negative front electrode voltages ($V < -300$ volts). The data shown in Table 3 are independent of polymer sample and show a relatively small dependence on the incident beam energy. This indicates that the back emission of electrons is determined by the gold electrode and that the angular emission of electrons is relatively constant as a function of incident beam energy.

Table 3. Measured Calibration Factors for the Faraday Cup

Kapton		FEP		Mylar	
E(keV)	k	E(keV)	k	E(keV)	k
6	3.28	5	3.48	5	3.50
13.5	3.33	10	3.25	10	3.47
20	4.22	15	3.63	15	3.57
		20	3.82	20	3.90
Mean	3.61		3.55		3.61

Measurement of I_b yields the sum of I_η and I_δ. In order to determine I_t, I_δ must be determined. This was done by calculation. In Figure 14 we have plotted $(I_o/I_i) + \delta$ as a function of beam energy for all samples and incident energies examined. For comparison, we have plotted τ, the fraction of electrons transmitted through a 350 Å thick gold foil as determined experimentally by Cosslett and Thomas (Ref 26), corrected for backscatter from the polymer film using the formula

$$= \frac{\tau'(1-r)}{(1-r\beta')} \tag{20}$$

where τ' is the experimentally determined value of the transmission coefficient of the gold foil, β' the backscatter coefficient for the metal (β' is less than the thick target backscatter coefficient), r is the thick target backscatter coefficient for the various polymer films and δ is the secondary electron coefficient for gold. A value of r = 0.05 was used in all of the calculations based on a series of SANDYL calculations for backscatter from the various polymers as a function of energy. This agrees reasonably well with the predictions using the relationship

$$r = 0.1 E_i^{-0.2} \tag{21}$$

38
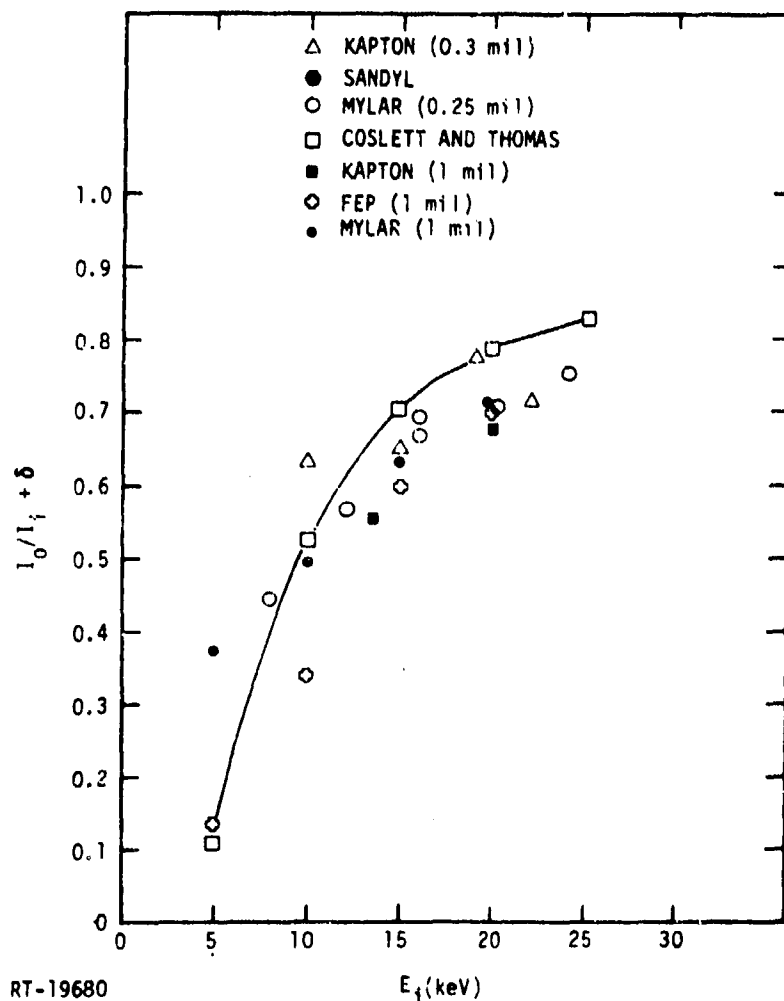
Figure 14. Fraction of electrons transmitted through the gold foil electrode

given in Reference 18, and in any event represents a small correction. It was more difficult to determine δ for gold because experimental values varied by more than a factor of two between experimenters. We employed the relationship

$$\delta = \frac{\Delta X}{\epsilon} \frac{dE}{dx} \tag{22}$$

given in Reference 31, where $\Delta X/\epsilon = 0.0225$, is an empirically determined constant, and dE/dx is the collision electron stopping power. Stopping powers for $E_i > 10$ keV were taken from Reference 32, while those for $E_i \leq 10$ keV were taken from Reference 33. Calculated values for δ based on Equation 22 are shown in Table 4. Two facts can be seen from Figure 14. First, the I_t vs E_i data is relatively independent of the

polymer sample as expected since it is the gold electrode which determines absorption and back emission rather than the polymer. Second, for energies of 10 keV and above, I_t is reasonably close to values given by Equation 20. At $E < 10$ keV, agreement is poorer. There are several possible reasons for the discrepancy:

1. Uncertainty in the values for δ vs E.

2. Experimental error in our determination of I_B, I_i.

3. Experimental error in the determinations of τ by the authors of Reference 26.

4. Absorbtion of incident electrons in the gold front electrode not specifically accounted for.

Also included are two points based on a SANDYL Monte Carlo code transport calculation for 10 and 15 keV electrons incident on a gold electroded Kapton sample. The calculation predicts somewhat higher transmission values than those determined by Cosslett and Thomas. Thus, in the work that follows, I_t is calculated using

$$I_t = I_0 + I_i \delta = I_1 + I_2 + I_i \simeq I_\tau \qquad , \qquad (23)$$

with δ determined from Equation 22, and I_1 and I_2 determined for large negative bias of the front electrode to ensure repulsion of all secondary electrons.

Table 4. Calculated Secondary Emission Coefficients for Gold

E(keV)	5	6	8	10	12	13.5	15	16	19	20
δ	0.325	0.292	0.238	0.195	0.169	0.165	0.152	0.147	0.131	0.126

E(keV)	22	24	25
δ	0.119	0.112	0.109

A second issue to be addressed was to determine the average charge and dose deposited in the samples. It is reasonable to assume that as long as internal potentials are low relative to the beam energy, the injected charge and dose profiles are relatively independent of previously deposited trapped charge, at least in the short circuit configuration. However, under the internal influence of internal potentials and radiation-induced conductivity, the space charge distribution will evolve with time from its deposition profile (Refs 34,35). This will be discussed in more detail in Section 5.

However, the data presented there and in Reference 35 indicates that the charge distribution reaches a quasi-equilibrium distribution which changes slowly over the time period of the experiment (ca. one to two hours).

In performing the calculations for deposited dose we have employed Equations 5 and 11 after allowing for beam attenuation and energy dispersion in passing through the front gold electrode. The injected current I_t was determined experimentally using the data shown in Figure 14. The practical range R_p was computed using the relationship

$$R_p (gm/cm^2) = AE_i \left[1 - B/(1 + CE_i) \right] \tag{24}$$

derived in Reference 36 where $A = 5.37 \cdot 10^{-4}$ g·cm^{-2}·keV^{-1}, E_i is in keV, $B = 0.9815$ and $C = 3.123 \cdot 10^{-3}$ keV^{-1}. The mean energy loss or equivalently, the mean residual energy $\overline{E}_t$ for a beam with initial energy E_i traversing a foil of thickness t is taken to be $\overline{E}_t(R_p,t) = E_i(R_p - t)$ with $\overline{E}_t$ derived by inverting Equation 24. Thus, the dose in rads deposited in the sample was taken to be

$$D = \frac{0.1 \, J_t \overline{E}_t}{(R_p - t)} \quad , \tag{25}$$

with J_t in na/cm^2, $t = 6.76 \cdot 10^{-5}$ g/cm^2, the thickness of the gold electrode, and $\overline{E}_t$ in kV.

For comparison, several SANDYL Monte Carlo transport calculations were run to obtain accurate charge and dose deposition profiles. Figures 15 and 16 show the result of two of these calculations for 15 keV electrons incident on Kapton. In each case, the appropriate profile is shown with and without the 350 Å gold electrode. Shown in the figures are the practical (R_p) and mean ranges $\overline{R}$ for the two cases. The subscript u denotes the unelectroded sample, while that with subscript ϵ is that for the sample with the gold electrode.

Table 5 summarizes the depth/dose calculations for Kapton. For a series of incident electron energies (E_i) are tabulated the mean and practical ranges ($\overline{R}_s$ and R_{ps}, respectively) determined by SANDYL calculations, the corresponding quantities determined with Equation 24 and the procedure for calculating energy loss described in Reference 36 to determine $\overline{E}_t$. The mean dose D_s for the SANDYL calculation was calculated by taking the average dose deposited per transmitted electron/cm^2 out to R_{ps}. The average dose deposited using the Kobitch-Katz formulae $\overline{D}_{kk}$ was also
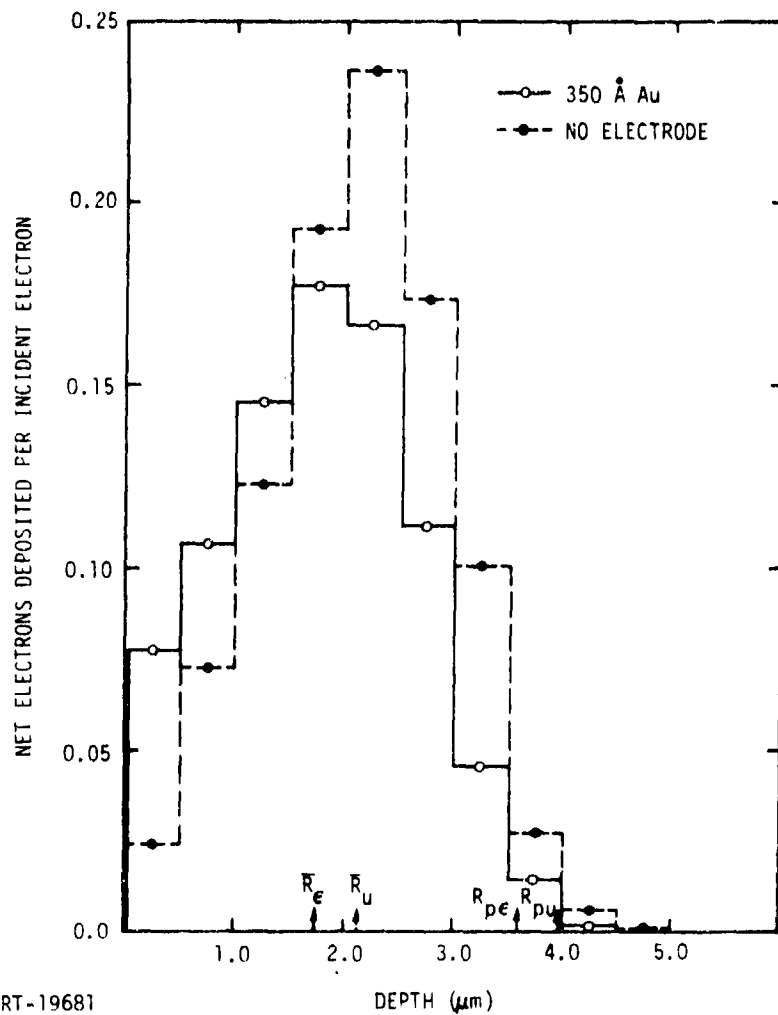
41

Figure 15. SANDYL charge deposition calculation for Kapton, $E_i = 15$ keV

calculated per transmitted electron/cm^2. For the foil thickness here, none of the incident electrons are stopped in the foil as calculated by either method. The average dose deposited by the SANDYL calculations take into account that a fraction of the beam is backscattered. Therefore, we have also included $\tau\overline{D}_{kk}$, where τ is the empirically determined transmission factor for Kapton. Where a value at a given energy was not determined it was calculated by interpolation. For the unelectroded samples, a backscatter coefficient was calculated using Equation 21. It can be seen from the Table 5 that the average dose per incident electron as calculated by Equation 25 agrees to within better than 10 percent of that calculated by SANDYL. The calculated practical ranges are about 10 percent lower in the unelectroded case and about 20 percent lower where electrodes are present than those calculated with SANDYL.

42
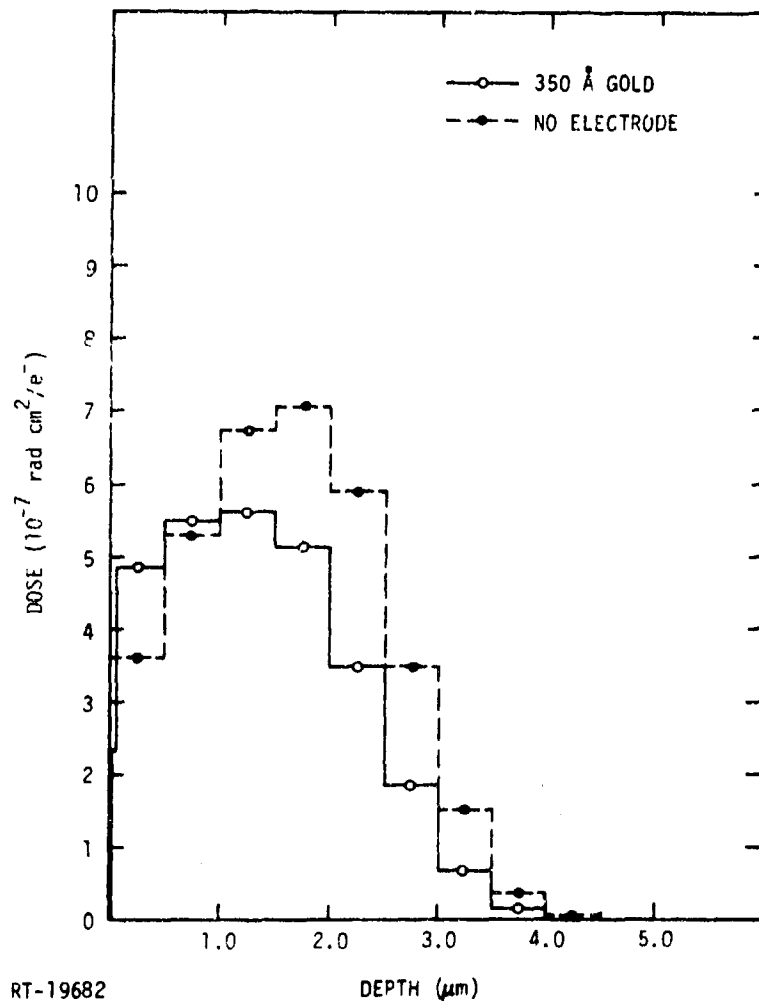
Figure 16. SANDYL dose deposition calculation for Kapton, $E_i = 15$ keV

4.3 CHARGE PENETRATION DEPTH IN TEFLON FEP, MYLAR S AND KAPTON

Charge deposition depth measurements were made at $300^{\circ}K$ as a function of incident beam energy for 1 mil samples of Teflon FEP, Mylar S and Kapton. These measurements were made by the charge induction method discussed in References 24 and 35.

The trapped charge $Q_t \simeq I_t t$ is deposited in the sample in a time t with a mean depth of deposition $\overline{R}$ given by Equation 10. After an irradiation time of about 10 seconds, the switch, S_1, in the circuit shown in Figure 17 is closed, shorting capacitor C_3. With σ given by Equation 9, the front and rear fields E_A and E_B must satisfy the relationships

43

Table 5. Summary of Depth/Dose Calculations for Kapton

E_i (keV)	R_{ps} (μm)	R_p (μm)	$\bar{R}_s$ (μm)	$\bar{D}_s$ 10^{-7} rad· cm^2/e^-	$\bar{D}_{kk}$ 10^{-7} rad· cm^2/e^-	$\bar{E}_t$ (keV)	$\tau \bar{D}_{kk}$ 10^{-7} rad cm^2/e^-
5_u		0.63			8.9		8.3
5_ϵ	2.1	0.16			12.4	1.75	1.2
10_u	2.1	1.81	1.04	5.91	6.2		5.8
10_ϵ	1.9	1.4	0.81	4.41	6.9	8.3	4.4
15_u	3.9	3.6	2.11	4.43	4.8		4.5
15_ϵ	3.6	3.1	1.75	3.40	5.0	13.8	3.3
20_u		5.8		3.91	3.9		3.7
20_ϵ		5.3			4.1	19.2	3.0
25_u		8.5			3.3		3.1
25_ϵ		7.9			3.4	24.1	2.7
27_u	10.6	9.6	6.4	3.21	3.1		2.9
27_ϵ		9.1			3.2	26.3	2.6

1. The subscript u denotes unelectroded sample.

2. The subscript ϵ denotes a sample with a 350 Å thick gold front electrode.

$$E_A = -(\sigma/\epsilon)(1 - \bar{R}/T_s) \qquad (26)$$

and

$$E_B = (\sigma/\epsilon)(\bar{R}/T_s) \quad , \qquad (27)$$

where ϵ is the dielectric permittivity.

Measurement of the charges Q_1 and Q_2 on capacitors 1 and 2 after irradiation yields the mean depth of charge deposition

$$\bar{R}/T_s = E_B/(E_B - E_A) = Q_2/(Q_1 + Q_2) \quad . \qquad (28)$$

In general, the value so determined will depend on the amount of charge injected, the time between cessation of charging and closing of S_1, and the injected current density, all of which determine the internal dynamics of conduction and space charge transport (Ref 35).

The circuit for these measurements and an example of the data obtained for a 10 keV charge depth measurement in 1 mil Teflon FEP is shown in Figure 17.
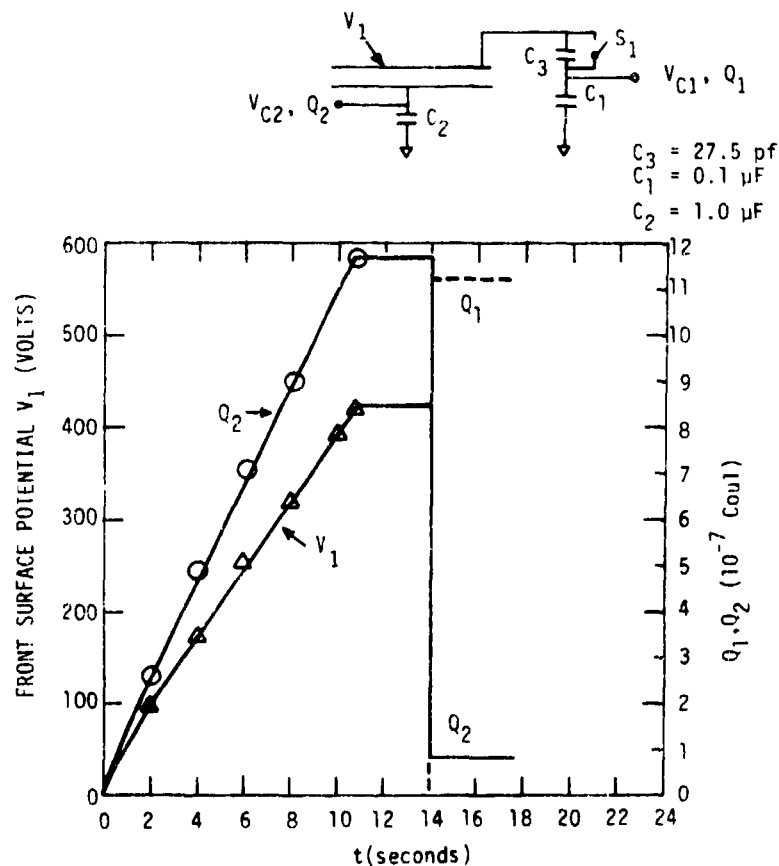
Figure 17. Typical charge depth measurement data. 25 μm Teflon FEP, 10 keV.

During charge injection from 0 to 10.8 seconds, the sample was in open circuit (S_1 open) and the total injected charge ($Q_2 = V_{C2}C_2$) and the front surface potential V_1 were measured versus time. During irradiation the front surface potential rose to 420 volts and the total injected charge, Q_2, was $\sim 1.16 \times 10^{-6}$ C. After 10.8 seconds, the electron beam remained off for the remainder of the measurement. At 14 seconds, switch S_1 was closed and the charge depth was determined by the charge induced on capacitors C_1 and C_2 using Equation 28. For this particular measurement

$$\overline{R} = \frac{0.8 \times 10^{-7}}{1.17 \times 10^{-6} + 0.8 \times 10^{-7}} \times 25.4 \ \mu m$$

$$= 1.63 \ \mu m \quad .$$

45

Figures 18 and 19 contain plots of the mean electron range as a function of incident electron energy for Teflon, Mylar S, and Kapton, respectively. Only one curve is given for the latter two polymers because the measured ranges are nearly identical. This is to be expected as the composition (relative atomic fractions) for the two polymers and their densities are similar. The data are plotted in terms of gm/cm^2 measured from the front face of the front gold electrode. To convert the experimental data to a mean range the following formulae was employed

$$R_i(gm/cm^2) = \overline{R}d + 6.7 \times 10^{-5} \quad , \tag{29}$$

Figure 18. Mean charge range measured from the front surface of the front electrode versus incident electron energy for Teflon. The letters kk denote ranges derived with the Kobitch-Katz relationship, Equation 24.

where $\overline{R}$ is the mean depth or centroid of the charge distribution in cm, R_i is the mean range measured from the front face of the sample computed under various approximations as shown in Figures 18 and 19, measured in g/cm^2, and 6.7×10^{-5} g/cm^2 is the thickness of the 350 Å gold electrode, and d polymer density in gm^3/cm^3.
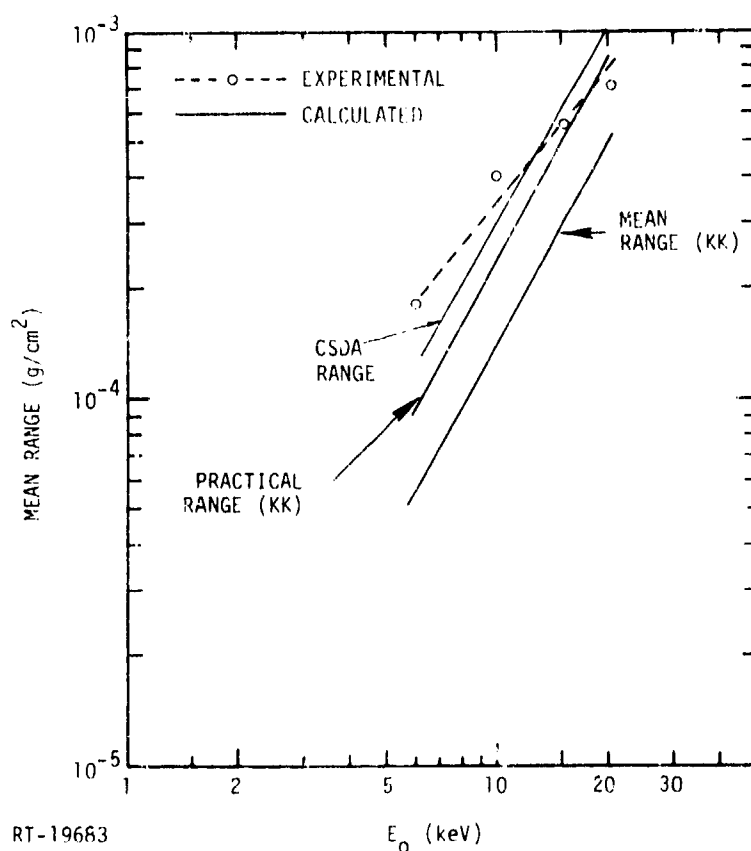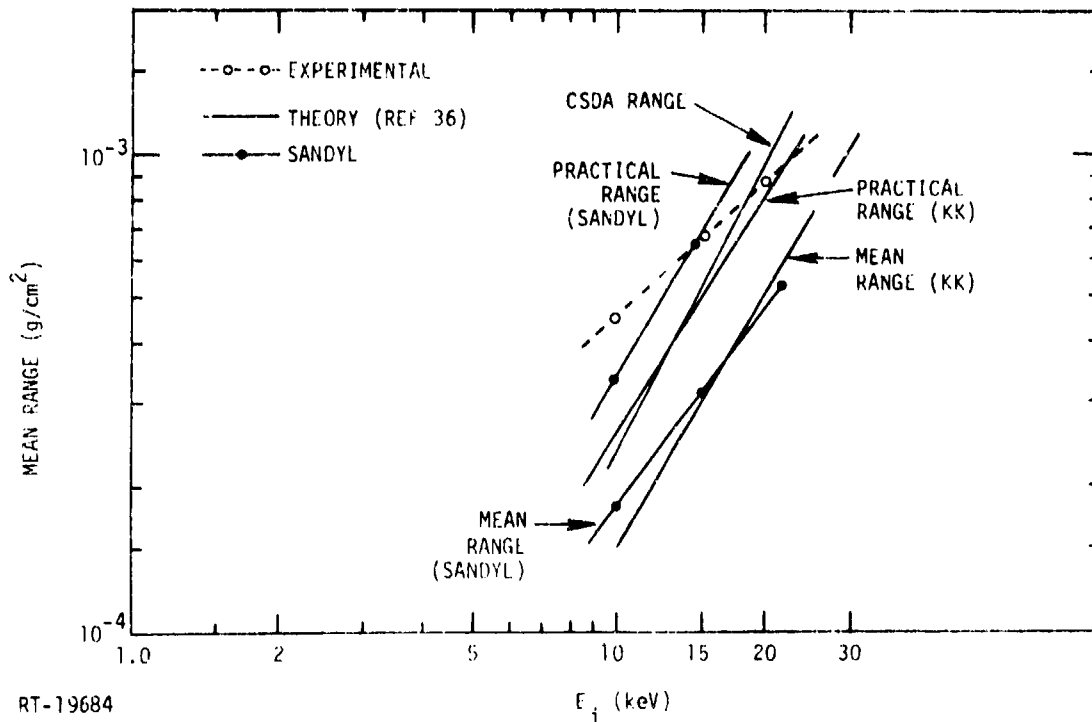
46

Figure 19. Mean charge range measured from the front surface of the front electrode versus incident electron energy for Kapton and Mylar

The data was plotted in the form given for comparison to theoretical values based on Equation 24. This procedure was employed because only a very limited set of SANDYL data was available. Examination of Table 5 shows that the values of R_p calculated by the Kobitch and Katz formula are about 20 percent lower than those calculated with SANDYL. The limited data available also indicates that $\overline{R}_S \simeq 0.6\,R_{PKK}$. The constant of proportionality is similar to that reported elsewhere (Ref 25).

It can be seen that the measured $\overline{R}/T_s$ values for all samples lie above the $\overline{R}$ calculated both from Equation 24 and for the SANDYL calculations, and for the most part above R_p obtained by either method. The authors of Reference 35 point out that as irradiation progresses, the initial deposited charge profile changes, primarily as space charge drifts into the unirradiated region of the sample. This is because the practical and CSDA ranges extend past the average range. We have also plotted the CSDA ranges for these materials. A region of radiation-induced conductivity extends past the centroid through the irradiated region. This conductivity allows charge transport to take place. Therefore during irradiation in open circuit, the centroid moves further into the unirradiated region following the field (in open circuit, region A

has zero net electric field). The time constant for this movement is of the order of ϵ/g_D which depends on depth. For the beam fluxes and dose rates employed, $g_D \sim 10^{-14} \; (\Omega\,cm)^{-1}$ and $\epsilon/g_D \sim 20$ seconds.

Similar range energy measurements were attempted on a 140 µm fused SiO_2 sample. The sample was mounted in a holder like that shown in Figure 9, which was designed to suppress secondary electrons. The sample was covered with a 214 Å thick aluminum front electrode. As this electrode is only 5.8 µg/cm^2 thick, even a 5 keV beam suffers negligible attenuation in passing through it. Irradiations were conducted with $J_i = 3.0$ na/cm^2 in open circuit, as shown in Figure 17, for 19 seconds before S_1 was closed. The mean deposited range was determined with Equation 28. The values for $\overline{R}/T_s$ were determined for $E_i = 10$ keV and $E_i = 23$ keV. The results were:

E_i (keV)	$\overline{R}/T_s$ (measured)	$\overline{R}/T_s$ (calculated)
10	4.8×10^{-3}	4.8×10^{-3}
23	4.8×10^{-3}	3.2×10^{-2}

$\overline{R}/T_s$ (calculated) was determined by taking $0.6 \times R_p$, where R_p was calculated with Equation 24. The agreement for 10 keV is probably fortuitous. In all probability the method is not sensitive enough to yield meaningful data for thick samples ($R_p/T_s \ll 1$).

4.4 CONDUCTIVITY MEASUREMENTS

This section describes the measurements to obtain values for the conductivity of the samples examined. Typically, the total conductivity is written

$$g = g_0(E,T) + g_D + \mu\rho \qquad (30)$$

where g_0 is the dark conductivity given by Equation 13, g_D the radiation-induced conductivity fit to Equation 5 and $\mu\rho$ is the effective space-charge conductivity. In an inhomogeneous insulator such as the polymers, which contain a complicated distribution of trapping and recombination centers, it is not always possible to separate the conductivity into terms such as is done in Equation 30. The validity of Equation 30 is discussed in Reference 21. In general, it requires that the electron-hole pair density exceed that of the space charge. The trap modulated mobility μ may be a function of

electric field and/or dose rate (Ref 24). The mobility will depend both on the charge carrier (electrons or holes), and if different trapping levels are present, μ is generally not a single term (Ref 37). Moreover, μ in the irradiated and unirradiated regions are different. However, it is often the case that at a given temperature, only one level for one charge carrier predominates. In the work performed here it is assumed that this is true and that the space-charge-limited current could be described with a single mobility term. Generally, each term is measured separately by creating experimental conditions where it predominates. In this section, measurements of g_0 and g_D are presented. Measurements of μ are discussed in Section 5 of the report.

4.4.1 Dark Conductivity

The dark conductivity of the various samples was measured as a function of bias and in some cases temperature. It was measured using the circuit configuration of Figure 11a by monitoring I_1 and I_2 as a function of applied bias. The value of conductivity for these insulators is somewhat ambiguous because of the relatively large transient absorbtion currents which flow following a step voltage excitation (Ref 38). The detailed form of the absorbtion current depends on the type of carrier injection process which occurs at electrode-insulator interfaces and on trapping processes. The apparent conductivity will decrease by one or more orders of magnitude in a few minutes after imposition of an applied voltage across the sample as shown in Figure 20 which is a plot of the resistivity of a 1 mil Mylar S sample for 306 V bias (120 kV/cm) as a function of time.

Measured values for effective dark conductivity as a function of applied bias, temperature, and time are shown in Table 6. Several facts are evident. In times ~one minute, the measured dark conductivities are and remain $<10^{-17}$ $(\Omega \text{cm})^{-1}$. There is little field dependence in evidence, the conductivity values for 120 V, are within experimental error, equal to those for 306 V. For 6.25 μm, Mylar, these voltages correspond to fields of 192 kV/cm and 490 kV/cm, respectively. The data in Figure 20 show that even after four minutes, the apparent conductivity is still decreasing. The equilibrium values of dark conductivity for a given applied voltage and temperature are all $<10^{-18}$ $(\Omega \text{cm})^{-1}$. The measured values of radiation conductivity are typically $>10^{-15}$ $(\Omega \text{cm})^{-1}$ for the relevant dose rates (cf. 4.4.2). Hence the neglect of g_0 in computing g_D is justified.

The Adamec-Calderwood theory (Ref 29), as embodied in Equation 13 predicts that the conductivity of the 6.25 μm Mylar sample at 306 V should be 7.3 times that at

120 V. The conductivity of Kapton should show a similar increase. In neither case is the predicted field enhanced conductivity observed. However, Equation 7 describes the steady-state conductivity; i.e., that which controls current flow after the absorbtion currents have ceased and the distribution of charge carriers in the conduction band, in traps and in recombination centers reach thermal equilibrium. No data was taken at long times when the current reach their equilibrium values because it is clear that $g_0 \ll g_D$ for irradiation times of interest.

Table 6. Dark Conductivity Values

Sample	Thickness (μm)	T (°K)	V_1 (volts)	Measured Conductivity ($10^{-18}\Omega^{-1}cm^{-1}$)			
				1 min	3 min	10 min	30 min
Mylar	6.25	300	+120	6.4	2.4		
			+213	5.6	2.2		
			+306	5.0	2.2		
			+306[a]	6.7		1.4	0.63
		200	+120	8.8	2.7		
			+213				
			+306	9.6	2.5		
			+306[a]	3.9	1.7	0.6	0.28
		185	+120	1.3	3.8		
			+213	13	3.5		
			+306	13	3.4		
	25.4	300	+306	5.6	2.0	0.74	0.14
Teflon	25.4	300	-100	0.14	0.077		
			-300	0.11	0.040		
			-500	0.11	0.040		
Kapton	7.6	300	-120	6.5	2.3		
			-213	6.8	2.4		
			-306	7.0	2.5	1.0	0.56
		119	-306	3.4	1.3	0.34	0.23

[a]Repeat measurements.

4.4.2 Radiation-Induced Conductivity

The radiation-induced conductivity induced in the three polymers and in fused quartz by the electron beam was measured in two ways. For the 6.25 μm Mylar and 7.62 μm Kapton samples, g_D was determined by exposing these films to penetrating electron beams; i.e., those of sufficient energy so that the practical range exceeded the
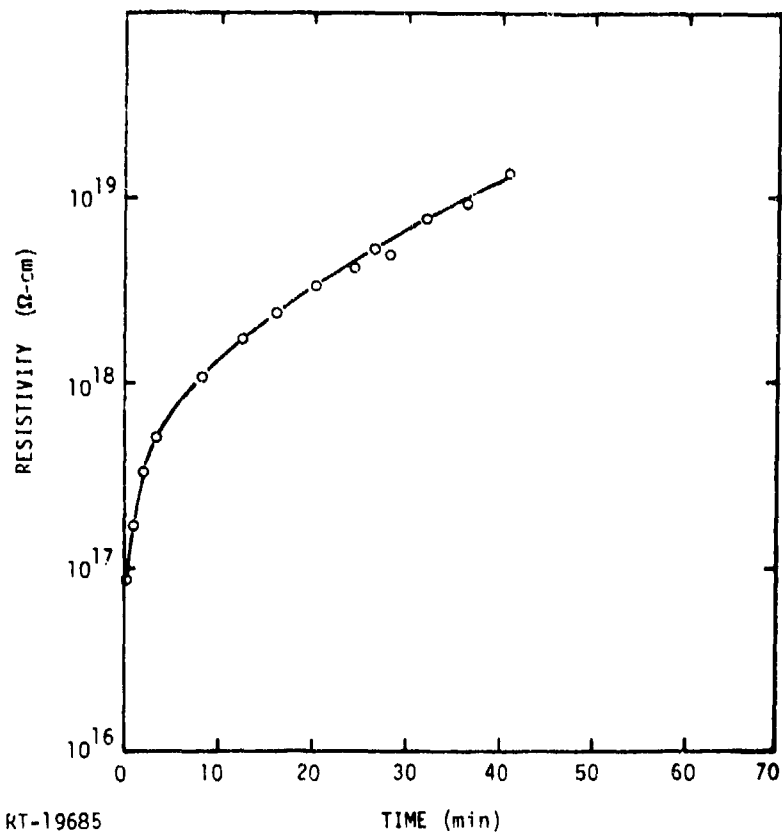
Figure 20. Resistivity versus time after applying 300 V bias 300°K for 25 μm type S Mylar

sample thickness. In this case, it is assumed that the conductivity is uniformly enhanced throughout the entire volume of the dielectric and given by

$$\Delta g = g_D = \frac{(\Delta J_2)T_s}{V_1} \tag{31}$$

where J_2 is the current density flowing out the rear electrode and V_1 is the applied bias for sample irradition in the "short circuit" configuration. The assumption of uniform conductivity enhancement follows from the assumption that the deposited dose is uniform in the dielectric and that g_D is given by Equation 12.

Where the sample is too thick for the maximum energy electron beam to penetrate the sample, a second method described in Reference 24 was employed. The experimental configuration is that of Figure 11a. Typically, the sample was irradiated with the switch open for about 10 seconds. Neglecting charge leakage to the rear

51

electrode, the deposited charge Q_t is $I_t t$ after irradiation. The switch is then closed. It can be shown that the trapped charge density will decay exponentially to its short circuit equilibrium value, $I_t \tau_D$, where
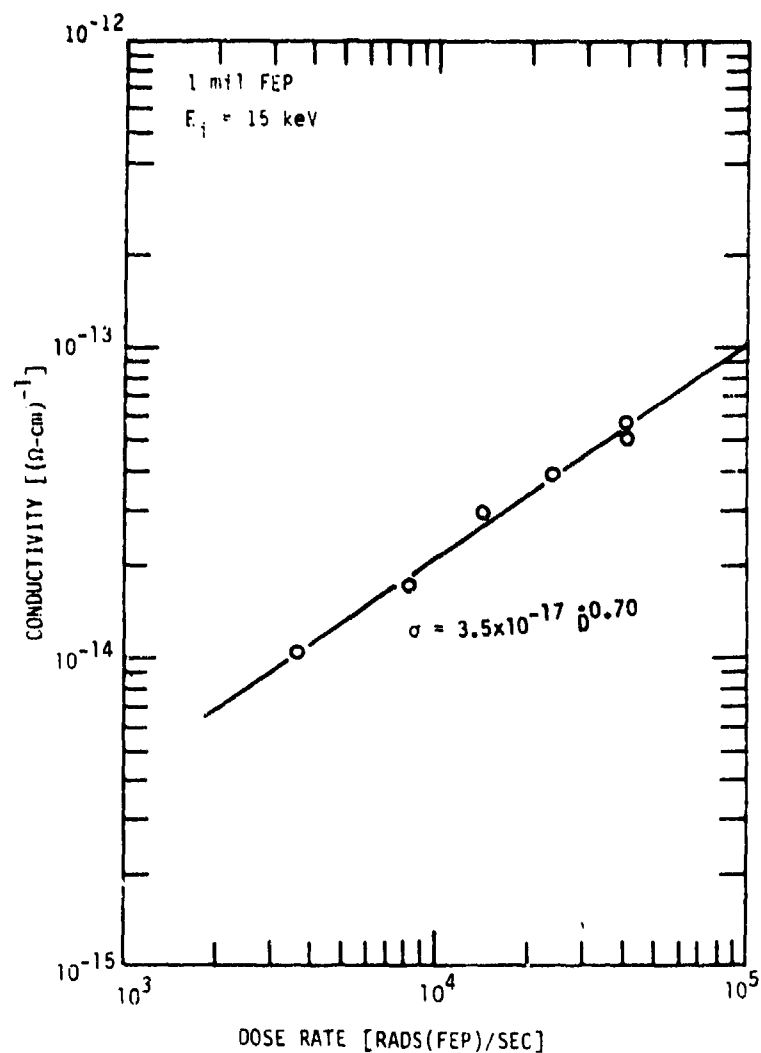
$$\tau_D = \frac{\epsilon \, T_s}{g_D(T_s - \overline{R})} \tag{32}$$

and τ_D is the e^{-1} time constant. In this model, $\overline{R}$ is the experimentally determined value for the charge centroid (cf. subsection 4.3). τ_D is about nine seconds for a 25.4 μm FEP sample irradiated with 15 keV electrons at a deposited dose rate $\dot{D} = 10^4$ rads(FEP)/s. The dose rate was calculated with Equation 25.

The radiation-induced conductivity for Teflon FEP as a function of dose rate is shown in Figure 21. The sample thickness was greater than the range of electrons of maximum energy output by the source (30 keV). Thus, only the nonpenetrating beam technique was used. For the measurements shown, incident beam energy was 15 keV. The normal dark conductivity of this material at 300°K is many orders of magnitude lower than the values measured (cf. subsection 4.4.1). The straight line is a least-squares fit of the data to Equation 12. It can be seen that the dose rate dependence is sublinear. The measured value of Δ is identical to that obtained by the authors of Reference 24, while the magnitudes observed are about a factor of six lower. However, the g values determined are within the range of reported values (Refs 18,39). A value for the exponent Δ such that $0.5 < \Delta < 1$ indicates that there is an exponential distribution of traps (Ref 27).

Figure 22 shows the radiation-induced conductivity in Kapton H as a function of dose rate in the polymer. Data is presented for the two techniques with the straight lines being a least-squares fit to the experimental data. The practical range of 27 keV electrons in Kapton was calculated to be 9.1 μm, while the sample thickness was 7.6 μm. Also plotted is the bias dependence of the conductivity data for the penetrating beam measurement. The conductivity in these cases was calculated from the slope of the I_2-V_1 curves for each dose rate and bias point. It can be seen that the values for conductivity obtained by the nonpenetrating beam technique falls within the range of values obtained by the more conventional method. The range of conductivities observed lies at the high end of values reported in Reference 18.

The radiation-induced conductivity in Mylar S as a function of dose rate is plotted in Figure 23. The data was derived from measurements with a nonpenetrating beam

52

$$\sigma = 3.5 \times 10^{-17} \, \dot{D}^{0.70}$$

1 mil FEP
$E_i = 15$ keV

CONDUCTIVITY $[(\Omega\text{-cm})^{-1}]$

DOSE RATE [RADS(FEP)/SEC]

RT-17277

Figure 21. Radiation induced conductivity in FEP Teflon as a function of dose rate

(open squares) and a penetrating beam (open circles). Again, the straight lines through the experimental data are a least-squares fit to Equation 12. It can be seen that the conductivity coefficients determined by the two procedures agree to within a factor of two, while the dependence of conductivity on dose rate is essentially identical. The measured values for the radiation conductivity fall at the upper end of reported data (Ref 18). The measured values of K_D are greater than those reported in the literature; however, there is no information on the value of Δ given in that reference. To yield a conductivity of 10^{-14} $(\Omega\,\text{cm})^{-1}$ at 10^4 rads(Mylar)/s requires a $K_D = 10^{-18}$ if $\Delta = 1$.

KAPTON H

O τ METHOD (25μm, 15 keV)
   PENETRATING (7.6μm, 27 keV)
▽ -120V BIAS

△ -213V BIAS

□ -368V BIAS

$\sigma = 3.8 \times 10^{-17} \dot{D}^{0.90}$

$\sigma = 5.6 \times 10^{-17} \dot{D}^{0.85}$

$\sigma = 2.7 \times 10^{-17} \dot{D}^{0.90}$

$\sigma = 5.9 \times 10^{-18} \dot{D}^{1.00}$

CONDUCTIVITY $[(\Omega\text{-cm})^{-1}]$

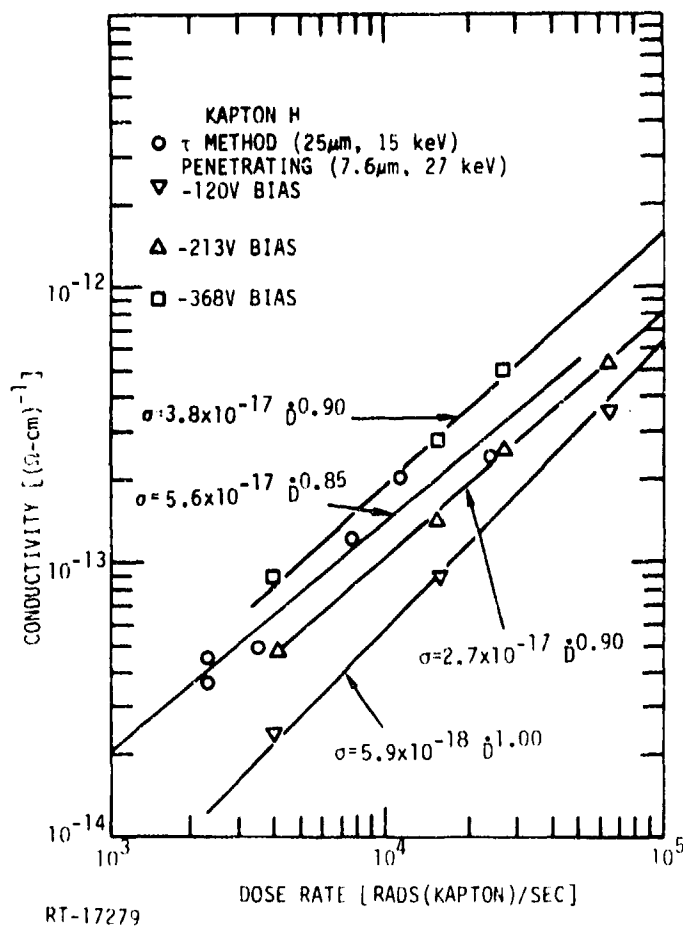DOSE RATE [RADS(KAPTON)/SEC]

RT-17279

Figure 22. Radiation-induced conductivity in Kapton H as a function of dose rate and applied bias

The radiation-induced conductivity was measured in the 0.25 mil Mylar S sample excited by an electron beam whose energy is 24 keV where $R_p/T_s \simeq 1.07$. Measurements were made as a function of dose rate and negative front surface bias. Figure 24 shows the current leaving the rear electrode I_2 as a function of bias and dose rate. the values for the conductivity plotted in Figure 23 were determined from the average values of $\Delta I_2/\Delta V_1$ taken from the I, V curves in Figure 24. It is evident that the slope $\Delta I_2/\Delta V_1$ versus V_1 is positive, indicating that the effective conductivity is increasing with bias. This bias-dependent increase in conductance with increasing applied voltage is also evident in the Kapton data shown in Figure 22.

To explain the bias dependence of the measured conductivity values, three possible explanations may be invoked. These are:

54

1. A field-induced enhancement of the conductivity through an increase in the number of charge carriers generated.

2. A field-induced enhancement of the mobility in the polymer because trap escapes are aided by the field (Poole-Frankel effect).

3. Increase in space-charge currents in the rear of the sample, where the real charge and dose deposition are less than those close to the front of the sample.

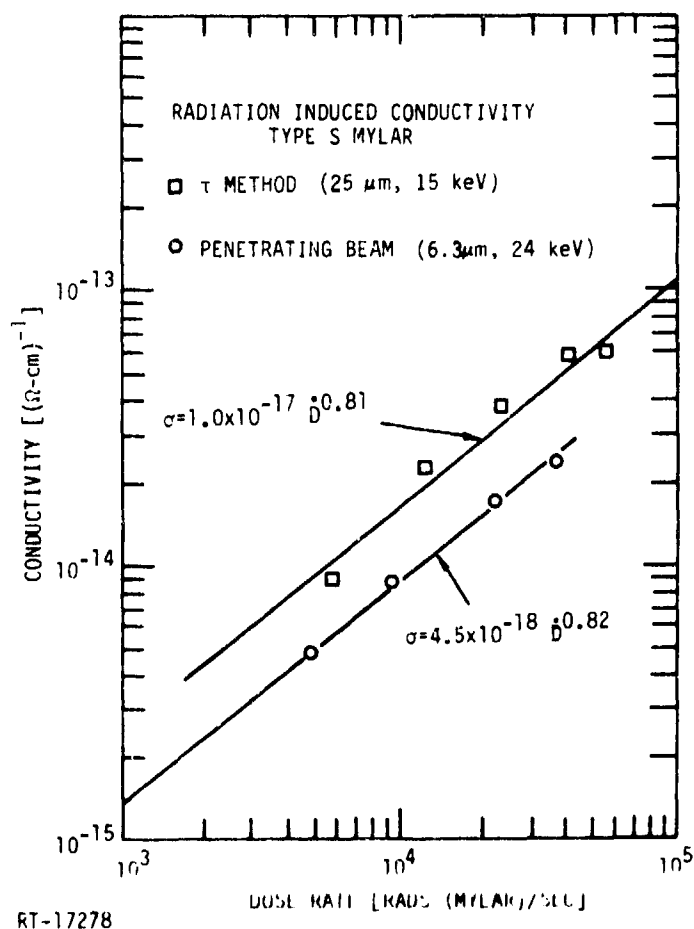We discuss each of these in turn.

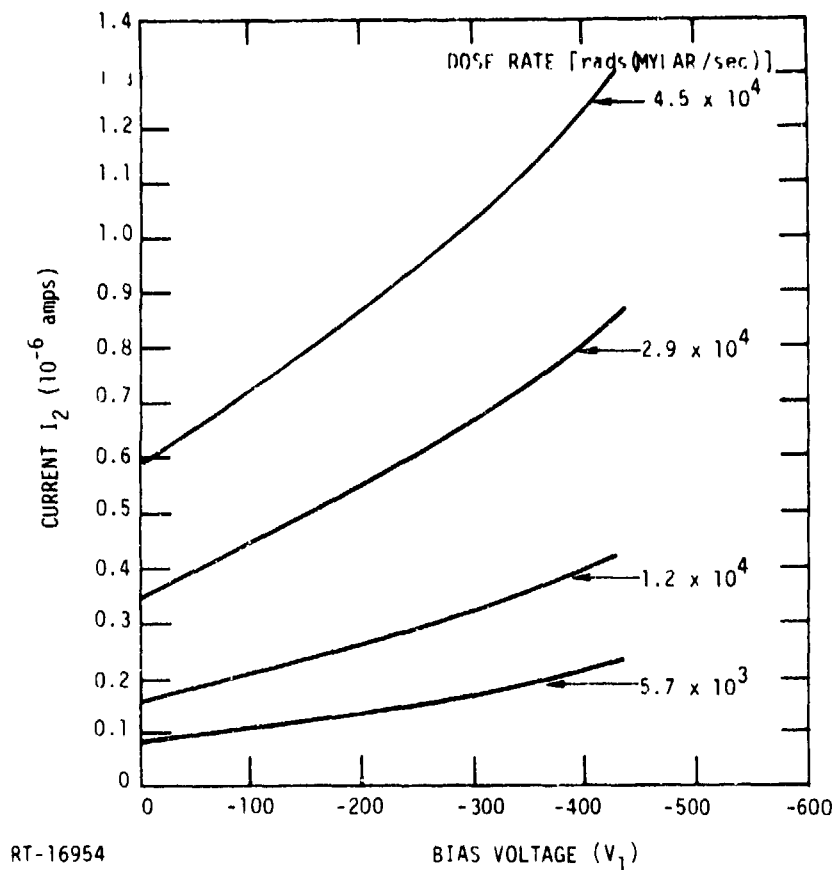Figure 23. Radiation-induced conductivity in Type S Mylar as a function of dose rate

55

Figure 24. Leakage current (I_2) versus dose rate and bias.
6.3 μm Mylar S, 24 keV, R/D = 1.07.

Hughes (Ref 40) has studied the charge transport of electrons in thin (2.5 μm) films of Mylar. He finds that the concentration of charge carriers per rad of absorbed dose increases by a factor of ca. 10 when the applied field is increased from <100 kV/cm to 500 kV/cm. He argues that geminate recombination of electron-hole pairs is diminished as the field is increased.

Field enhanced mobility is invoked by Adamec and Calderwood as a mechanism by which an applied electric field increases conductivity. The presence of a field increases the trap modulated mobility by increasing the escape rate of trapped charge carriers. However, both Adamec and Calderwood and Hughes agree that field enhancement of g_0 does not become significant until E > 500 kV/cm, or above the values for which our data was taken.

In performing the penetrating electron irradiations, it was assumed that because $R_p > T_s$, all of the incident charge passes through the sample, creating a uniform dose

profile. In fact, SANDYL calculations indicate that a significant fraction of the incident electron beam is deposited in each sample as $\overline{R} \simeq 0.6\ R_p < T_s$. A calculation for 24 keV electrons incident on Mylar indicate that approximately 50 percent of these would be trapped in the polymer. These electrons will move toward the rear electrode under the built-in space charge fields and also under the applied negative bias. At sufficiently high fields all of this charge is swept out of the samples and as expected, the value of the radiation-induced conductivity measured with a "penetrating" beam will approach that measured by the "τ" method. Space charge conduction in region B of the sample is discussed in Section 5.

4.4.3 Delayed Conductivity Measurements

Delayed conductivity measurements were made in 1 mil Mylar S and Teflon FEP samples. The measurement setup is that shown in Figure 11b. In performing the radiation conductivity measurement the sample was irradiated in open circuit for approximately 10 seconds or so after which the switch shorting C_3, the 27.5 pF air capacitor, is closed. The short circuiting induced a charge rearrangement from which the mean depth of charge deposited can be determined as discussed in subsection 4.3. However, current continues to flow through the sample which decreases with time. It can be shown (Ref 24) that the current flow or, equivalently, the change in charge on C_2 can be related to the post-irradiation conductivity $\overline{g}(t)$ in the irradiated portion of the sample through the equation

$$ I_2(t) = -\overline{g}(t)\ \frac{q_2}{\epsilon}\ \left(1 - \frac{\overline{R}}{T_s} \right) , \tag{33} $$

where q_2 is the charge per unit sample area on C_2.

Figures 25 through 28 show a plot of the charge stored on the rear electrode, q_2, internal fields E_A and E_B between the injected charge layer and front electrode or rear electrodes, respectively, and charge per unit area embedded in the sample q_t. Irradiation condictions were 10 seconds at 3.2×10^{-9} A/cm^2, 15 keV in both cases. Values for q_t and E_A are calculated from the measured values of q_2 and V_{C2}, the charge per unit area, and potential of the rear electrode referenced to ground using the relationships

$$q_t = \frac{T_s}{\bar{R}} q_2 \quad , \tag{34}$$

and

$$E_1 = \left(1 - \frac{T_s}{\bar{R}}\right) E_2 = \left(1 - \frac{T_s}{\bar{R}}\right) \frac{C_2 V_{C2}}{A} \quad , \tag{35}$$

where A is the area of the rear electrode $\cong 45 \text{ cm}^2$.

No attempt has been made to provide a detailed model of the observed delayed conductivity. One commonly held model (Ref 29) predicts that the persistent conductivity in the irradiated portion of the sample is given by
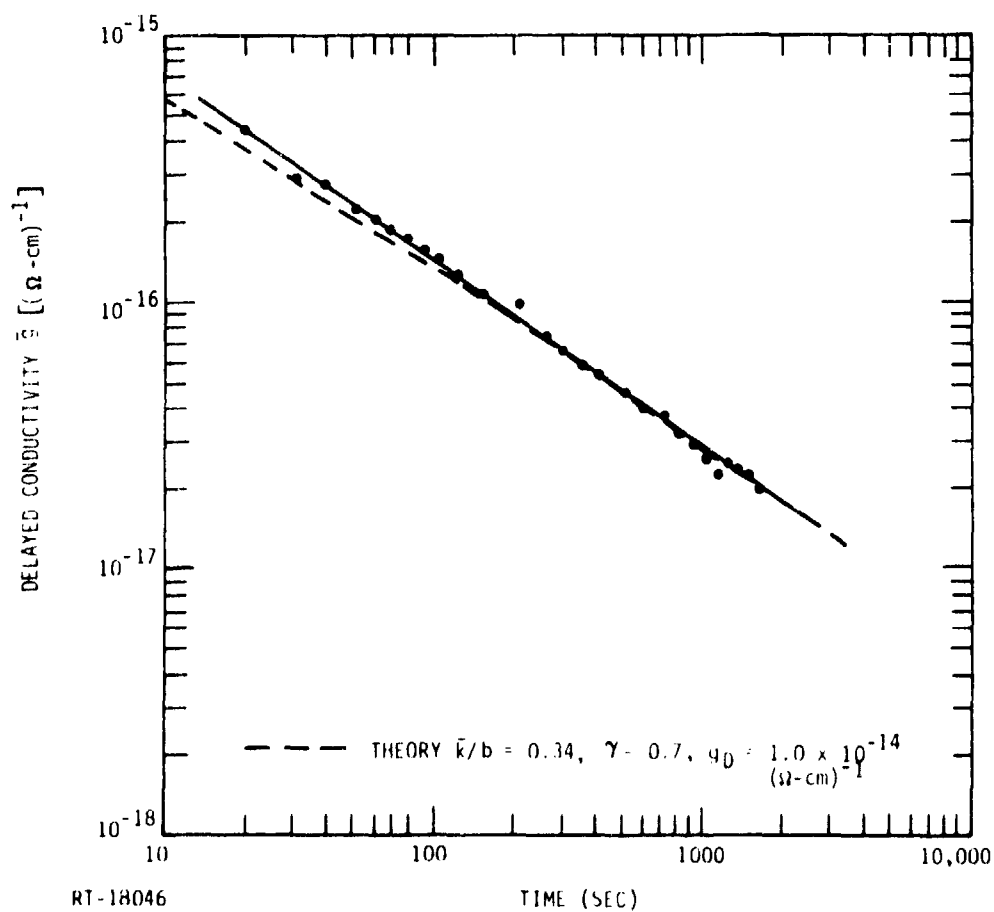

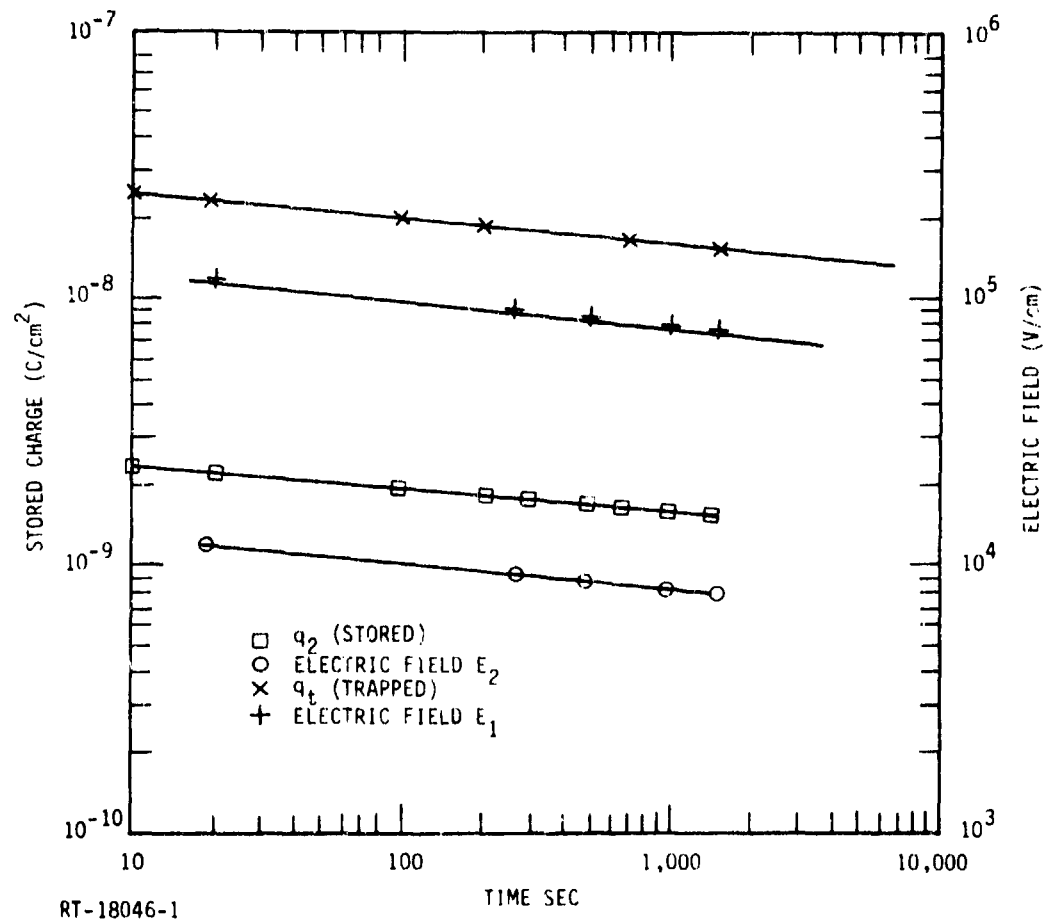Figure 25. Delayed conductivity after irradiation for FEP Teflon

RT-18046-1

Figure 26. Internal electric fields and stored charge after irradiation for FEP Teflon

$$\bar{g}(t) = \bar{k}g_D(1 + bt^\gamma)^{-1}$$

$$\simeq \frac{\bar{k}}{b} g_D t^{-\gamma}, \, bt \gg 1 \quad , \tag{36}$$

$\bar{k} \leqslant 1$ is a reduction factor which takes into account that thermal equilibrium between conduction electrons and trapped electrons is not instantly reached. For the conditions of irradiation, $g_D(FEP) = 1.05 \times 10^{-14} \, (\Omega \, cm)^{-1}$ and $g_D(Mylar) = 7.5 \times 10^{-15} \, (\Omega \, cm)^{-1}$. Also shown in Figures 25 and 26 are plots of Equation 36 with appropriate values of g_D and $k/b = 0.34$ and $\gamma = 0.7$ for FEP, and $k/b = 0.48$ and $n = 0.8$ for Mylar. The measured rate of decrease of delayed conductivity is slower than commonly predicted; i.e., $n = 1$ for bimolecular recombination. Note that the values of γ obtained are equal to the corresponding Δ values for radiation-induced conductivity.
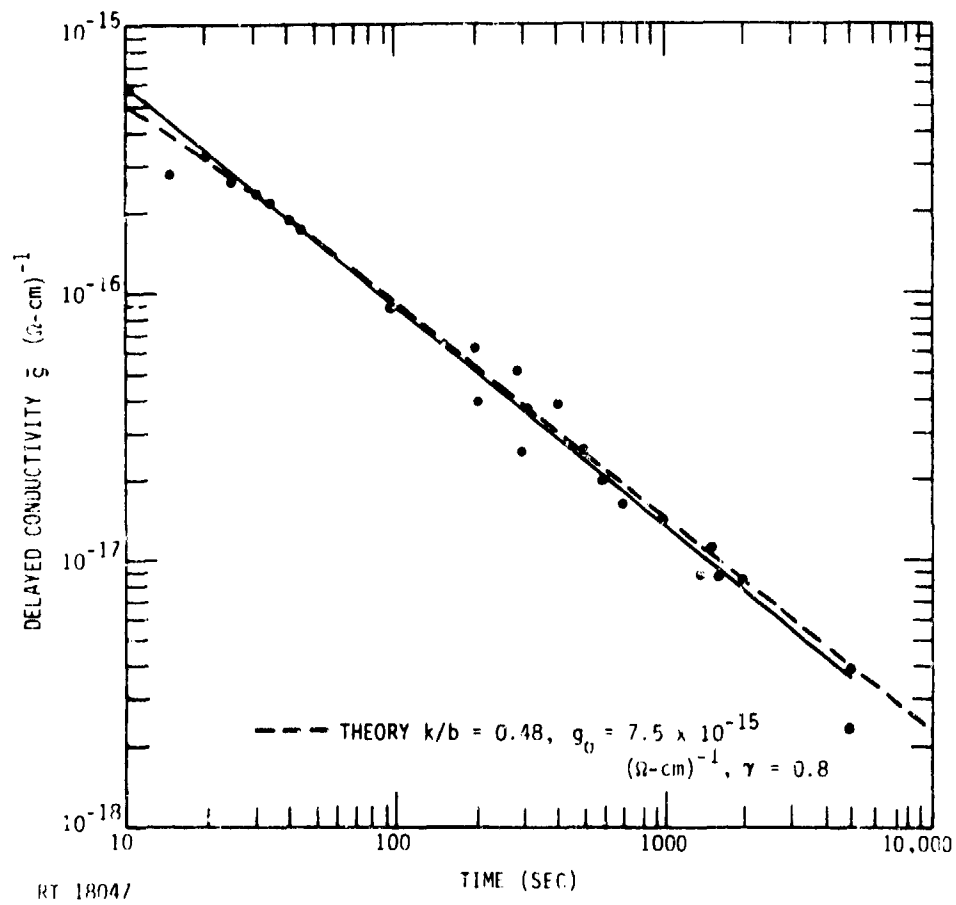
59

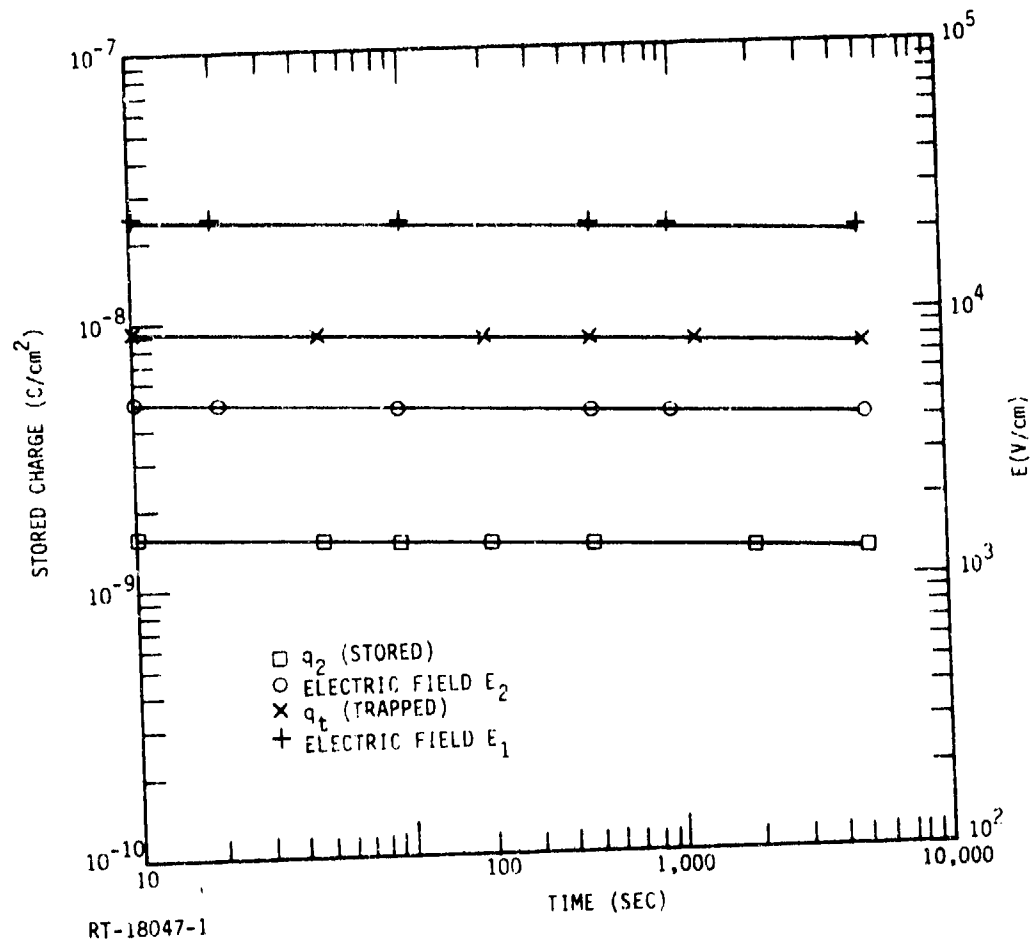Figure 27. Delayed conductivity after irradiation for Mylar S

RT 18047

Figure 28. Internal electric fields and stored charge after irradiation for Mylar S

RT-18047-1

61

5. LEAKAGE CURRENT MEASUREMENTS

5.1 EXPERIMENTAL RESULTS

A series of leakage current measurements were made in a set of FEP, Kapton, and Mylar polymer films and a fused silica (Corning 7940) solar cell coverslip. The parameters varied were sample thickness, sample temperature, beam energy, and applied bias to the front electrode. The experimental setup is the "short circuit" configuration pictured in Figure 11a. During the irradiations at a given temperature and beam energy, I_i, I_b, I_1, and I_2 were monitored. The data plotted in the figures that follow are quasi-equilibrium values, i.e., where I_1 and I_2 essentially ceased to change. Typically, this was 30 to 60 minutes after the start of irradiation. Measurements were run at fixed E_i, T, starting with the lowest value of applied bias (most negative) and increasing the bias in approximately 100 V increments. Most of the data was taken with $-520 \leqslant V_1 \leqslant +520$.

The incident beam current was monitored with a calibrated Faraday cup facing the source. The back-emitted beam current was monitored with a second Faraday cup facing the target. The net back-emitted current I_b was determined using the procedure described in subsection 4.2.

The measured electrode currents I_1 and I_2 were corrected for the secondary current leaving the front electrode which varied as a function of applied bias (cf. subsection 4.2). The net injection current I_t was determined for $V_1 \leqslant 0$ such that

$$I_t \simeq I_o - I_\beta + I_\delta = I_1 + I_2 + I_\delta \quad . \tag{37}$$

The secondary emission current I_δ was determined by computation with Equation 22. A check of the I_δ values so determined was made by comparing I_b for $V \leqslant 0$ and $V \geqslant 0$ which gave reasonable agreement. As the Faraday cup was not designed to measure the total emitted secondary emission current, it was felt more reliable to use Equation 22. The meter current I_1 was thus corrected for secondary emission by requiring

63

$$I'_1 + I_2 = I_t \qquad (38)$$

The current I'_1 represents that current reaching the front electrode from inside the sample which is the quantity needed to determine material parameters.

In the data which follows, we have plotted I'_1 and I_2 for different samples, incident electron energies, and in some cases sample thickness and temperature. Where $R/T_s \leqslant 1/2$, $I'_1 \simeq I_t$ at all values of V_1. Hence only I_2 was plotted.

To understand the data presented below, Figure 12 shows the sign conventions employed. Irradiation parameters for these measurements are summarized in Table 7 and the data is given in Figures 29 through 49.

Table 7. Summary of Irradiation Parameters for Charge Leakage Experiments

Material	Thickness (μm)	Temp. ($^\circ$K)	Beam Energy (keV)	$\lvert I_i \rvert^a$ (na)	$\lvert I_i - I_b \rvert^a$ (na)	$\lvert I_t \rvert^a$ (na)
FEP	25.4	300	5	155	29.0 (p)	21.4
			10	142	21.0	48.7
			15	152	68.0	91.0
			20	130	75	91.2
Kapton	25.4	300	6	123	27 (p)	1.0 (p)
			13.5	138	49.5	76.7
			20	138	81.7	93.2
	7.6	300	10	136	60.3	86.4
			15	134	67.0	87.3
			22	131	79.0	94.2
	7.6	110	19	125	79.0	95.1
		200	19	129	78.8	95.6
		300	19	132	84.7	101.7
Mylar	25.4	300	5	110	5.5	41.3
			10	110	33.0	54.4
			15	110	52.8	69.5
			20	110	63.8	77.7
	6.3	300	8	140	29	62.3
			12	141	56.4	80.2
			16	140	66	93.4
			20	140	87	98.8
			24	137.5	85.5	103.4
	6.3	127	16	124	75.1	93.3
		200		124	69.6	87.8
		250		127	73.9	91.6
		300		125	68.7	87.0
Fused Silica	140	300	10	6.71	5.90	5.90
			23	6.72	5.71	5.71

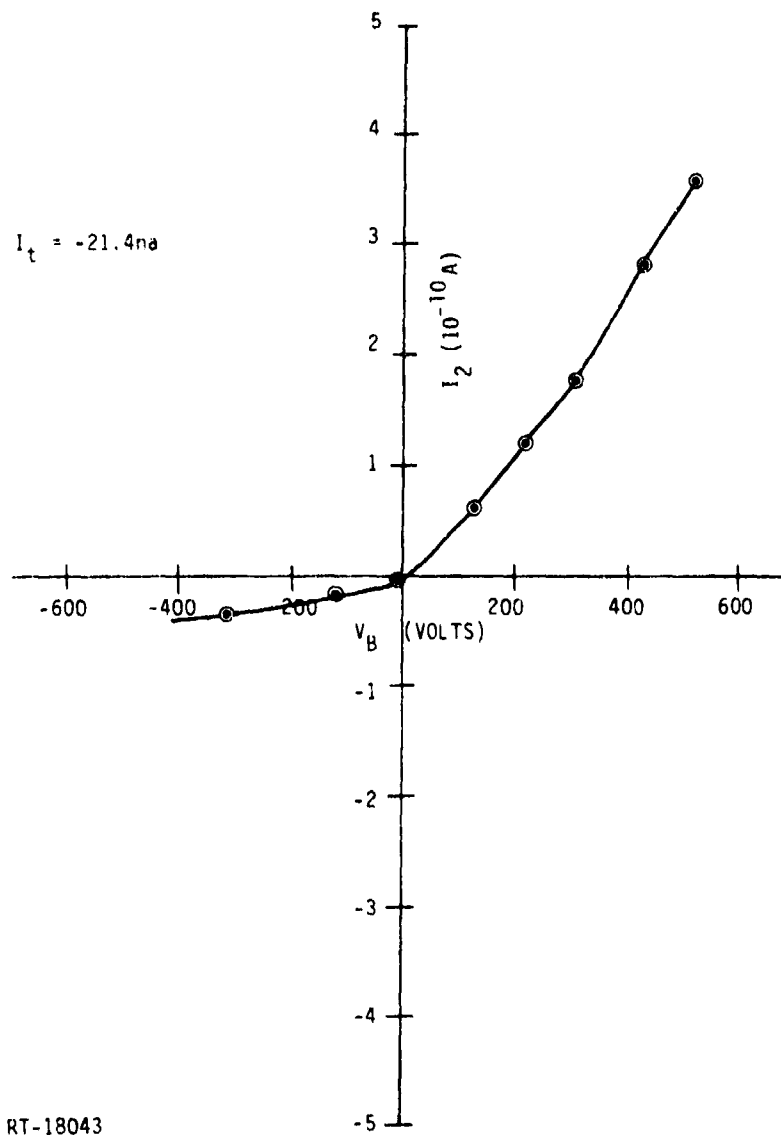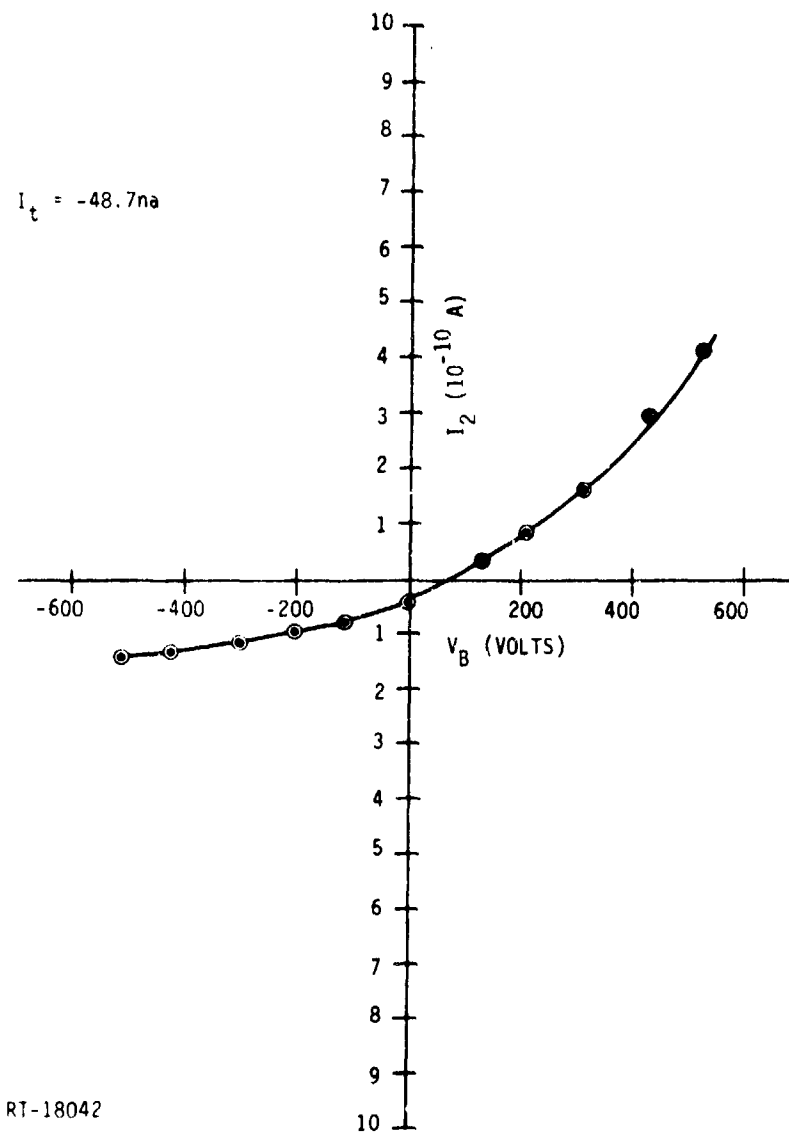[a]All values are negative by the sign convention of Figure 12 except those with a (p).

Figure 29. Leakage current through the rear electrode of a 25 μm FEP sample as a function of applied bias for $E_i = 5$ keV, T = 300°K

RT-18043

65

$I_t = -48.7$na

I_2 $(10^{-10}$ A)

V_B (VOLTS)

RT-18042

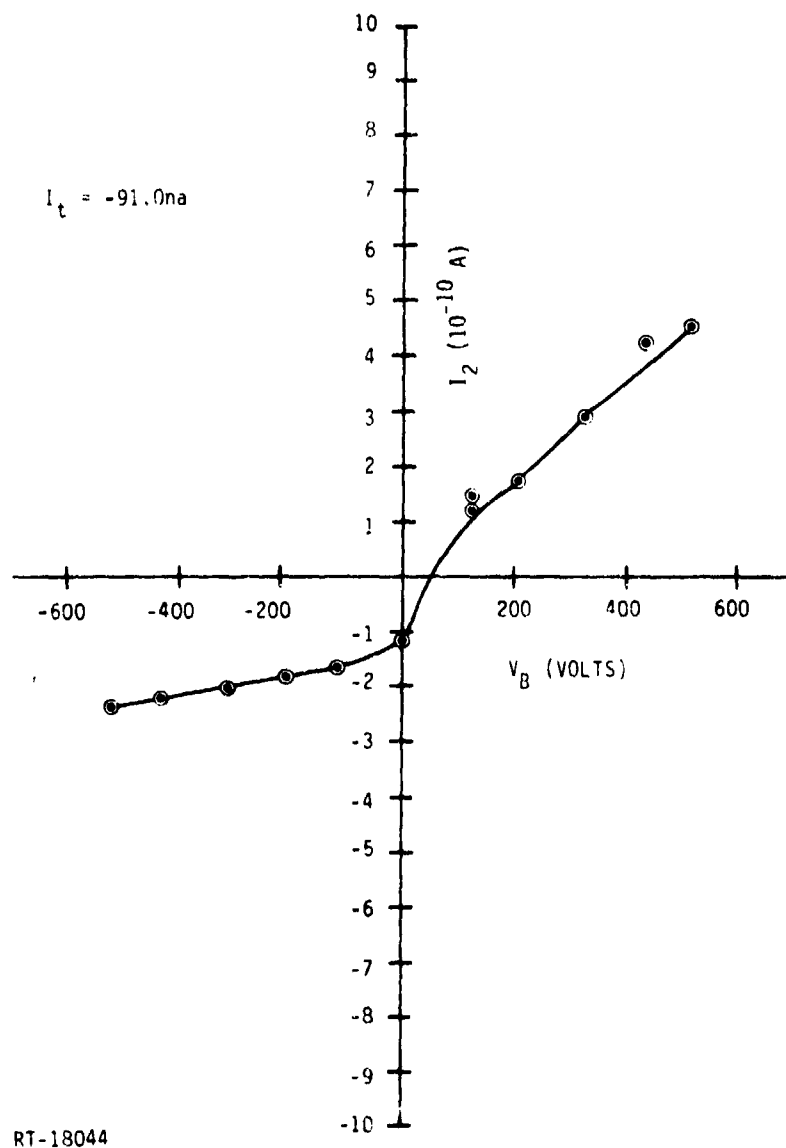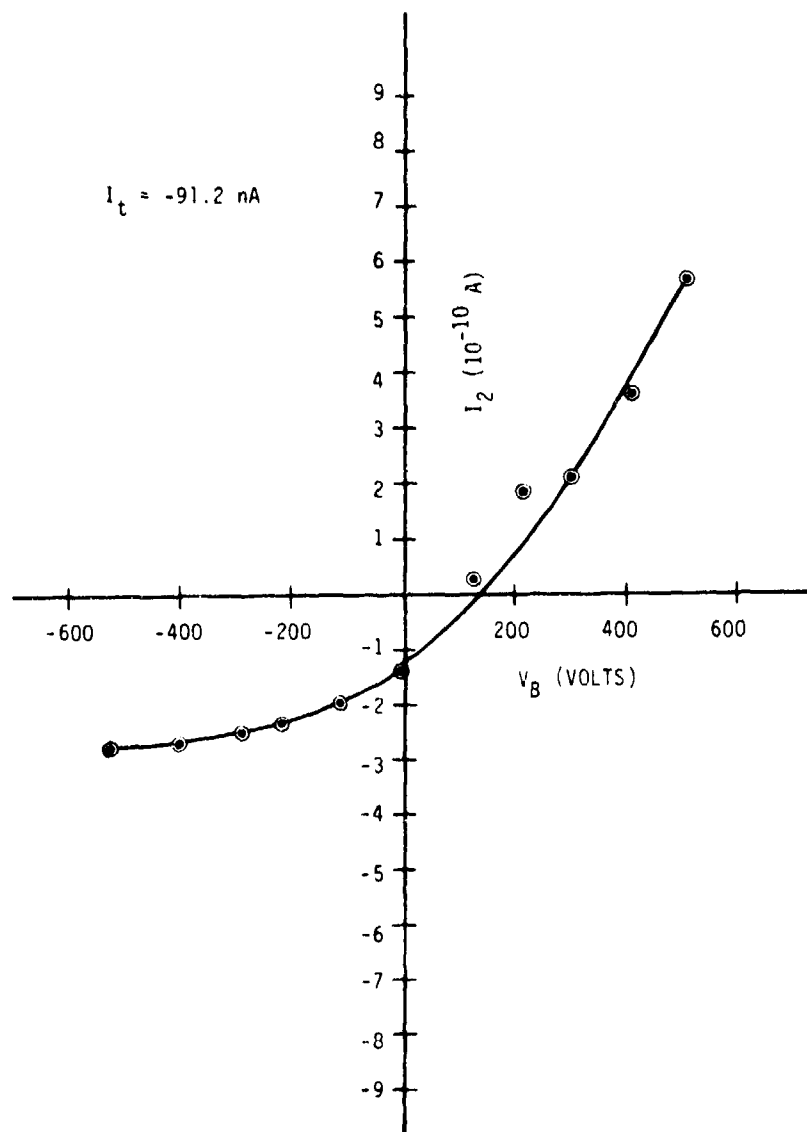Figure 30. Leakage current through the rear electrode of a 25 μm FEP sample as a function of applied bias for $E_i = 10$ keV, T = 300°K

Figure 31. Leakage current through the rear electrode of a 25 μm FEP sample as a function of applied bias for E_i = 15 keV, T = 300°K

$I_t = -91.2$ nA

I_2 (10^{-10} A)

V_B (VOLTS)

RT-18045

Figure 32. Leakage current through the rear electrode of a 25 μm FEP sample as a function of applied bias for $E_i = 20$ keV
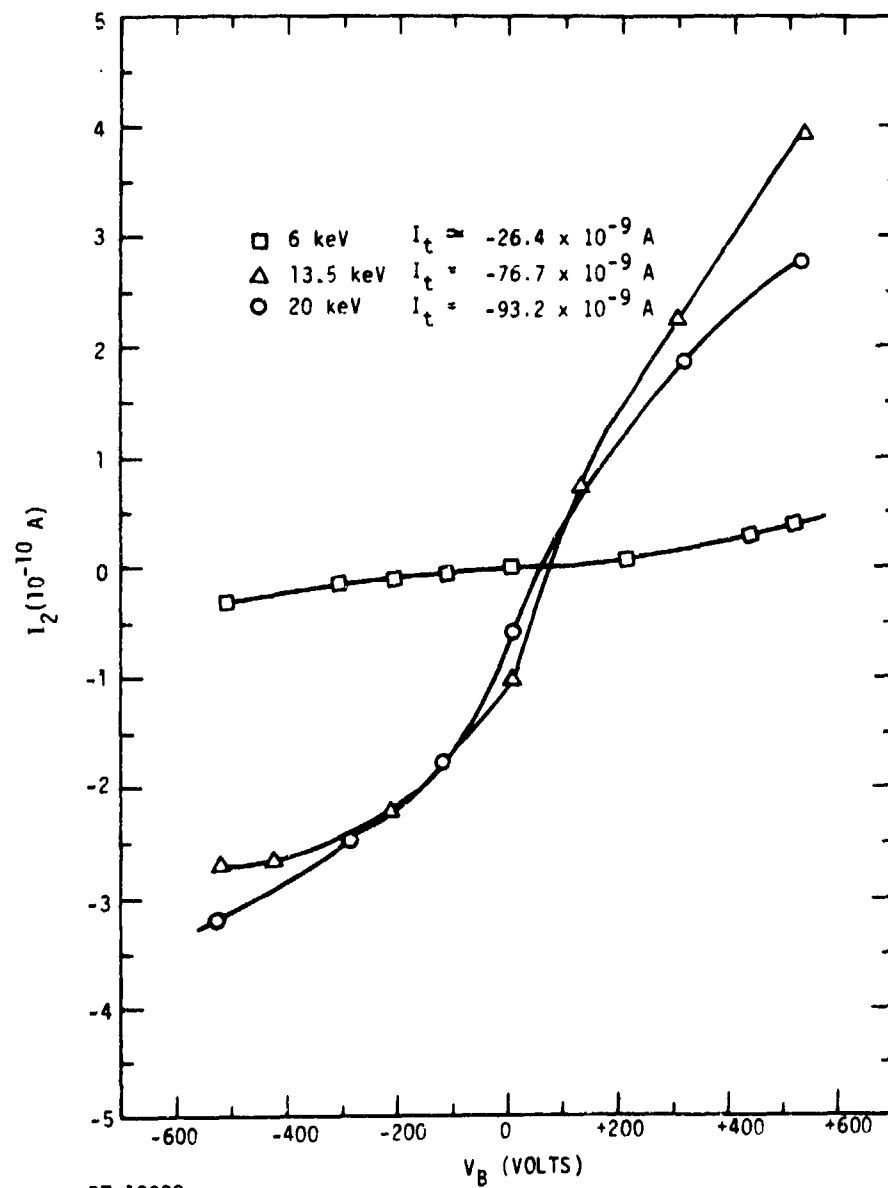
68

Figure 33. Leakage current through the rear electrode of a 25 μm Kapton sample as a function of incident electron energy and applied bias, T = 300°K

RT-18038

69

RT-18039

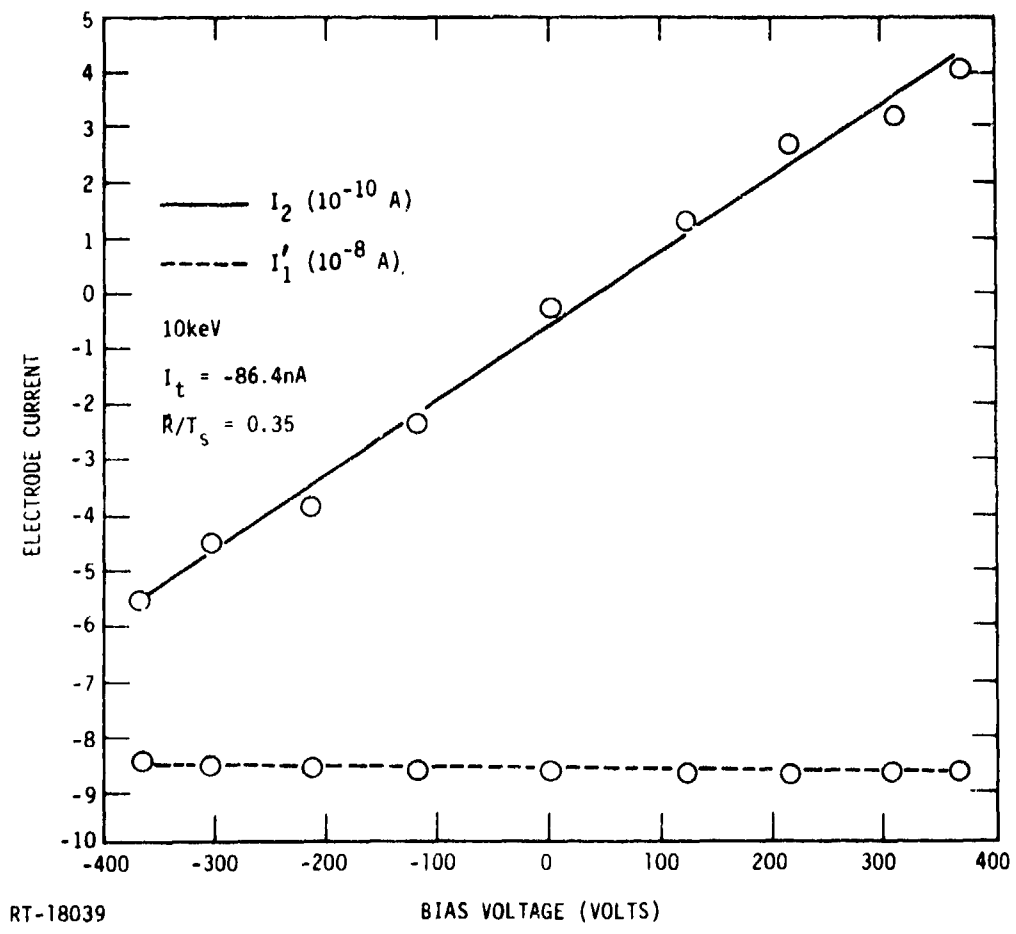Figure 34. Leakage currents as a function of bias voltage for a 7.6 μm
Kapton sample for E_i = 10 keV at 300°K

Figure 35. Electrode currents as a function of applied bias for a 7.6 μm Kapton sample exposed for E_i = 15 keV at 300°K
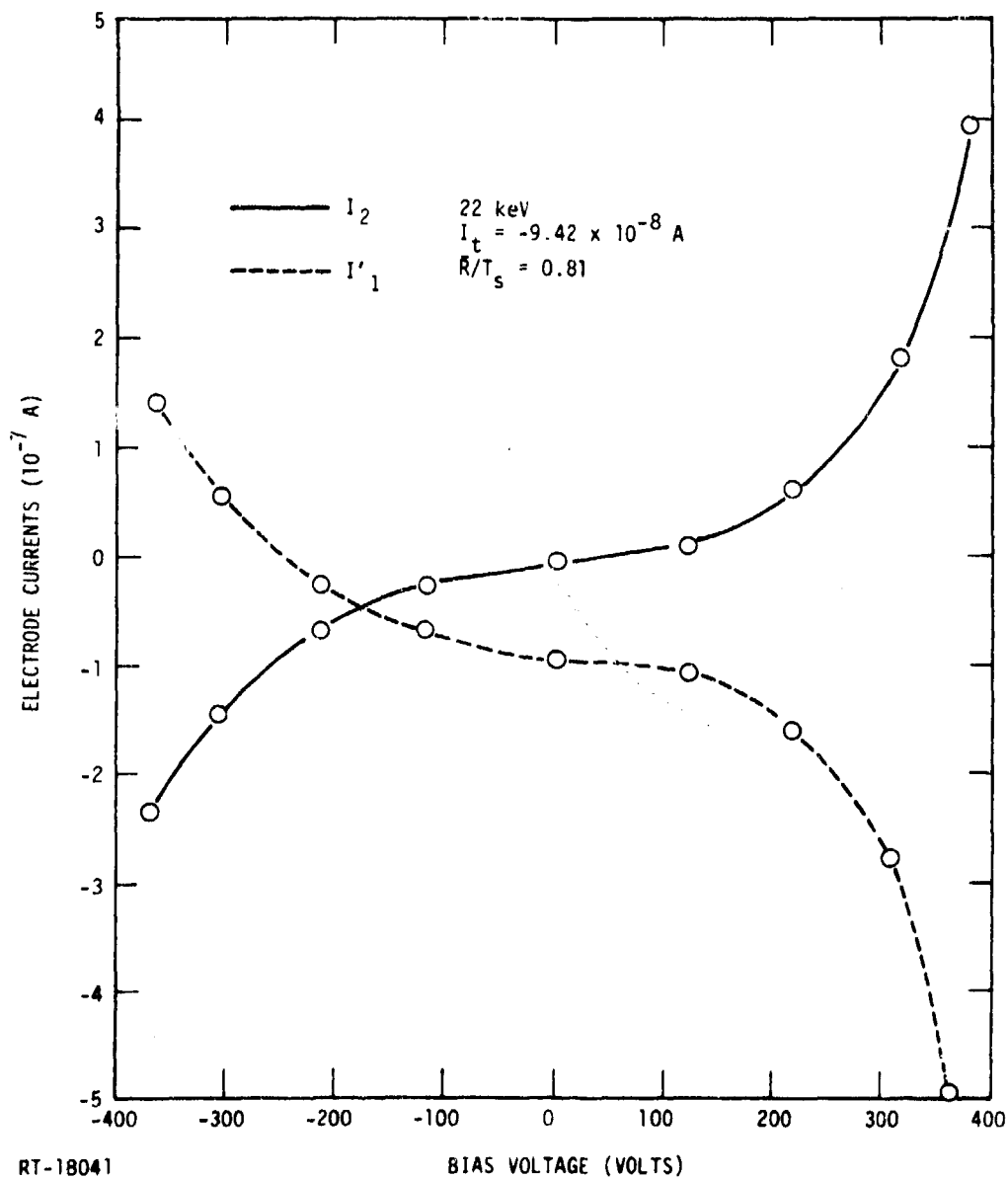
RT-18040

Figure 36. Electrode currents as a function of applied bias in a 7.6 μm Kapton sample for E_i = 22 keV at 300°K

RT-18041

RT-18048
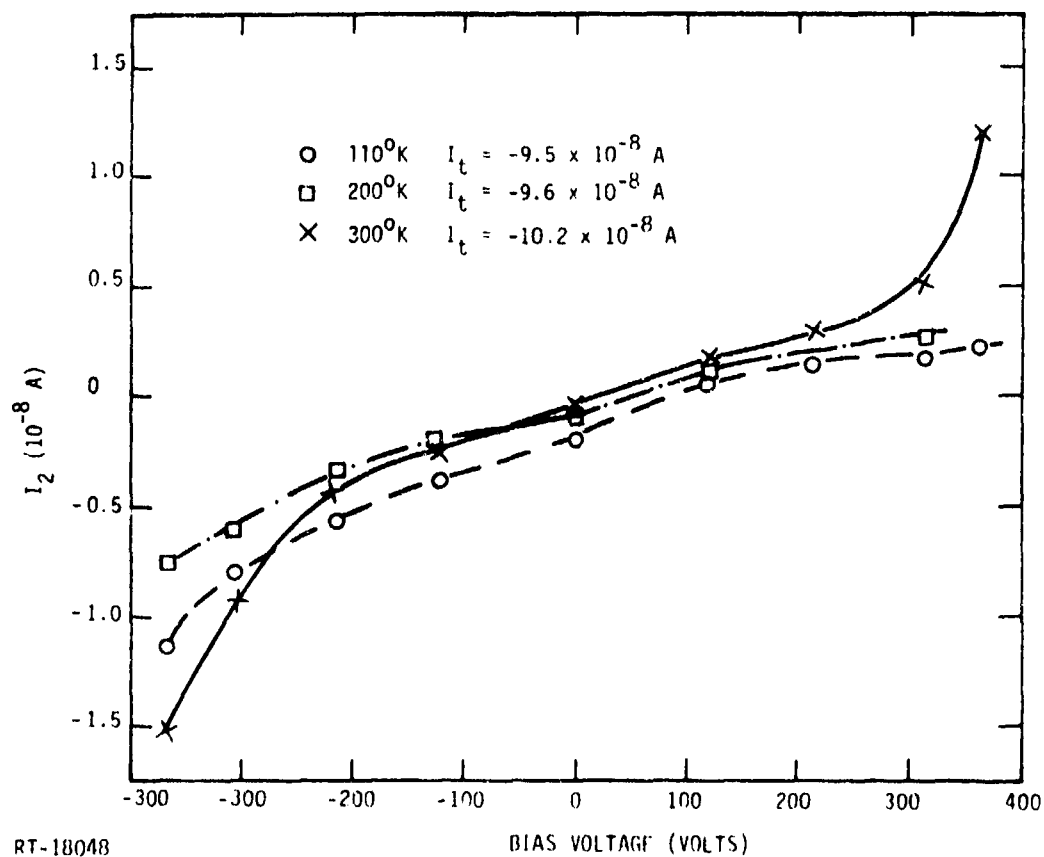
Figure 37. Rear electrode current (I_2) as a function of bias voltage and sample
temperature in 7.6 μm Kapton samples irradiated with 19 keV
electrons

+10
+9
+8 ⊙- - - - -⊙ 5 keV $I_t = -41.3 \times 10^{-9}$ A
+7 □—·—□ 10 keV $I_t = -54.4 \times 10^{-9}$ A
+6 △————△ 20 keV $I_t = -77.7 \times 10^{-9}$ A
+5
+4
+3
+2
+1
0
-1
-2
-3
-4
-5
-6
-7
-8
-9
-10

I_2 $(10^{-10}$ A$)$

-600   -400   -200   0   +200   +400   +600

BIAS VOLTAGE (VOLTS)

RT-19697

Figure 38. Leakage current (I_2) through rear electrode in 25 μm
Mylar S, T = 300°K

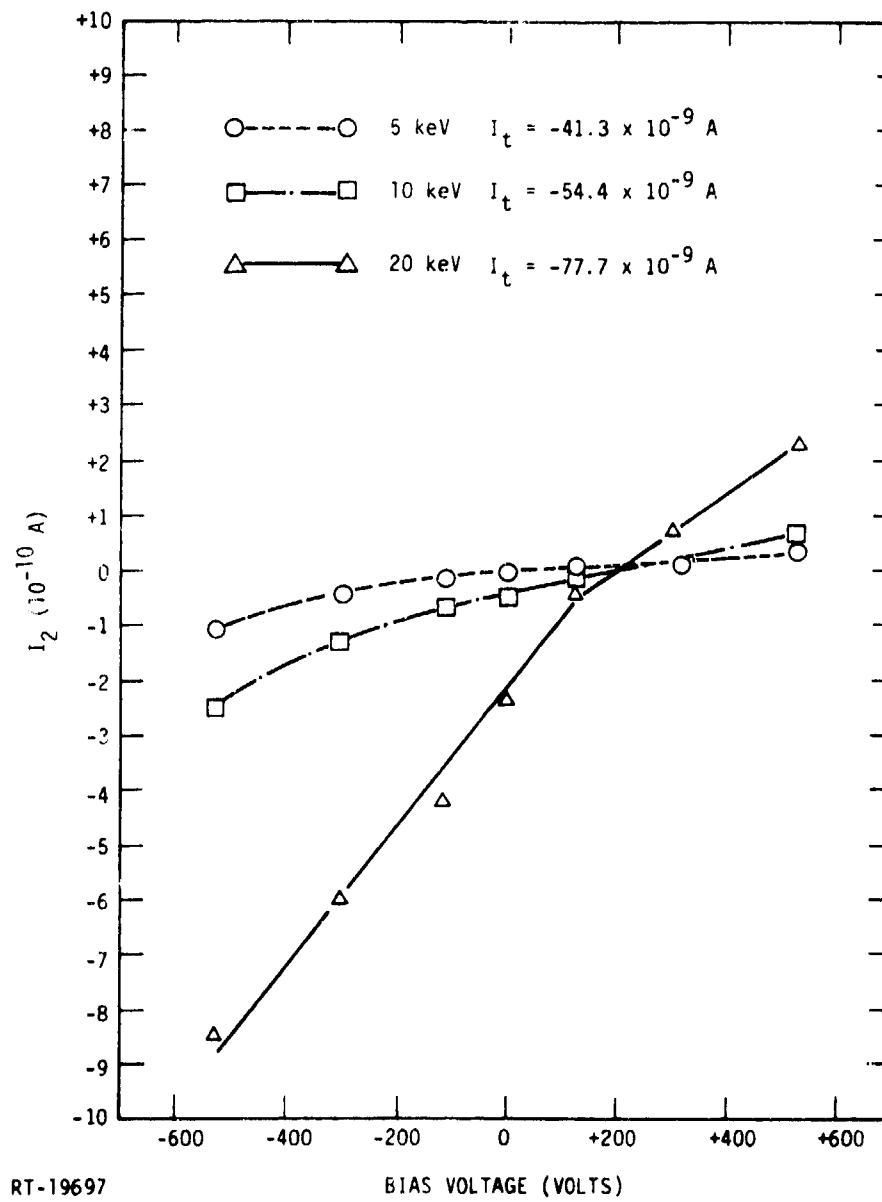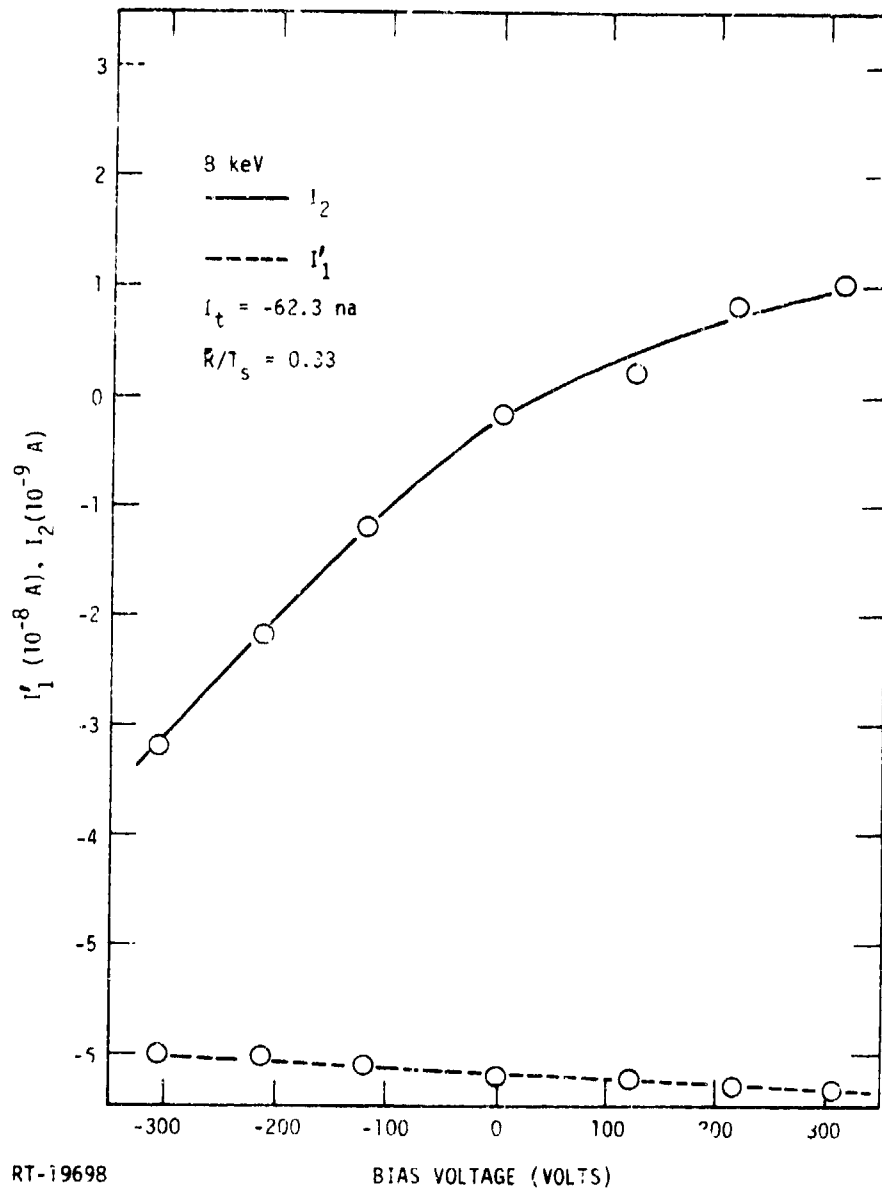**Figure 39.** Leakage current through 6.3 μm Mylar, $E_i = 8$ keV, 300°K

12 keV

I_2

I'_1

$I_t = -8.0 \times 10^{-8} A$

$\bar{R}/T_s = 0.52$

BIAS VOLTAGE (VOLTS)

I'_1, i_2 (10^{-8} A)

RT-19699
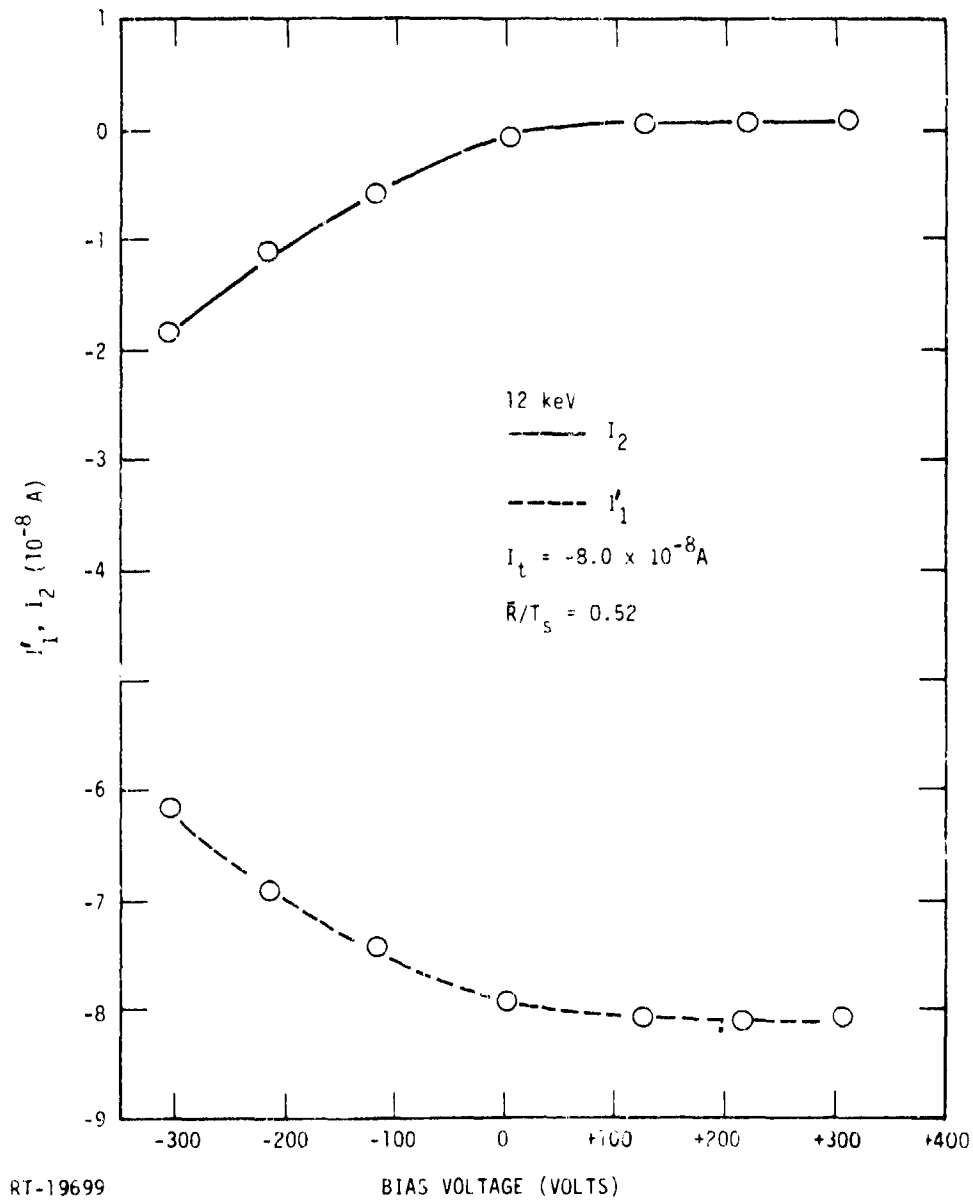
Figure 40. Leakage currents in 6.3 μm Mylar, T = 300°K
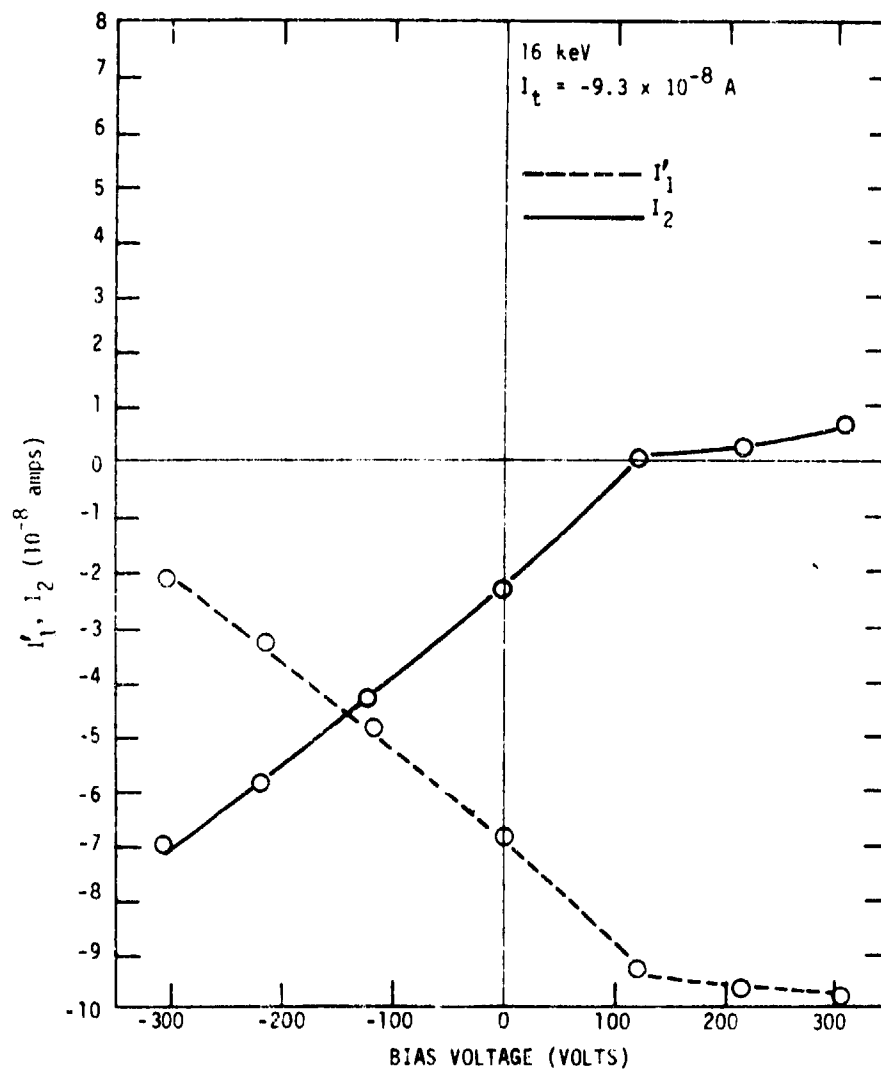
RT-16959

Figure 41. Bulk leakage current versus bias, 6.3 μm
Mylar S, 300°K
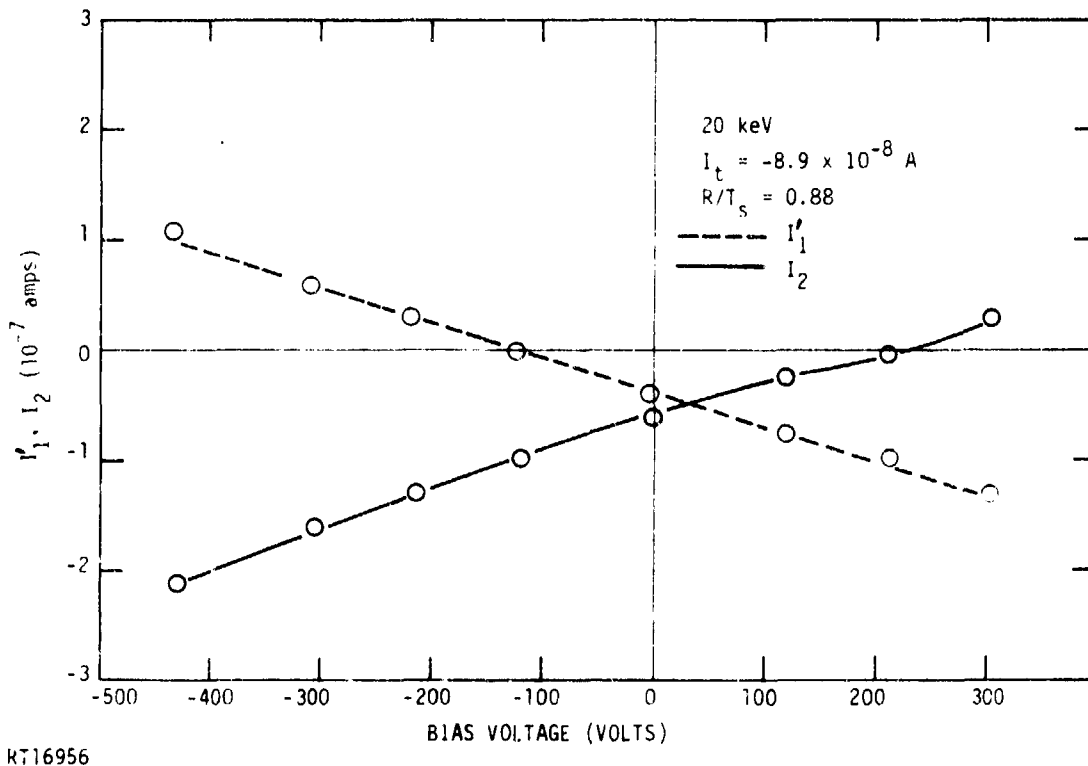
RT16956

Figure 42. Bulk leakage current versus bias, 6.3 μm Mylar S,
20 keV, T = 300°K
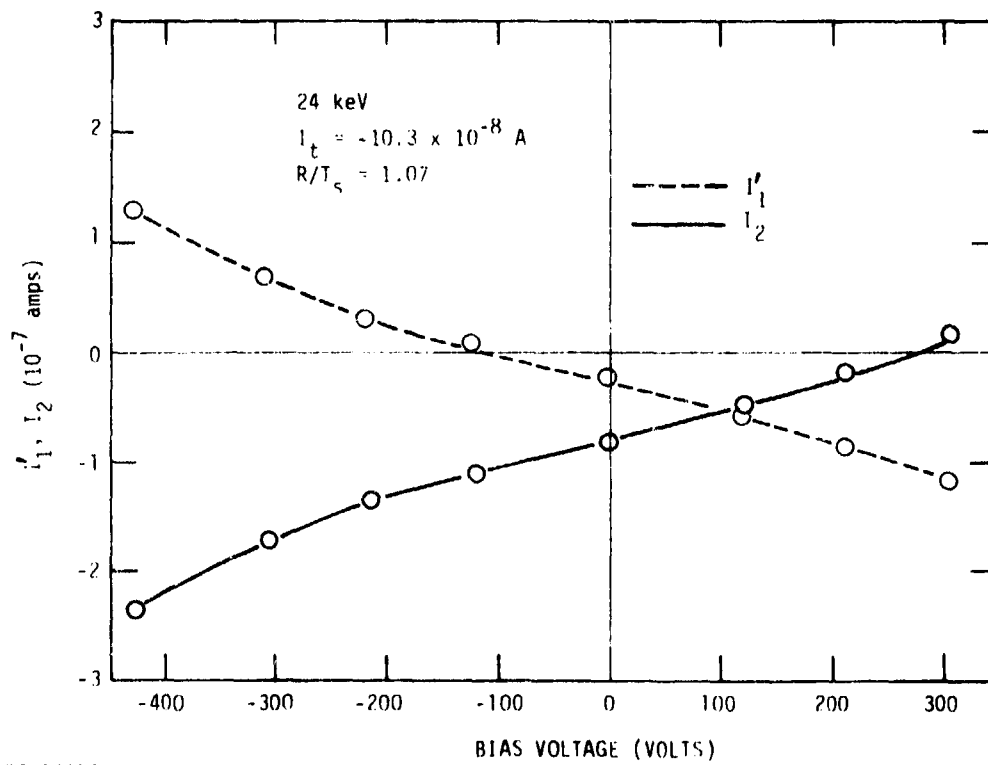
RT-16953

Figure 43. Bulk leakage current versus bias, 6.3 μm Mylar S,
24 keV, T = 300°K
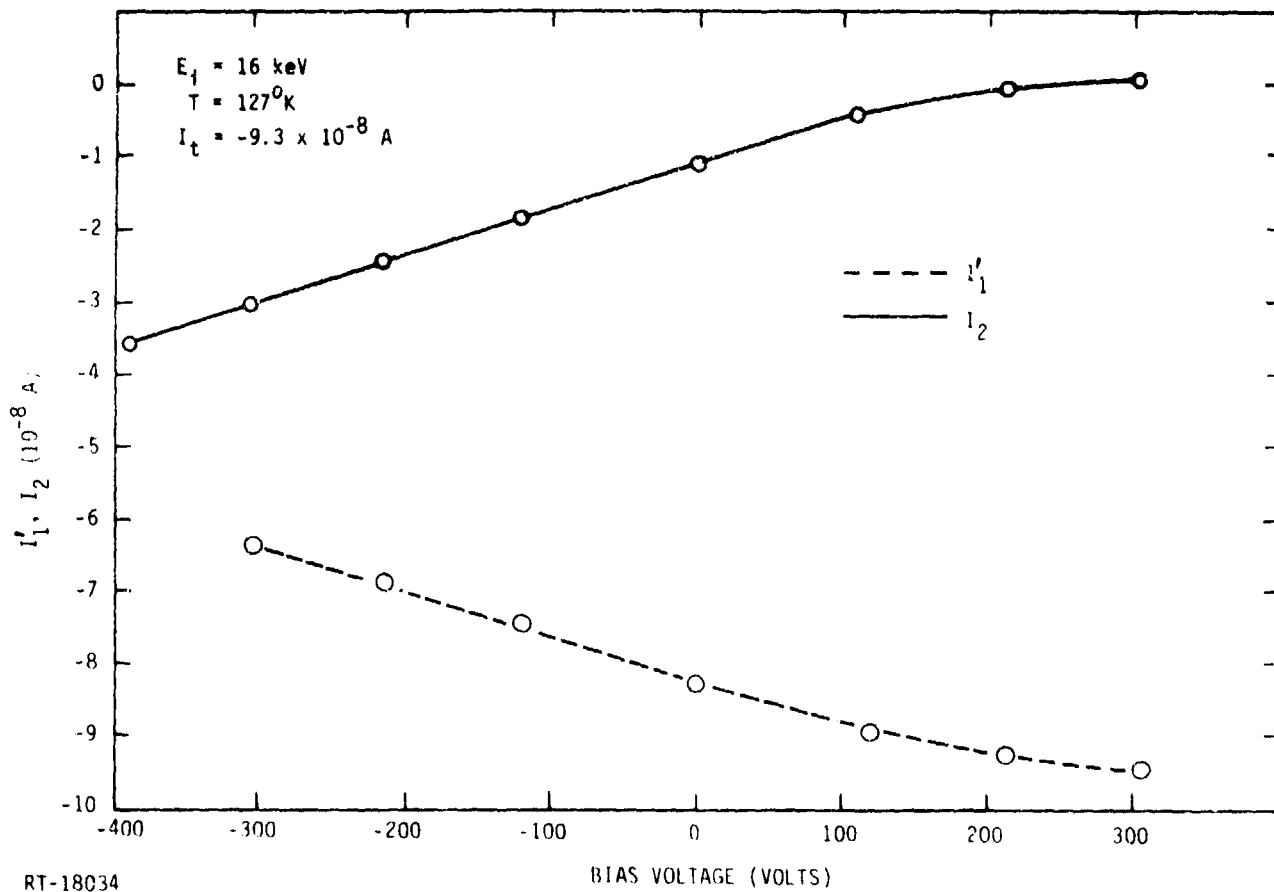
RT-18034

Figure 44. Leakage currents through a 6.3 μm Mylar sample as a
function of applied bias E_i = 16 keV, T = 127°K
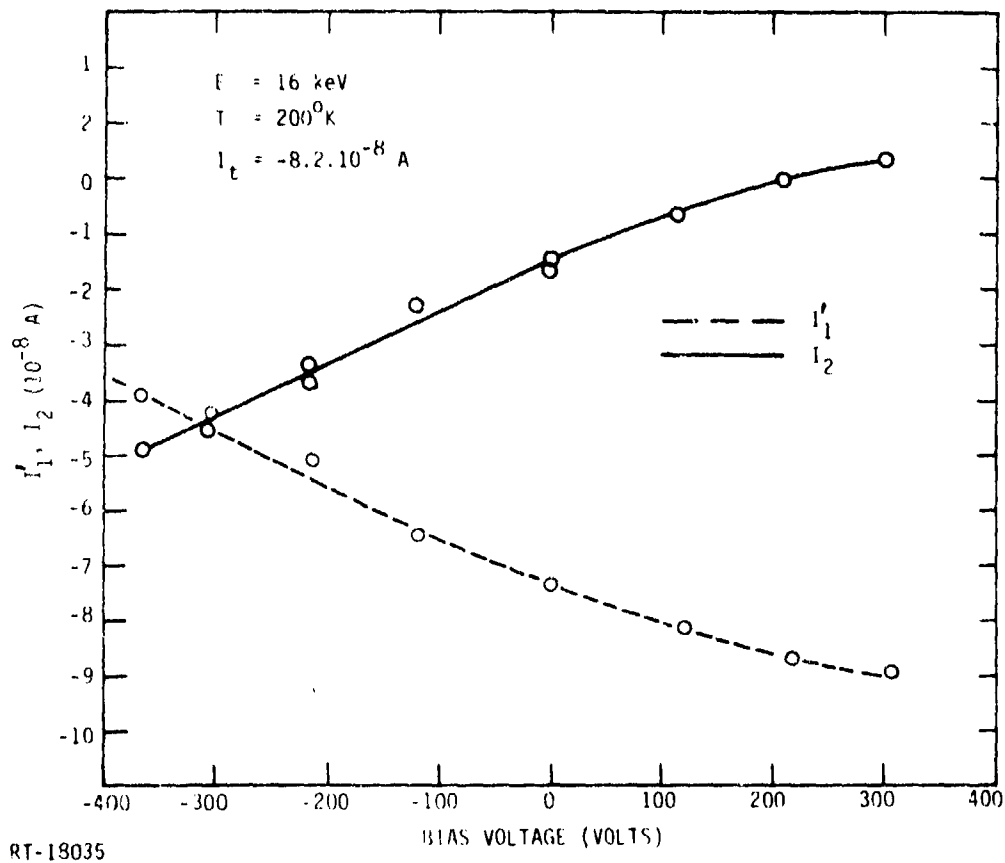
Figure 45. Leakage currents as a function of applied bias in a 6.3 μm Mylar sample, E_i = 16 keV, T = 200°K

RT-18035
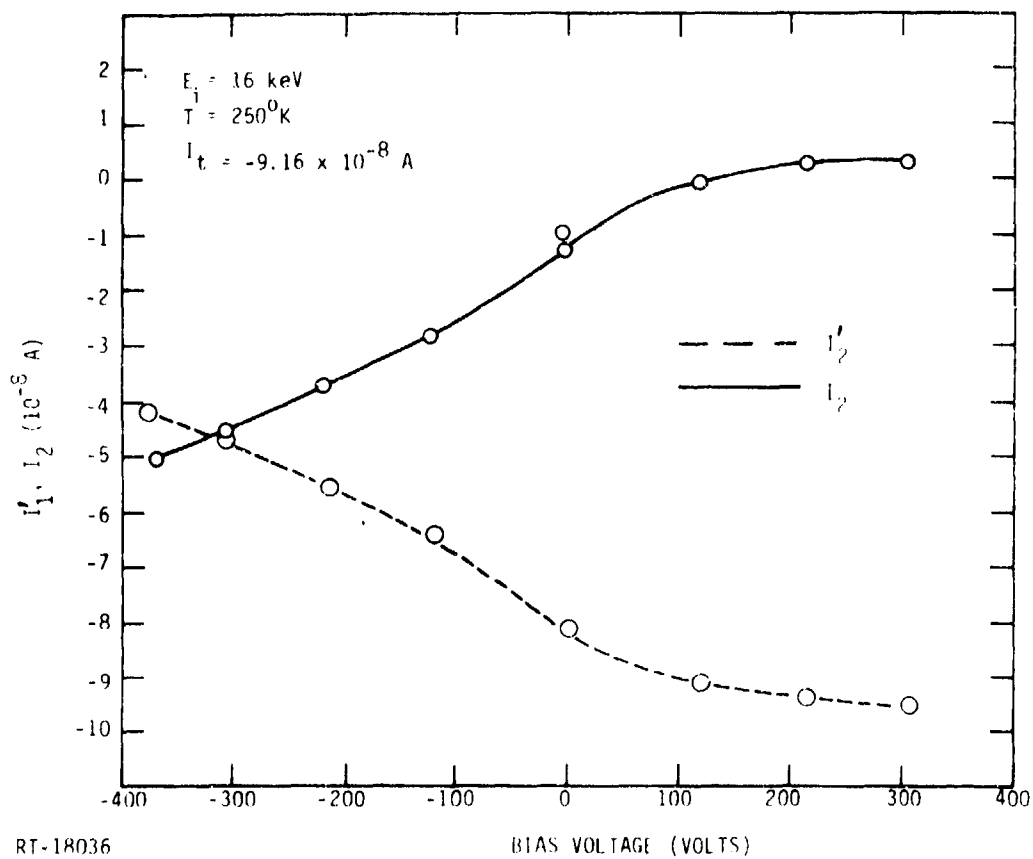
Figure 46. Leakage currents as a function of applied bias in a 6.3 μm Mylar sample, E_i = 16 keV, T = 250°K
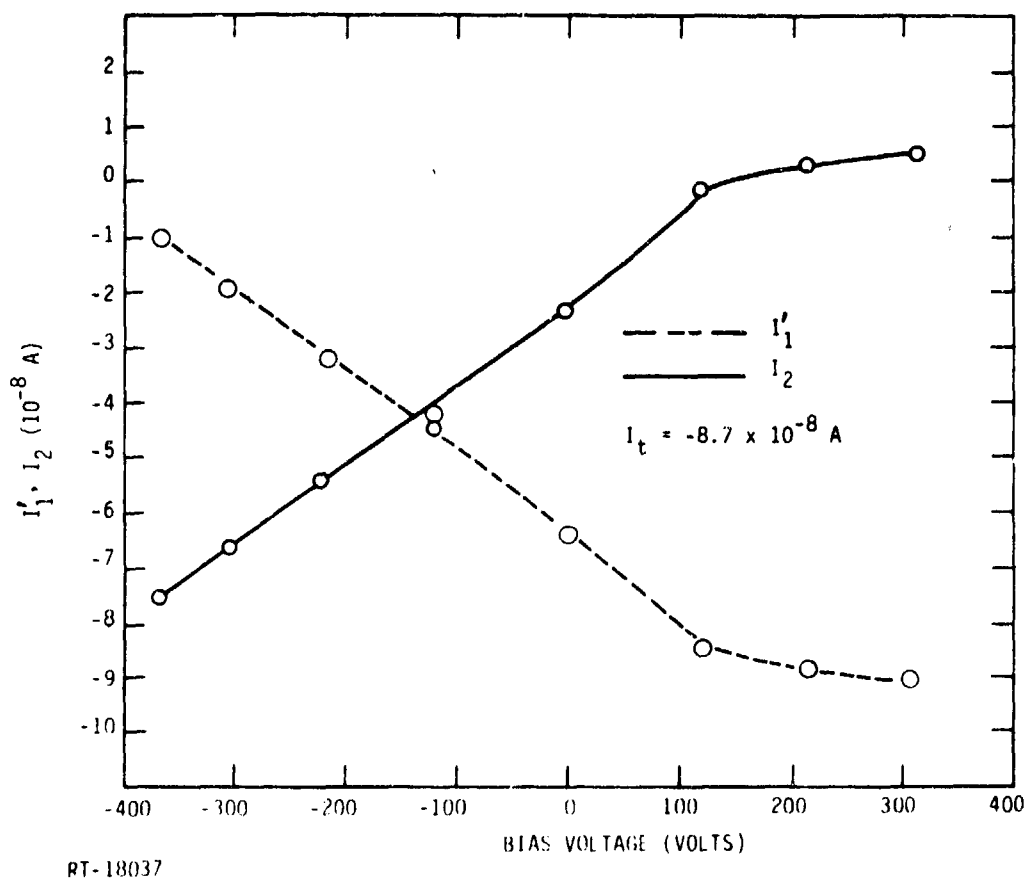
Figure 47. Leakage currents as a function of applied bias in a 6.3 μm Mylar sample, E_i = 16 keV, T = 300°K
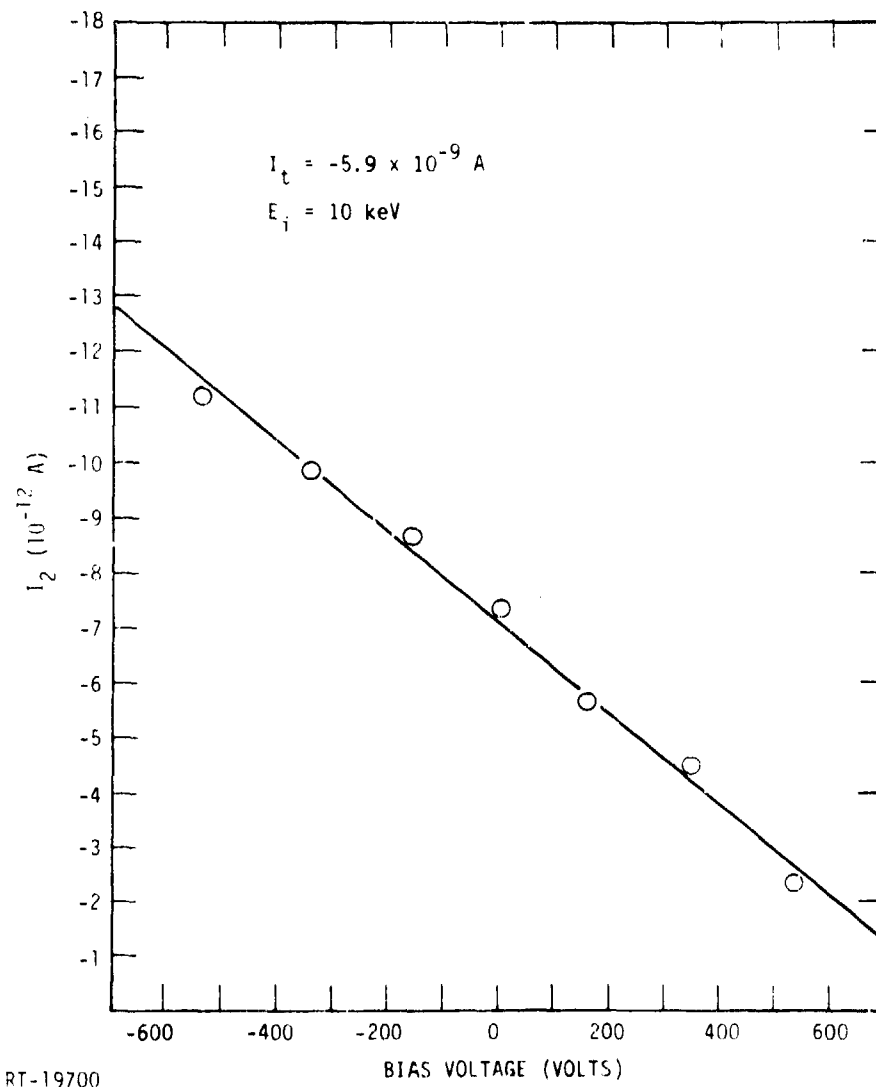
Figure 48. Rear leakage current from fused silica sample as a function of bias, $E_i = 10$ keV, $T = 300°$K

RT-19700

Figure 49. Rear leakage current from fused silica sample as a function
of bias, $E_i = 23$ keV, $T = 300^\circ K$

5.2 DISCUSSION

An examination of the data shows the following patterns:

1. Where $R/T_s < 1/2$, I_1' is $\simeq I_t$. $I_B = I_2$ changes with applied bias V_1 from negative ($V_1 < 0$) to positive values at some $V_o \geqslant 0$. It is typically several orders of magnitude lower than I_t. In some instances, I_2 vs V_1 is linear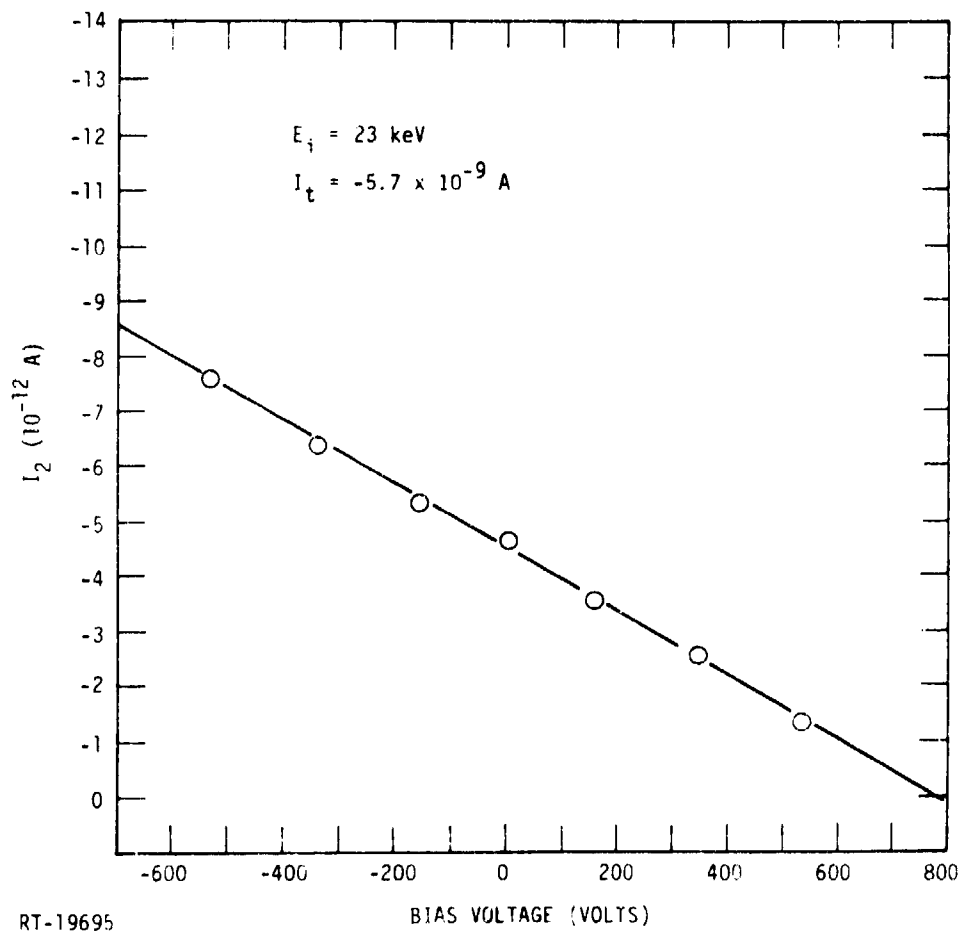. In this case, one is tempted to attribute the change in current with bias to the inherent dark conductivity. However, if one computes the apparent conductivity, it is an order of magnitude or more larger than the values given in Table 6. This implies that either the internal field is significantly enhanced because of space charge or as postulated, space-charge-limited current injection into region B occurs according to Equation 6. Neglecting space-charge enhancement of the conductivity in region B, the net conduction current density can be written

$$ J_B = g_{BO} \left[\frac{\sigma}{E} \frac{\overline{R}}{T_s} + \frac{V_1}{T_s} \right] \tag{39} $$

where σ is the equilibrium charge layer built up at $\overline{R}$. The values of V_1/T_s for the thinner samples is $\simeq 100\text{-}500$ kV/cm, whereas for the thicker samples it is about one-fourth of these. From Figures 26 and 28 one can see that E_2 due to space charge is ca. $10^3\text{-}10^4$ V/cm, a relatively small perturbation. Thus we are led to assume that the increase in I_2 is due to an increase in space charge limited currents.

2. Where $\overline{R}/T > 1/2$, I_2 approaches I_1' so that when $\overline{R}/D \simeq 0.75$ the two become relatively equal. In this case, I_1' will become positive for sufficiently negative V_1.

In order to analyze the leakage data, we employ the model developed by Nunes de Olivera and Gross (Ref 25) described in subsection 4.1. Briefly, it assumes that for a polymer or other dielectric sample irradiated under bias, the conductivity in region A is dominated by the radiation-induced conductivity term (Equation 12) and that in region B is dominated by space-charge conduction. Since we are interested in the equilibrium case, the displacement current term proportional to $\dot{E}$ - 0.

In this model, the injected space-charge layer serves as a virtual electrode for the injection of carriers into the nonirradiated region of the sample. The nature of this

electrode, whether injecting, ohmic, or blocking, is a function of the front electrode bias, the injection current density J_t, and g_D in the irradiated region. Several cases can be distinguished.

I. For $V_1 > V_{c'}$ where

$$V_{c'} = J_t T_s / g_D \qquad (40)$$

the virtual electrode is an ohmic anode ($E_B \neq 0$, ρ finite) and the predominant space charge carriers in Region B are holes.

II. For $V_0 < V_1 < V_{c'}$ where

$$V_0 = J_t \overline{R} / g_D \qquad , \qquad (41)$$

the virtual electrode is blocking (zero conduction current) and $I_2 = 0$. There is some dispute as to whether the virtual electrode is really blocking or whether the current remains small for $V_0 < V_1 < V_{c'}$ (Ref 41).

III. Between $V_c < V_1 < V_0$, where $V_c < 0$ and is given by (Ref 35, Equation 12)

$$V_c = \left(-\frac{8}{9} \frac{J_t}{\mu_- \epsilon} \right)^{1/2} (T_s - \overline{R})^{3/2} \qquad , \qquad (42)$$

the electrode is injecting. At $V_1 = V_c$, $I'_1 = 0$, a zero field plane exists, or equivalently a plane where $E \to 0$ and ρ to infinity so that the limit $(E\rho)$ is finite. This condition assures that I_B is finite and nonvanishing in region B. At the interface between regions A and B located at $\overline{R}_+$, $E(\overline{R}_+)$ 0 and an interface charge of density $\sigma = -\epsilon E_A$ exists. This charge layer serves as an injecting virtual electrode for electrons.

IV. For $V_1 < V_c$, the virtual electrode is ohmic and is injecting for electrons. One can define a quantity called the gain G (Ref 41, Equation 3) as

$$G = \frac{I_2}{I_t} = \frac{\epsilon \mu_-}{|J_t|} \left[-V_B - \frac{(G-1)\overline{R}|J_t|}{g_D} \right]^2 (T_s - \overline{R})^{-3} \qquad . \qquad (43)$$

G is written in closed form in Equation 43. The equation was solved iteratively because of its presence on both sides of the equation. Our V_1 is the potential difference between the front and rear electrodes, corresponding to our experimental setup. The authors of References 25 and 41 define V in the opposite sense. Hence, their V is equal to $-V_1$.

We have attempted to test the theory and the validity of our material parameters by calculating V_o, V_c, and G where the data was available. No attempt was made to develop complete $G(J_t, V_1, E_1)$ curves. Note that μ is the effective trap modulated mobility in the nonirradiated region of the polymer and can be different for conduction by electrons (μ_-) or holes (μ_+). For the conditions under which these calculations were performed, the mobilities are for electrons (μ_-).

In Table 8 we have listed the effective and measured I_2 crossover voltage (V_o) for each of the materials, along with the experimentally determined values V_o(exp). We have used the measured value of J_t, $\bar{R}$ and g_D in each case. It can be seen from the data, that, in most cases, the agreement between experiment and theory is fair, being within a factor about three. Possible sources of error include difficulty in determining the crossover point, the method employed to calculate dose rate and the simplified nature of the model.

Table 8. Calculation of Crossover Voltages (V_o)

Material	Thickness (μm)	Temp. (°K)	Energy (keV)	J_t (na/cm²)	$g_D \left[10^{-14} (\Omega\,cm)^{-1}\right]$	$\bar{R}$ (μm)	$J_t\bar{R}/g_D$ (volts)	V_o(exp) (volts)
Mylar	6.3	300	8	1.48	0.42	2.1	74	45
			12	1.91	0.67	3.3	94	55
			16	2.22	0.76	4.5	131	120
			20	2.35	0.89	5.7	149	230
Mylar	25.4	300	5	0.98	0.15	1.25	82	ca. 20
			10	1.30	0.46	2.7	75	ca. 180
			20	1.85	0.66	5.65	158	ca. 190
FEP	25.4	300	5	0.51	0.22	1.1	26	0
			10	1.16	0.91	1.6	20	60
			15	2.17	1.6	2.3	32	60
			20	2.17	1.6	3.1	41	130
Kapton	7.6	300	10	1.63	5.0	2.7	9	ca. 30
			15	2.08	6.6	4.2	13	ca. 40
			22	2.24	7.5	6.2	18	ca. 45
Kapton	25.4	300	6	0.63	1.5	1.5	6.4	ca. 30
			13.5	1.85	5.4	3.9	13.0	70
			20	2.22	6.9	5.7	18	60

In Table 9, we have employed Equation 42 to determine effective values for the electron mobility in Mylar and Kapton. All of the parameters were experimentally derived. In several cases, as indicated, V_c was estimated. The values for μ_- in Mylar at $300°K$ are about an order of magnitude lower than those reported in Reference 42 for this polymer. A similar value of ca. 3×10^{-13} cm^2/V sec was derived for Kapton. However, room temperature mobilities of this magnitude are not unreasonable for polymers (Refs 24,37).

Table 9. Calculation of Electron Mobilities in Region B

Material	Thickness (μm)	Temp. ($°K$)	E (keV)	$\overline{R}$ (μm)	J_t (na/cm^2)	V_c (volts)	μ_- ($10^{-13} cm^2/$V sec)
Mylar	6.3	300	16	4.5	2.22	-400	2.4
	6.3	300	20	5.65	2.35	-120	1.3
Mylar	6.3	127	16	4.5	2.22	-1310^a	0.22
	6.3	200	16	4.5	2.0	-762^a	0.61
	6.3	250	16	4.5	2.18	-771^a	0.63
	6.3	300	16	4.5	2.07	-450	1.8
Kapton	7.6	300	22	6.2	2.24	-250	2.8

[a]Value for V_c estimated from slope of I'_1 vs V_1 curve.

In Table 10, we have calculated current gains G with Equation 43. For Mylar and Kapton, agreement between prediction and measurement was within a factor of ten. The reason for this relatively large discrepancy has not been determined. The

Table 10. Gain Calculations

Material	Thickness (μm)	V_B (volts)	Energy (keV)	J_t (na/cm^2)	$g_D [10^{-14}$ $(\Omega cm)^{-1}]$	$\overline{R}$ (μm)	μ_- ($10^{-12} cm^2/$Vsec)	G_{calc}	G_{exp}
Mylar	25.4	-500	5	0.98	0.15	1.25	0.2^a	1.5×10^{-3}	2.4×10^{-3}
		-500	10	1.30	0.46	2.7	0.2^a	1.3×10^{-3}	4.0×10^{-3}
		-500	20	1.85	0.66	5.65	0.2^a	1.8×10^{-3}	1.1×10^{-2}
Kapton	25.4	-200	13.5	1.83	5.4	3.9	0.28^a	2.3×10^{-4}	3.0×10^{-3}
		-200	20	2.22	6.9	5.7	0.28^a	2.6×10^{-4}	2.7×10^{-3}
FEP	25.4	-200	10	1.16	0.91	1.6	4.0^b	2.6×10^{-3}	2.1×10^{-3}
		-200	20	2.17	1.6	3.1	4.0^b	2.0×10^{-3}	2.2×10^{-3}

[a]Calculated from Equation 42.

[b]From the experimental gain data.

experimental gain data was used to provide an estimate of the trap modulated mobility in Teflon FEP at $300°K$. Values of ca. 4×10^{-12} cm^2/V sec were obtained, which is comparable to those derived in Reference 37 for holes in this material, but much higher than that reported for electrons.

In summary, the simple model of Nunes de Olivera and Gross predicts in a general way the trends in the experimental data, but a more detailed analysis which fits the data to a specific trap structure is required. Additional experiments, in particular those of the kind described in Reference 43 to determine the detailed charge distribution, would be useful. Also necessary are thermally stimulated current measurements on electron charged polymers of interest of the type described in Reference 37 to determine more detailed information about trap distributions. Another useful activity to pursue would be the development of transport-type models of the kind developed by Berkeley (Ref 44) and Beers (Ref 45), in which realistic models of conductivity, including space-charge transport, and trapping kinetics are included.

6. SURFACE LEAKAGE MEASUREMENTS

6.1 DEFINITION OF THE PROBLEM

This section describes measurements of surface current flow under electron irradiation. The objective of these experiments was to measure the radiation-induced enhancement of surface leakage currents in insulator materials subjected to electron irradiation. From such measurements it was hoped that values for a dose-dependent surface conductivity could be derived.

The intent of the experiment is demonstrated with the aid of Figure 50. As shown in the figure, the sample has two strip electrodes on the irradiated surface. During

RT-18019
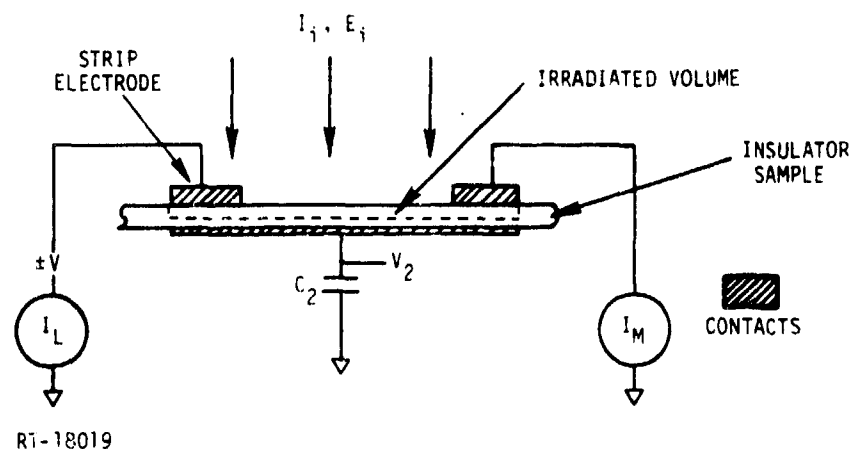
Figure 50. Schematic representation of method for measuring surface leakage current.

irradiation by a nonpenetrating electron beam, the surface conductivity of the nonelectroded sample between the contact strips will be enhanced by radiation-induced conductivity, and the current flow between the contacts will be a function of this conductivity, the applied bias, and also the electric field that results from charge buildup in the insulator material.

A simple analysis will point out the difficulties of such an experiment. Consider an insulator sample whose thickness is large compared to the electron range irradiated

by an incident flux J_i and with a grounded front electrode of area A, as shown in Figure 51.

For this geometry, if $\overline{R}/T_s < 1/2$ the leakage current to the rear electrode through the nonirradiated volume of the insulator is essentially zero and can be neglected for this discussion. At the onset of irradiation, a charge layer will build within the sample to a maximum value of
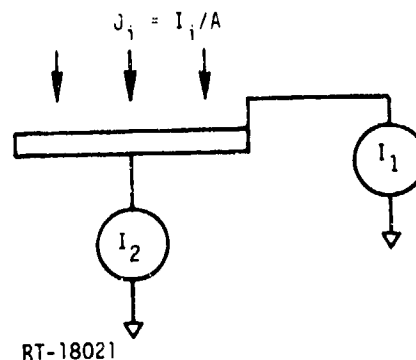

Figure 51. Short circuit irradiation of an insulator sample

$$Q_t = J_t A \tau_D \tag{44}$$

where J_t is the injected current density and τ_D is the dielectric relaxation time given by

$$\tau_D = \frac{\epsilon}{g_D} \left(\frac{T_s}{T_s - \overline{R}} \right) \tag{45}$$

with T_s the sample thickness and $\overline{R}$ the mean electron range. During this time I_1 will increase until an equilibrium value equal to $(J_i - J_b)A$ is reached. This value of current will always be present as a background signal in an experiment designed to measure the surface leakage current between two electrodes on an insulator sample.

In general, the observed current I_1 will be equal to

$$I_1 = I_i - I_b - I_2 = I_0 - I_2 \quad , \tag{46}$$

where I_b is the net back-emitted current equal to $I_\eta + I_\delta$ the sum of the backscattered and secondary emission currents. In general, $I_0 \neq I_t$. The latter is the current actually injected into the polymer sample and is given by $I_i \tau$. Values for τ have been given in Figure 14. In the experiment, the minimum current that will be observed without bias is $I_{0\epsilon} = J_i A_\epsilon - I_{b\epsilon}$, where $I_{b\epsilon}$ is the net current back emitted from the electrodes of area A_ϵ. The maximum current is the sum of $I_{0\epsilon} + I_{0D}$, where $I_{0D} = J_i A_D - I_{bD}$ and A_D

is the nonelectroded dielectric sample area, depending on the amount of charge which can travel to the electrodes. This argument indicates that the contact area should be made as small as possible.

An estimate of the sensitivity of the experiment can be made using the sample geometry electrode area and the ionization-induced conductivity in the insulator material. The sample geometry used for surface leakage measurement is discussed and analyzed in the following section.

6.2 GEOMETRY OF SURFACE LEAKAGE SAMPLES

The sample had a meshed comb configuration (Figure 52) in which alternate electrodes were connected in parallel. To minimize the area of the electrodes, an evaporation mask was made using photolithography and chemical milling techniques. This provided electrodes 8 mils wide and spaced 8 mils apart. Array L (Figure 52) consisted of 11 electrodes in parallel and Array M had 10 parallel electrodes. The irradiated areas were as follows:
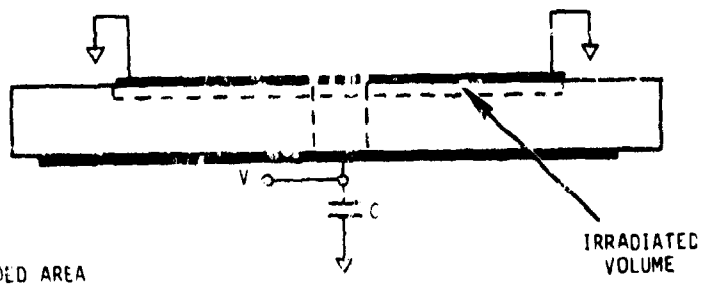
Array L	1.84 cm^2;
Array M	1.68 cm^2;
Nonelectroded sample	3.28 cm^2;
Total irradiated area	6.8 cm^2.

Using this geometry, one can estimate the expected current flow as a function of applied bias for a given electron irradiation. The following is assumed:

Sample, Mylar S;
Density (d), 1.38 g/cm^3;
Electron energy (E_i), 12 keV;
Practical electron range (R_p), 3.4×10^{-4} cm;
Current density (J_i), 3.3×10^{-9} A/cm^2;
Radiation conductivity $g_D = 6.34 \times 10^{-18} \dot{D}^{0.77}$.

To calculate the resistance of the array we assume parallel bar shaped insulator samples whose width is defined by the electrode spacing and whose cross section area is defined by the electron range and the sample length $[2\ell x(n-1)]$ where ℓ is the length of individual samples defined by the electrode length and n is the total number of electrodes. The resistance is then calculated by $R = \ell/\sigma A$. The geometry factor is

ELECTRODE AREA = 3.52 cm^2
SAMPLE AREA = 3.28 cm^2

ELECTRON BEAM
COLLIMATOR
(TOTAL EXPOSED
AREA = 42 cm^2)

ELECTRODED AREA

IRRADIATED
VOLUME
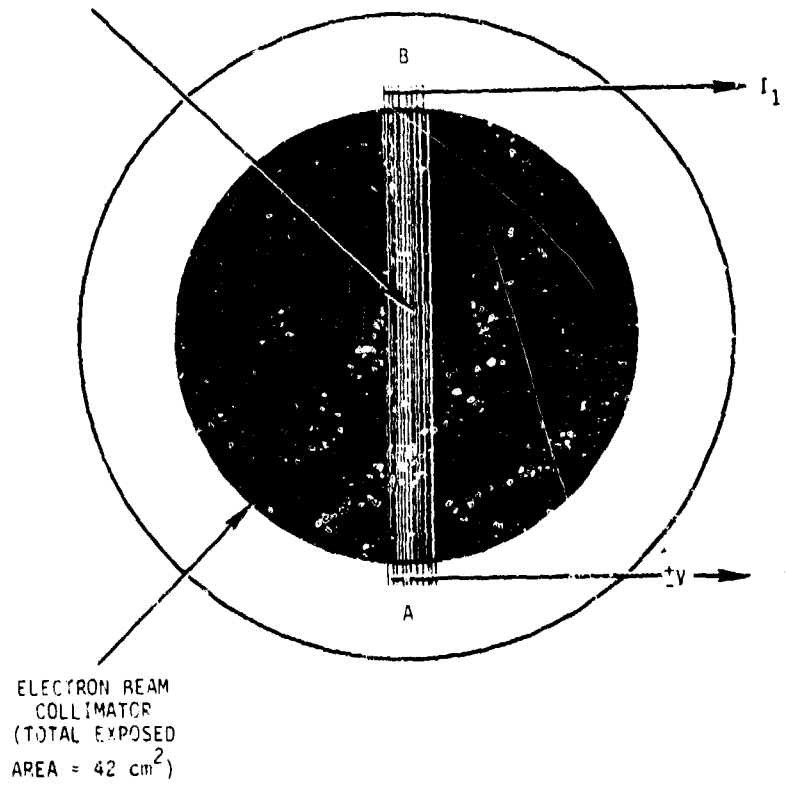
RT-13023

Figure 52. Geometry of samples used for surface leakage measurements

$$\frac{\ell}{A} = \frac{2.15 \times 10^{-2}}{2 \times 7.62 \times (21-1) \times 3.4 \times 10^{-4}} = 0.21 \quad .$$

The dose rate $\dot{D}$ in rads(Mylar)/s is approximately

$$\dot{D} = \frac{J_i \cdot E_i \cdot 10^5}{d \cdot R_p}$$

$$= \frac{3.3 \times 10^{-9} \times 12 \times 10^3 \times 10^5}{1.38 \times 3.4 \times 10^{-4}}$$

$$= 8.45 \times 10^3 \text{ rads(Mylar)/s} \qquad (47)$$

neglecting backscatter. The radiation-induced conductivity for this dose rate is 6.7×10^{-15} $(\Omega\,\text{cm})^{-1}$ and the sample resistance between the two arrays is

$$R = \frac{0.21}{6.7 \times 10^{-15}} = 3.1 \times 10^{13}\,\Omega \quad .$$

This value of resistance yields a current sensitivity of $\sim 3.2 \times 10^{-14}$ amperes-per-volt bias. We now compare this current with that expected as a result of irradiating the electroded area of the sample. For this we assume a transmission coefficient (I_t/I_i) of 0.5 for 12 keV electrons and the 350 Å thick gold electrode (cf. Figure 14) and a coefficient of unity for the nonelectroded sample. In equilibrium, the current flow in the two electrode arrays is

| Current	Array	Area	$0.5\,J_i\,A_\epsilon$
I_L	L	1.84 cm^2	3.03×10^{-9} A
I_M	M	1.68 cm^2	2.78×10^{-9} A

As shown above, the current flow in I_1 and I_2 due to the electrodes above ($\sim 2.9 \times 10^{-9}$ amps) is much larger than the current sensitivity of $\sim 3 \times 10^{-14}$ amperes/volt bias expected due to radiation-induced conductivity. In a differential experiment,

95

one might hope to cancel out the common mode currents collected by electrode sets L and M. This depends on creating a perfectly symmetric system. It can be seen that the practical difference of $\sim 3 \times 10^{-10}$ amperes is still large compared to the current sensitivity. Therefore, one would not expect to see a current-bias voltage dependence for this configuration.

A simple calculation will demonstrate this. Consider the idealized system shown in Figure 53. Following (Ref 46), one can show that the potential distribution in equilibrium is given by
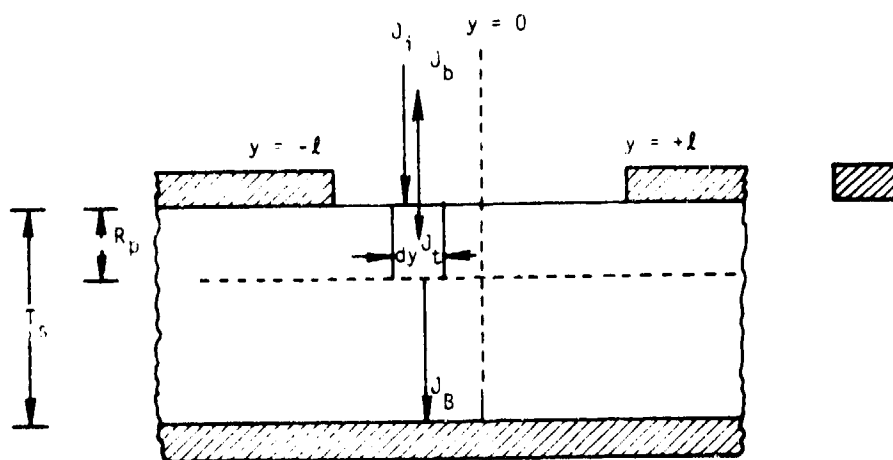
(A)   SURFACE CHARGING GEOMETRY
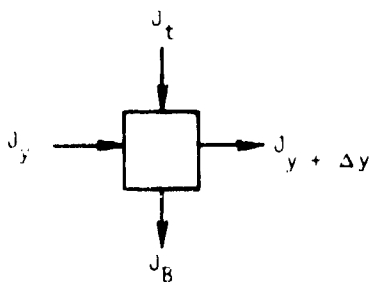
$$J_t \, \Delta y = (J_i - J_B) \, \Delta y \qquad J_y = - q_D \, R_p \frac{dV(y)}{dy} \qquad J_B = - \frac{V(y)}{T_s} g_o$$

$$J_t \, \Delta y - J_B \, \Delta y + J_y - J_{y + \Delta y} = 0 \qquad V(\pm \ell) = 0$$

(B)   CURRENT BALANCE EQUATION

RT-18022

Figure 53. Surface charging model

$$V(y) = \frac{J_t T_s}{g_0} \left[\frac{1 - \cosh(ay)}{\cosh(a\ell)} \right] \quad , \quad -\ell \leqslant y \leqslant \ell \quad , \tag{48}$$

where

$$a = \left(\frac{g_0}{g_D R_p T_s} \right)^{\frac{1}{2}}$$

for a dielectric of thickness T_s, dark conductivity g_0, irradiated by electrons of incident energy E_i, range $R_p(E_i)$, which create a radiation conductivity g_D in a volume bounded by R_p. For $E_i = 12$ keV, $R_p = 3.4 \times 10^{-4}$ cm, $J_i = 3.3 \times 10^{-9}$ A/cm^2, $g_D = 6.7 \times 10^{-15}$ $(\Omega\,\text{cm})^{-1}$, $d = 2.54 \times 10^{-3}$ cm, $\ell = 10^{-2}$ cm, and $g_0 = 10^{-18}$ $(\Omega\,\text{cm})^{-1}$, one finds that

$$\Delta V \leqslant (0.6) \times 3.3 \times 10^{-9} \, (\text{A/cm}^2) \times \frac{2.54 \times 10^{-3} \, \text{cm} \times (0.01)}{10^{-18} \, (\Omega\,\text{cm})^{-1}}$$

$$< 5 \times 10^4 \, \text{V} \quad .$$

The model on which this calculation is based yields an overestimate for the following reasons. First as the sample is charged up, the effective energy of incident particles is diminished. Hence, secondary electron production increases. If this were an infinite plane, the front surface potential would rise to a voltage such that the difference between the accelerating voltage and front surface voltage (relative to ground) is equal to the second crossover voltage, i.e., where the back-emission yield is unity unless breakdown occurred. The data of Reference 47 indicate that this is about 800 eV for Mylar. Then the maximum potential difference attained would be about 11 keV for the given charging conditions. In fact, measured data indicates that the potential reached before breakdown is much smaller (q.v., subsection 6.3). In addition, as the front surface potential buildup, more deposited charge will leak to the rear electrode. The point to be made is that the fields generated by deposited charge are large compared to those which can be applied across gap samples. Clearly, to more accurately model this experiment requires a dynamic two-dimensional charging model. It would be interesting to apply NASCAP to this problem. NASCAP is not presently set up to handle internal charging, i.e., it assumes that $R/T_s \ll 1$. However, it should be possible to examine surface charging of relatively thick samples.

6.3 RESULTS OF SURFACE LEAKAGE MEASUREMENTS

A 25 μm thick type S Mylar sample was prepared with the electrode configuration discussed above and data were taken for 8 and 12 keV electron irradiations at 300°K. A significant difference, both in time dependence and magnitude of current flow and charge buildup, is observed when comparing 100 percent electroded samples with the surface leakage sample. This is shown in Figure 54 which compares the results of a
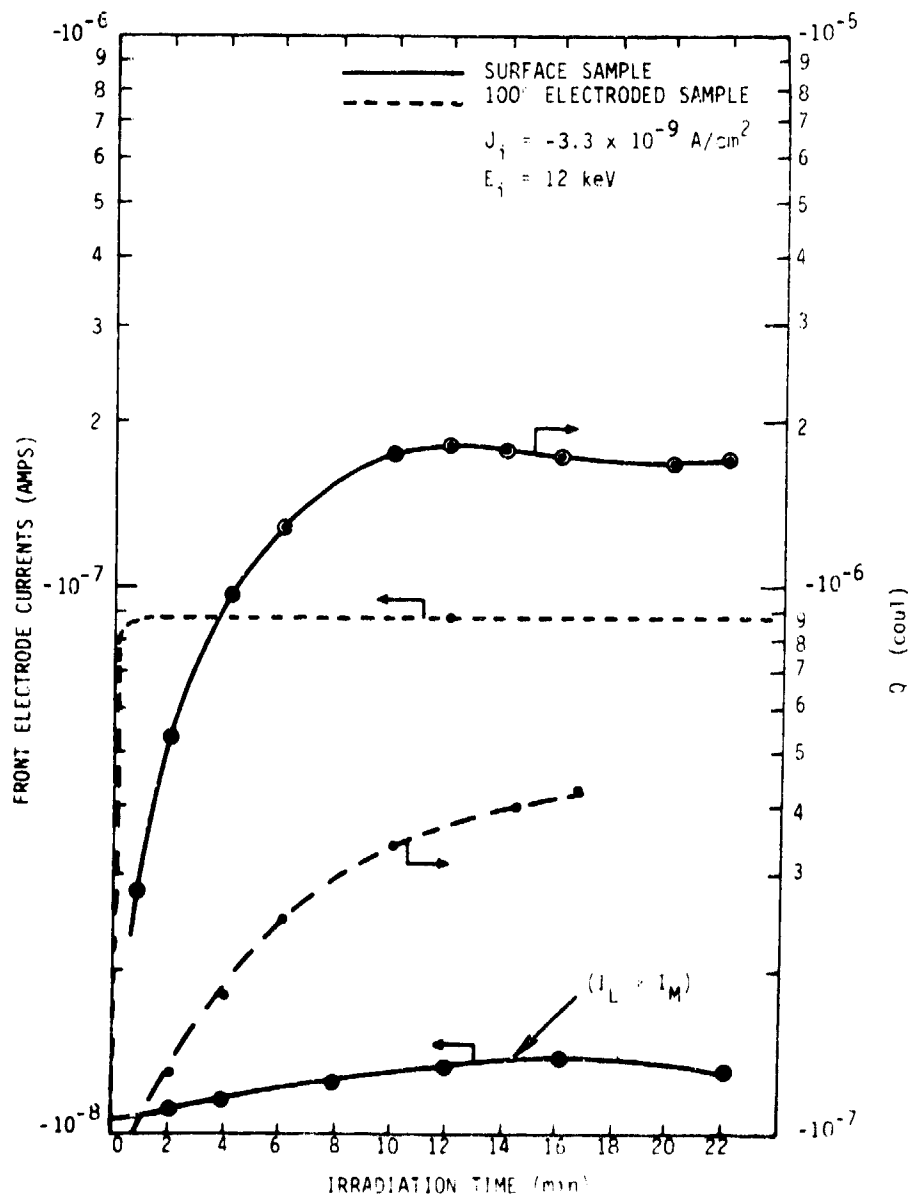

RT-18024

Figure 54. Comparison of charge and current buildup in surface and bulk leakage samples. The arrows show which axes should be read.

98

surface leakage sample (solid curves) with a fully electroded sample (dashed curves) for nearly identical electron irradiation, i.e., incident electron energy and incident flux. Note that all currents shown in Figures 54 through 60 are, in fact, negative except where indicated. For the surface leakage sample, the current shown is the sum measured from both electrode arrays (Figure 52) whose areas are 3.52 cm^2 total. That shown for the fully electroded sample is the current from the front electrode I_1 whose area is 42 cm^2. For this case the electrode area ratio is 0.084 and the measured current ratio is 0.15. This is an indication that the current flow for the surface sample results not only from the electrode region but also from the collection of charge deposited in the nonelectroded insulator. In fact, the ratio of the total area bounded by the electrode fingers to that of the electrode area of the totally electroded sample is just 0.16, which indicates that nearly all charge deposited in the surface sample is being collected in equilibrium.

RT-18025
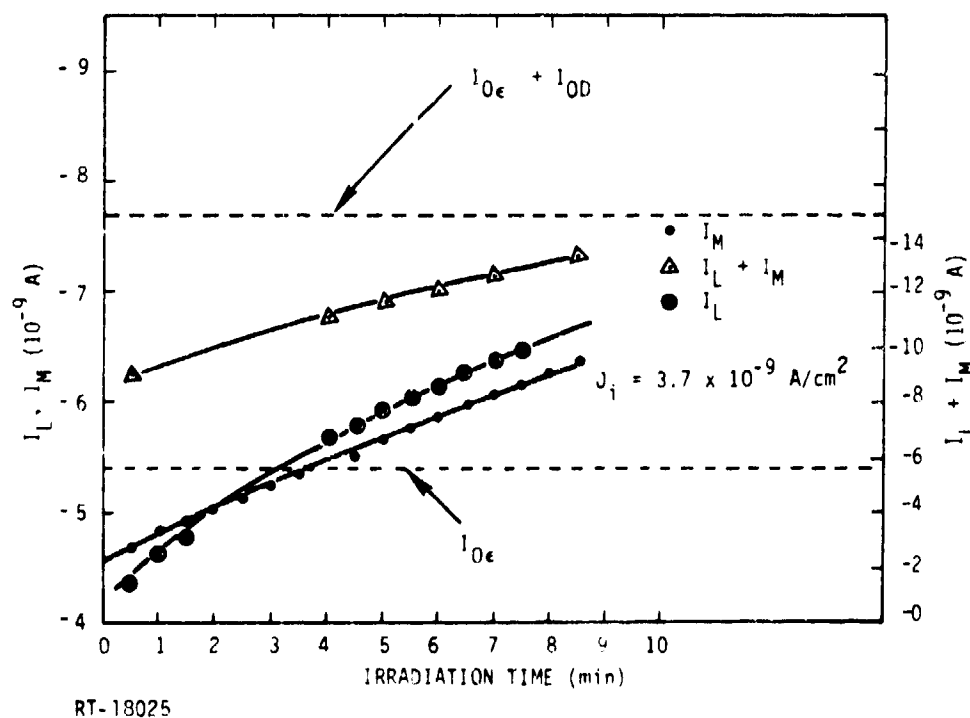
Figure 55. Charging behavior of surface sample exposed to an 8 keV electron beam

The time dependence of current flow is considerably different for the two cases as shown in Figure 54. For the fully electroded sample, the current flow to ground from the front electrode reaches an equilibrium value in less than two minutes, compared to ~12 minutes for the surface sample. The former reaches a constant value when the
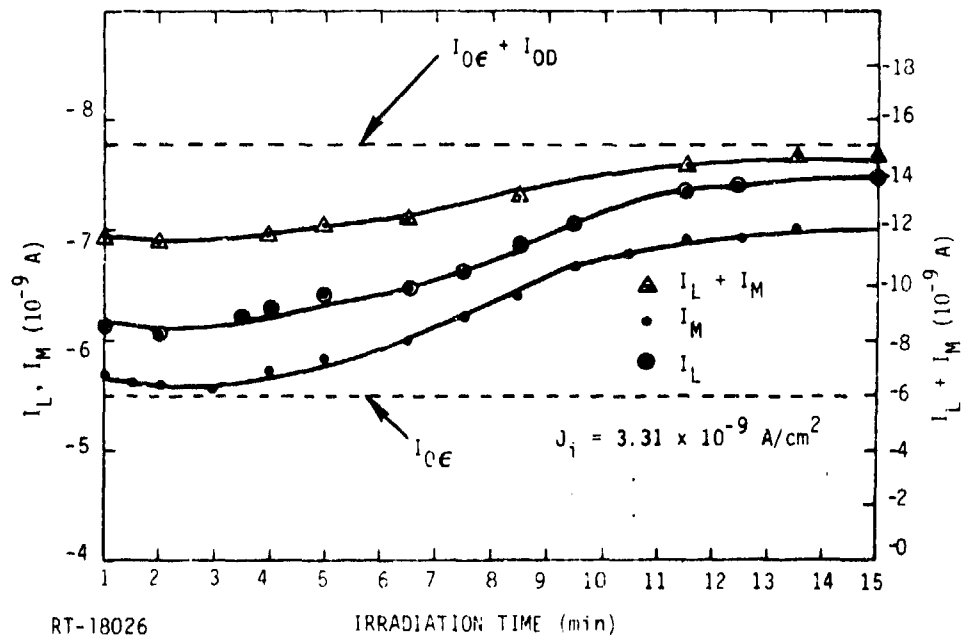
99

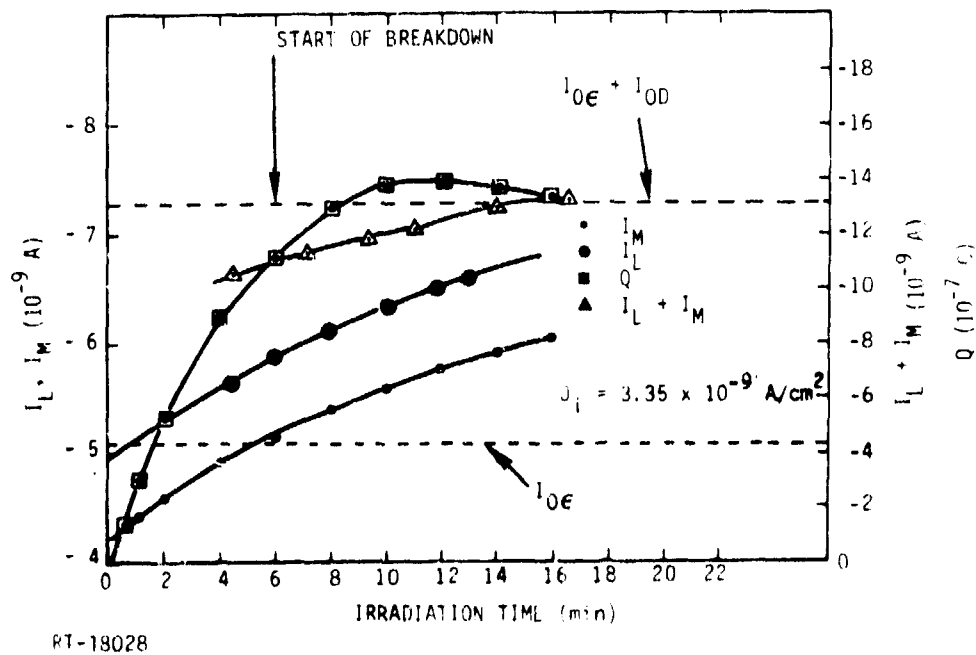**Figure 56.** Charging behavior of a surface sample exposed to a 12 keV electron beam

Figure 57. Irradiation of Mylar surface sample with 8 keV electrons

100
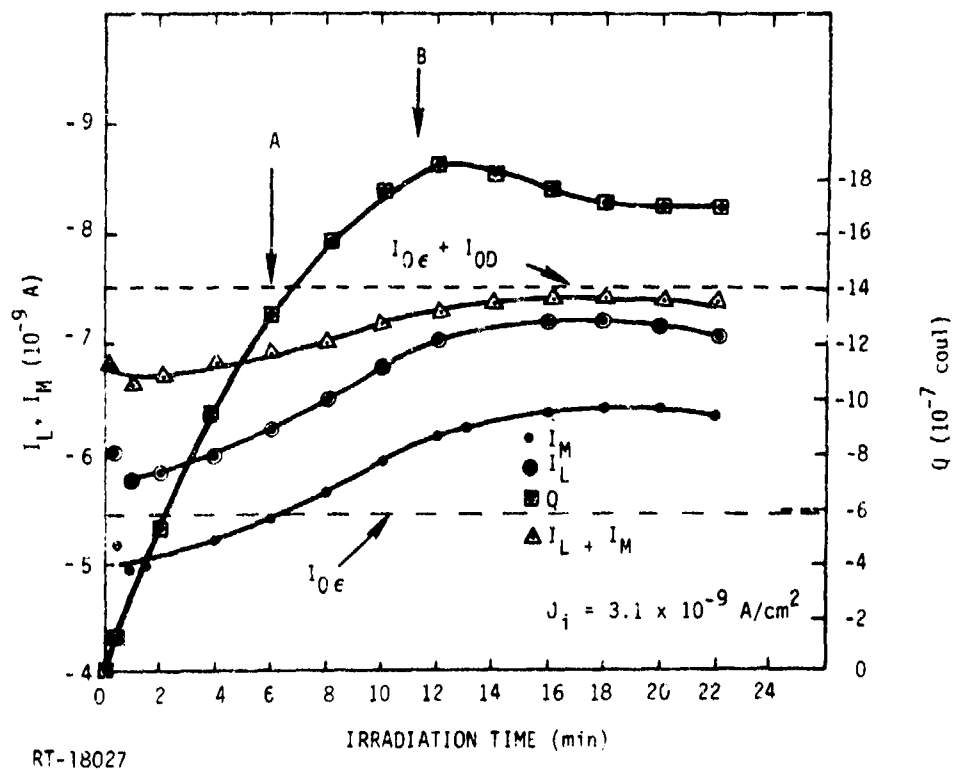
Figure 58. Irradiation of a Mylar surface sample with 12 keV electrons

maximum equilibrium stored charge density (equal to $J_0 \tau_D$ if leakage is neglected) is established. The slower increase in I_1 and I_2 is probably indicative of the decrease in J_0 as the average potential of the dielectric surface rises towards the second crossover voltage; i.e., more of the incident beam is backscattered and secondary emission increases. There is also the possiblity of beam steering (deflection of the beam to the grounded outer electroded portion of the surface charging sample). The average current flow from the surface sample never quite reaches its anticipated value because of discharging which results in charge loss.

Figure 54 also compares the charging rate for the two cases. Charge is determined from a measurement of the voltage across the capacitor C_2 (Figure 52) that connects the rear electrode to ground. This measurement does not differentiate between displacement and leakage current, and in the case of the surface sample does not differentiate between charge deposited beneath the array that measures surface leakage current and that deposited beneath the grounded front electrodes that cover the remainder of the sample.

101

The charge buildup in the fully electroded sample increases rapidly at the onset of irradiation until an equilibrium charge density is established after a few minutes. The continued apparent charge buildup after this time results from leakage current from the charge layer to the back electrode (this charge is continually replenished by the electron beam). Charge buildup in the surface sample, however, reaches a maximum value after ~12 minutes of irradiation and then remains constant or decreases with continued irradiation. This leveling off or decrease in measured charge density results from charge loss from repeated small breakdowns. It is also interesting to note that the charge buildup in the surface is a factor of five larger than that for the fully electroded sample, even though only 8 percent of the total indicated surface ($3.2 \text{ cm}^2/42 \text{ cm}^2$) is nonelectroded. It is likely that extra charge is embedded in the dielectric to build up the field gradients between electrodes above that needed to provide charging equilib-rium $= I_t\tau = (0.6)(3.3 \times 10^{-9} \text{ A/cm}^2) \times 45.8 \text{ s} \times 42 \text{ cm}^2 = 3.8 \ \mu\text{C}$. The value $\tau = 0.6$ was obtained from Figure 14. Note that in estimating I_{0D}, allowance is made for back emission of electrons from the dielectric using the data of Reference 47. At 8 keV $\beta + \delta = 0.25$. At 12 keV, $\beta + \delta = 0.20$, for Mylar.

Figure 55 presents similar data for an 8 keV electron irradiation for a slightly different fluence. Note that the amount of the net current charging the electrode $I_{0\epsilon}$ is smaller at the lower energy, reflecting an increase in secondary emission and backscatter. No change was observed in the currents collected in I_L and I_M as a result of applied bias as large as 90 volts, a value small compared to the magnitude of the transverse fields built up due to charging alone. During the measurements the following set of bias voltage were applied: 0 to 2 min, 0 volts; 2 to 4 min, 20 volts; 4 to 6 min, 40 volts; 6 to 7 min, 70 volts, 7 to 8 min, 90 volts; 8 to 9 min, 0 volt. Figure 55 also compares the sum of currents I_L and I_M with calculated maximum and minimum currents. The minimum current (lower dashed curve of Figure 55) is just the current that penetrates the electrode (i_{0c}). The maximum current that would be observed is the sum of this current and the dielectric charging current I_{0D}. As shown in Figure 55, the measured current value falls between the predicted maximum and minimum values. That the measured values are greater than the calculated minimum value is a clear indication that a part of the charge deposited in the base insulator material between electrodes leaks to the electrodes. That the measured current is independent of external bias indicates that the built-in field that results from charge buildup between the electrodes significantly exceeds that due to the external bias. Failure of the average measured current to achieve the calculated maximum value is due in part to

charge loss via breakdown. Breakdown began approximately six minutes after start of irradiation and continued during the remainder of the irradiation.

Figure 56 shows similar data for a 12 keV irradiation. Again, the measured currents lie between the calculated maximum and minimum values. The shape of the current versus time between 0 and ~3 minutes results from charge recall as a result of the prior 8 keV irradiation.

During the bias dependence measurements discussed above, the back electrode was grounded. Approximately two weeks later, the surface charging experiments were repeated and charge accumulation in the sample was measured by a 1 μF capacitor connected between the back electrode and ground. The circuit used for these measurements is shown in Figure 50. The results of these experiments are shown in Figures 57 and 58. At both energies, the charge buildup within the sample reaches a maximum and then remains constant or decreases slightly with further irradiation as the average charge lost by breakdown and leakage equals the rate of charge deposition.

Two types of breakdown were observed when a comparison was made between the 8 and 12 keV irradiations. Figure 59 shows a trace of a strip chart record of the current I_M and the sample charge, Q_2, as a function of time during a 12 keV irradiation. The circuit configuration is shown in the inset of Figure 59. The lower curve of Figure 59 shows the change in collected current I_M that results from breakdown. The former discharges result in a net charge loss from the sample as shown by the upper curve of Figure 59. The decrease in I_M after discharge is a result of the fact that additional charge is captured by the dielectric, and less leaks to the electrodes (q.v., Figures 54 through 57). The positive-going excursions of I_M in Figure 59 do not result in significant sample charge loss. These observations indicate that the principal charge loss during breakdown results from the blowoff of charge from the front surface rather than breakdown to the electrodes. The second type of discharge could be attributed to punchthrough to the rear electrode. Such a discharge would not change Q_2. After breakdown, the charge loss is replenished by the electron beam and by electron flow from ground through the current meter to the electrodes.

During the 12 keV irradiation, breakdown started to occur approximately six minutes after start of irradiation (point A of Figure 58). Between 6 and 11 minutes (point B of Figure 58) the breakdowns were of the type that produced no significant charge loss (upward excursion of I_M) and the sample continues to charge. At 11 minutes, (point B in Figure 58) the second type of breakdown, that results in loss of charge, starts and continues to occur while the sample retains a more or less constant
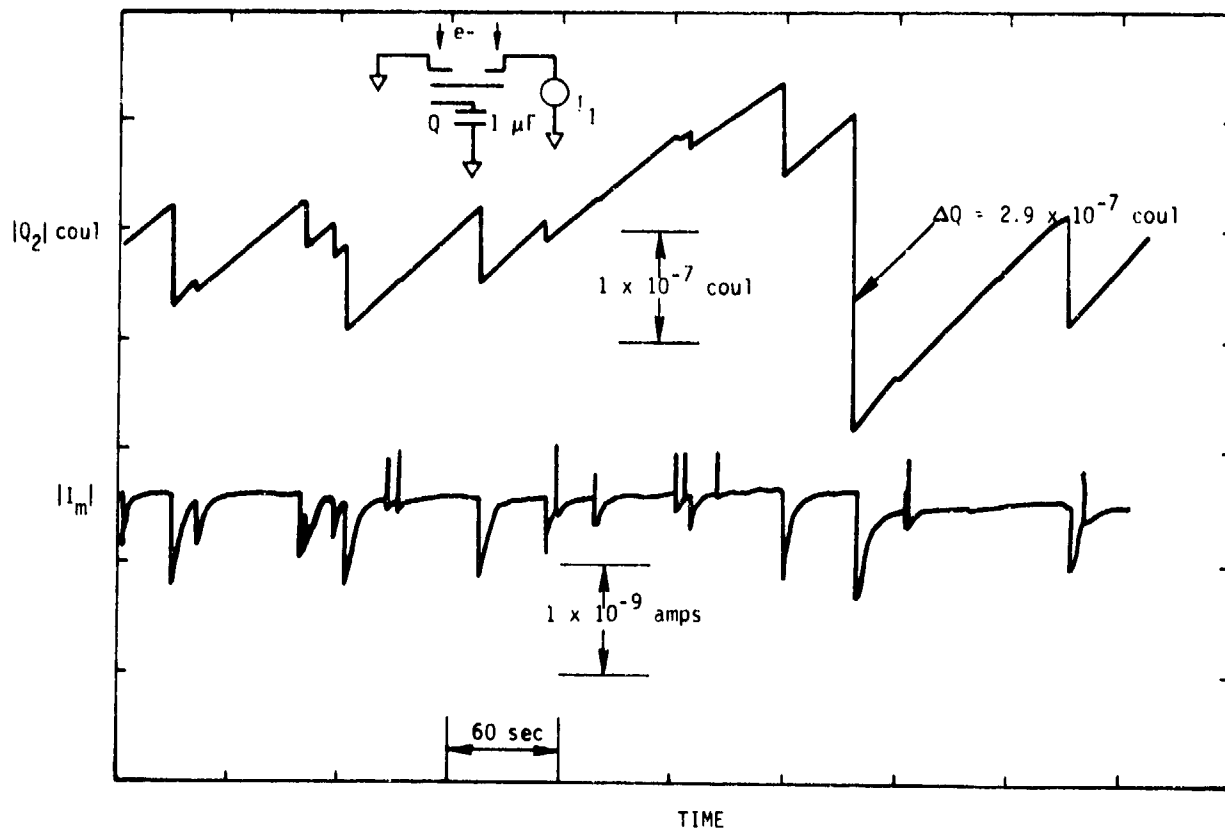
RT-18029

Figure 59. Strip chart trace of the charge on the rear sample electrode and the current flowing out of the front electrode for a 12 keV electron irradiation of the Mylar surface sample
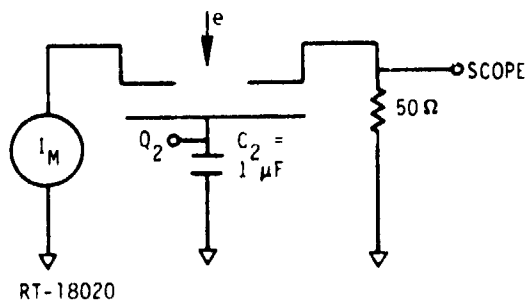

RT-18020

Figure 60. Experimental setup used to photograph breakdowns

104

amount of stored charge; that being lost in a discharge is replenished in subsequent charging. The 8 keV irradiation produced very few breakdowns of the second type. However, the sample still reached a charge equilibrium as shown in Figure 57.

The circuit configuration used to photograph breakdown in the 25 μm Mylar S sample is shown in Figure 60. Figure 61 is a photograph of current flow from one of the electrode arrays during a breakdown that resulted in a charge loss of 2.7×10^{-8} C. The polarity of the trace in Figure 61 results from electron flow from the sample front electrode to ground as expected for flashover. The area under the curve is 6×10^{-9} C which is approximately 20 percent of the total charge loss as measured by the 1 μF capacitor that monitors the change in charge stored within the sample. This is reasonable if some of the charge is lost to space because of blowoff. Note that the observed discharge shows both flashover and blowoff.

In summary, it was not practical to measure the surface conductivity in the manner originally proposed. However, the sample arrangement has proved valuable insights into the charging of two-dimensional surfaces. It is possible to study surface charging effects with such a setup, i.e., to systematically examine edge effects which are important in controlling charging. Many practical fixes for spacecraft charging involve grounding edges. Implicit in our analysis is the idea that in this case surface conductivity can be more precisely defined than normally possible; i.e., it is just the product of the mean radiation conductivity in the irradiated region times the thickness of the dose deposition region. Moreover, the value of obtaining strict current closure in these measurements has been amply demonstrated.
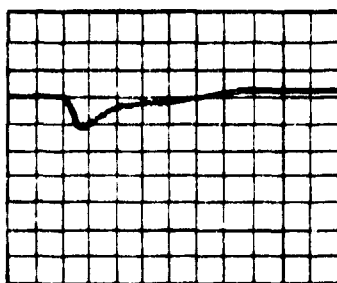
RT-18033

Figure 61. Discharge current through the 50 ohm resistor.
The horizontal axis represents 50 ns/div and
the vertical axis represents 40 mA/div.

105

REFERENCES

1. C. P. Pike and M. H. Bunn, "A Correlation Study Relating Spacecraft Anomalies to Environmental Data," in Reference 2, page 45.

2. A. Rosen, ed., Progress in Astronautics and Aeronautics, Vol. 47, "Spacecraft Charging by Magnetospheric Plasmas," MIT Press, 1976.

3. C. P. Pike and A. R. Lovell, eds., Proceedings of the Spacecraft Charging Technology Conference, AFGL-TR-77-0051, 24 February 1977.

4. Spacecraft Charging Technology - 1978, NASA Conference Publication 2071, (1979).

5. A. Rosen, IEEE Trans. on Nucl. Sci. 23, 1762 (1976).

6. A. Meulenberg, "Evidence for a New Discharge Mechanism for Dielectrics in a Plasma," in Reference 2, page 237.

7. R. C. Keyser, R. E. Leadon, A. Weiman and J. Wilkenfeld, Electron-Induced Discharge Modeling, Testing and Analysis for SCATHA (Two Vols.), DNA4820F-1, -2, 31 December 1978.

8. D. A. McPherson and W. Schober, "Spacecraft Charging at High Altitudes: The SCATHA Satellite Program," in Reference 2, page 15; and R. P. Lovell, N. John Stevens, W. Schober, C. P. Pike, and W. Lehn, "Spacecraft Charging Investigation: A Joint Research and Technology Program," in Reference 2, page 3.

9. H. B. Garrett, "Modeling of the Geosynchronous Orbit Plasma Environment 1," AFGL TR-0288 (1977), "Review of Quantitative Models of the 0-to-100 keV Near-Earth Plasma," Rev. Geophys. and Space Phys. 17, 397 (1979).

10. N. J. Stevens, R. E. Kaman and A. B. Holman, "Design Guidelines for Assuring and Controlling Spacecraft Charging Effects," NASA Monograph, November 1979 (Draft), Appendix A.

11. O. R. White, "The Solar Output and Its Variation," Colorado Associated Universities Press (1977).

12. J. I. Vette, K. W. Chan, M. J. Teague, "Problems in Modeling the Earth's Trapped Radiation Environment," AFGL-TR-78-0130, September 30, 1978.

13. J. B. Claddis, G. T. Davidson, L. L. Newkirk, "The Trapped Radiation Handbook," DNA 2524H, Revision of January 21, 1977.

14. B. Feuerbach and B. Fitton, "Experimental Investigation of Photoemission for Satellite Surface Materials," J. Appl. Phys. 43, 1563 (1972).

15. E. P. Wenaas, M. J. Treadaway, T. M. Flanagan, C. E. Mallon and R. Denson, "High Energy Electron Induced Discharge in Printed Circuit Boards," IEEE Trans. Nucl. Sci. NS-26, 5152 (1980).

16. I. Katz, D. E. Parks, M. J. Mandell, J. M. Harvey, D. H. Brownell, S. S. Wang and M. Rotenberg, A Three-Dimensional Dynamic Study of the Electostatic Charging for Materials, NASA CR-135256, August 1977.

17. K. Balmain and G. Dubois, "Surface Discharges on Teflon, Mylar, and Kapton," IEEE Trans. Nucl. Sci. NS-26, 5146 (1979).

18. J. A. Wall, E. A. Burke, and A. R. Frederickson, "Results of Literature Search on Dielectric Properties and Electron Interaction Phenomena Related to Spacecraft Charging," in Reference 3, pages 569-592.

19. J. van Turnhout, Thermally Stimulated Currents in Polymer Electrets, Elsevier, Amsterdam, 1975.

20. M. M. Perlman, ed., Electrets: Charge Storage and Transport in Dielectrics, Electrochemical Society, Princeton, 1973.

21. International Symposium on Electrets and Dielectrics, Brazilian Academy of Sciences, 1977, especially the article by B. Gross and L. Nunes de Olivera, "Electron Beams as Virtual Electrodes," pp 15-49.

22. W. E. Spear, "Electron Bombardment Effects in Thin Dielectrics," Proc. Phys. Soc. B68, 991 (1955).

23. J. A. Rutherford, S. M. Trujillo and J. Wilkenfeld, An Electron Gun for Simulating Spacecraft Charging Effects, IRT 8176-002, February 1978.

24. B. Gross, G. M. Sessler, and J. E. West, "Charge Dynamics for Electron Irradiated Polymer Foil Electrets," J. Appl. Phys. 45, 2481 (1974).

25. L. Nunes de Olivera and B. Gross, "Space Charge Limited Currents in Electron Irradiated Dielectrics," J. Appl. Phys. 46, 3132 (1975).

26. V. E. Cosslett and R. N. Thomas, "Multiple Scattering of 5-30 keV Electrons in Evaporated Metal Films, III," Brit. J. Appl. Phys. 16, 779 (1965).

27. J. F. Fowler, "X-Ray Induced Conductivity in Insulating Materials," Proc. Roy. Soc. (London) A236, 464 (1956).

28. V. Adamec and J. H. Calderwood, "Electrical Conduction at High Fields," J. Phys. D8, 551 (1975).

29. R. Bube, Photoconductivity of Solids, (Wiley, New York, 1960), p. 278.

30. E. H. Darlington, "Backscattering of 10-100 keV Electrons from Thick Targets," J. Phys. Sci. 8, 85 (1975).

31. E. A. Burke, J. A. Wall, A. R. Frederickson, "Radiation Induced Low Energy Electron Emission from Metals," IEEE Trans. Nucl. Sci. NS-17, 193 (1970).

32. M. J. Berger and S. M. Seltzer, Studies in Penetration of Charged Particles in Matter, Publication 1133 (National Academy of Sciences - National Research Council, Washington, D.C., 1964), pp. 205-279.

33. J. C. Ashley, C. J. Tung, R. H. Ritchie, and V. E. Anderson, IEEE Trans. Nucl. Sci. NS-23, 1833 (1976).

34. A. R. Frederickson, "Electric Fields in Irradiated Dielectrics," in Reference 4, pages 554-569.

35. B. Gross, G. M. Sessler, and J. E. West, "Location of Charge Centroid in Electron Beam Charged Films," J. Appl. Phys. 48, 4303 (1977).

36. E. J. Kobitch and R. Katz, "Energy Deposition by Electron Beams and X-Rays," Phys. Rev. 170, 391 (1968).

37. G. M. Sessler and J. E. West, "Trap Modulated Mobility of Electrons and Holes in Teflon FEP," J. Appl. Phys. 47, 3480 (1976).

38. H. J. Wintle, "Transient Charging Currents in Insulators," Solid-State Electronics 10, 1039 (1975).

39. T. J. Ahrens and F. Wooten, "Electrical Conductivity Induced in Insulators by Pulsed Radiation," IEEE Trans. Nucl. Sci. NS-23, 1268 (1976).

40. R. C. Hughes, "Charge Transport by Photocarriers in Polymer Films," in Proceedings of the Second International Conference on Electrophotography, Society of Photographic Scientists and Engineers, Washington, D.C., 1974.

41. F. C. Aris, P. M. Davies and T. J. Lewis, "Electron Beam Induced Conduction in Dielectrics," J. Phys. C.: Solid State Phys. 9, 797 (1976).

42. L. M. Beckley, J. J. Lewis, and D. M. Taylor, "Electron Beam Induced Conduction in Polyethylene Terephthalate Films," J. Phys. D.: Appl. Phys. 9, 1355 (1976).

43. G. M. Sessler, J. E. West, D. A. Berkeley, and G. Morgenstern, "Determination of Spatial Distribution of Charges in Thin Dielectrics," Phys. Rev. Lett. 38, 368 (1977).

44. D. A. Berkeley, "Computer Simulation of Charge Dynamics in Electron Irradiated Polymer Foils," J. Appl. Phys. 50, 3447 (1979).

45. B. L. Beers, "Electron Transport Model of Dielectric Charging," IEEE Trans. Nucl. Sci. NS-24, 2429 (1977).

46. N. John Stevens, Carolyn K. Purvis, and John Staskus, "Insulator Edge Voltage Gradient Effects in Spacecraft Charging Phenomena," IEEE Trans. Nucl. Sci. NS-25, 304 (1978).

47. E. Burke, "Secondary Emission from Polymers," IEEE Trans. Nucl. Sci. NS-27, 1760 (1980).

GLOSSARY OF SYMBOLS

A	Irradiated sample area
A	Constant in range-energy relationship (Equation 24)
A_D	Exposed front dielectric surface area of surface conductivity samples
A	Electrode area of surface conductivity samples
B	Constant in range-energy relationship (Equation 24)
b	Constant in delayed conductivity equation (Equation 14)
C	Constant in range-energy relationship (Equation 24)
$C_{1,2,3}$	Capacitors used to measure stored charge (q.v. Figure 11b)
$\dot{D}$	Dose rate
$\overline{D}_{kk}$	Average dose deposited in the polymer calculated with Equation 24 and Equation 25.
$\overline{D}_s$	Mean dose deposited in the polymer sample based on a SANDYL calculation
E	Electric field
E_i	Energy of incident electrons
$\overline{E}_t$	Average beam energy after passage through the front electrode of thickness t.
G	Current gain
$\overline{g}(t)$	Delayed conductivity
$g_{A,B}$	Conductivity in regions A, B of the dielectric, respectively
$g_{A0,B0}$	Dark conductivity in regions A, B, respectively
g_D	Radiation-induced conductivity
g_{00}	Dark conductivity at zero electric field
$I_{A,B}$	Solenoidal currents in regions A, B, respectively
I_b	Net back emitted current
I_{bD}	Net current back emitted from the dielectric surface of the surface conductivity sample

111

I_b	Net current back emitted from the front electrode
I_i	Incident current
$I_{L,M}$	Current leaving electrode arrays L, M, respectively, of the surface conductivity sample
I_t	Net current injected into the sample
I_{BF}	Current collected by the Faraday cup sampling the back emitted current
i_α	Current exiting front electrode due to stopping of a fraction of the beam therein
I_β	Backscatter current
I_δ	Secondary emission current
I_τ	Current injected into the dielectric
I_0	Net charging current
I_{0D}	Net charging current deposited in the dielectric surface of the surface conductivity sample
$I_{0\epsilon}$	Net charging current deposited in the front electrode surfaces of the surface conductivity sample
$I_{1,2}$	Currents leaving front or rear electrodes, respectively
$J_{A,B}$	Net solenoidal current densities in dielectric regions A, B, respectively
J_t	Injected current density
J_y	Surface current density
k	Calibration constant for Faraday cup monitoring back emitted currents
$\bar{k}$	Constant in delayed conductivity equation (Equation 14)
k_B	Boltzmann's constant $= 8.63 \times 10^{-5}$ eV/$^\circ$K
K_D	Radiation-induced conductivity constant
q_t	Trapped charge per unit irradiated sample area
Q_0	Net charge deposited in the sample
Q_t	Charge deposited in the dielectric
$Q_{1,2}$	Charge on capacitors $C_{1,2}$, respectively
q_2	Charge per unit irradiated sample area on C_2

112

$\overline{R}$	Centroid of injected charge
r	Thick target backscatter coefficient for polymers
$\overline{R}_i$	Experimentally determined value of injected charge centroid
R_p	Practical range
R_{ps}	Practical range determined from SANDYL calculation
$\overline{R}_s$	Mean range determined from SANDYL calculation
T	Sample temperature
t	Time
t	Front electrode thickness in g/cm^2
T_e	Plasma electron temperature
T_s	Sample thickness
V_c	Negative voltage at which $I'_1 = 0$
$V_{c'}$	Bias voltage threshold for hole conduction in the nonirradiated region of the polymer
$V_{C1,C2}$	Voltages across capacitors C_1, C_2, respectively
V_o	Voltage at which $I_2 = 0$
V_1	Potential of front electrode relative to ground
x	Perpendicular distance from the front face of the sample to an interior point
y	Distance along the dielectric surface of surface conductivity sample
α	Fraction of incident beam absorbed in front electrode
β	Backscatter coefficient
β'	Backscatter coefficient for electrons traversing a thin foil
β_F	Frenkel parameter
γ	Power law dependence of time decay of delayed conductivity
Δ	Power dependence of radiation-induced conductivity on dose rate
δ	Secondary emission coefficient
Δx	Constant in secondary emission equation (Equation 22)

ϵ	Dielectric constant
$\mu_{A,B}$	Trap modulated mobility of predominant charge carrier in regions A, B, respectively
ρ	Space charge density
σ	Planar charge density
τ	Transmission coefficient of electrons through front electrode
τ'	Transmission coefficient of electrons traversing a foil thin compared to electron range
τ_D	Characteristic relaxation time in irradiated polymers

MISSION
of
Rome Air Development Center

RADC plans and executes research, development, test and selected acquisition programs in support of Command, Control Communications and Intelligence (C^3I) activities. Technical and engineering support within areas of technical competence is provided to ESD Program Offices (POs) and other ESD elements. The principal technical mission areas are communications, electromagnetic guidance and control, surveillance of ground and aerospace objects, intelligence data collection and handling, information system technology, ionospheric propagation, solid state sciences, microwave physics and electronic reliability, maintainability and compatibility.